INTERNATIONAL UNIVERSITY LIAISON INDONESIA (IULI)

BARUNA 1: An Aerial Firefighting

Presented to 2021-2022 AIAA
Aircraft Design Competition

By
INFERNO TEAM

May 15, 2022

Executive Summary

BARUNA 1: An Aerial Firefighting

by INFERNO TEAM

Modern aerial firefighting is constantly evolving, with new problems and technology always emerging. As fire threats continue to improve, especially in the forest, so must aerial firefighting technology. At the same time, this constant improvement of technology and capability in an aerial firefighting environment comes with added cost. The ultimate goal of new aerial firefighting aircraft is to ensure superiority over the fire and maintain low operational costs. This report summarizes the preliminary design of a new aerial firefighting aircraft destined to take on the role of put on the fire, especially in the forest, all while maintaining a far lower operational cost.

The formal requirements of the aerial firefighting are to entry into service (EIS) in 2030, Use existing engine(s), or one that is in development will be in service by 2028, or at least two years before the airplane EIS, Assumptions on at least specific fuel consumption/efficiency, thrust/power and weight must be documented. The fire retardant capacity minimum is 4,000 gal, with a multi-drop capability minimum of 2,000 gallons per drop, fire retardant reload of 500 gal/min. The drop speed of the payload drop needs to be under 150 kts, and the drop altitude needs to be at least under 300 ft AGL. The design radius with payload needs to be at least 200 n mi, the design ferry range (no payload) needs to be at least 2,000 n mi, dash speed of at least 300 kts.

The following report outlines the preliminary design of the Baruna-1 Aerial Firefighting Aircraft, which meets or exceeds all requirements. The Baruna-1 uses 4 Europrop TP400-D6 with a total power of 44,260 horsepower and a fire retardant capacity of 8000 gallons. The ground support for the Baruna-1 will use two pumps, water, and a vacuum pump, with a fire retardant reload of 1,761 gal/min and 924.6 gal/min, respectively. Baruna-1 could drop eight times at maximum performance, and the amount of retardant that comes out in one drop can be set. The drop speed for the Baruna-1 is $60\,\mathrm{m\,s^{-1}}$, and the drop altitude of can be selected down to 50 m. Under full fuel capacity, Baruna-1 has a maximum mission range of 4500 m with full payload and 12 500 m ferry range.

Inferno Team

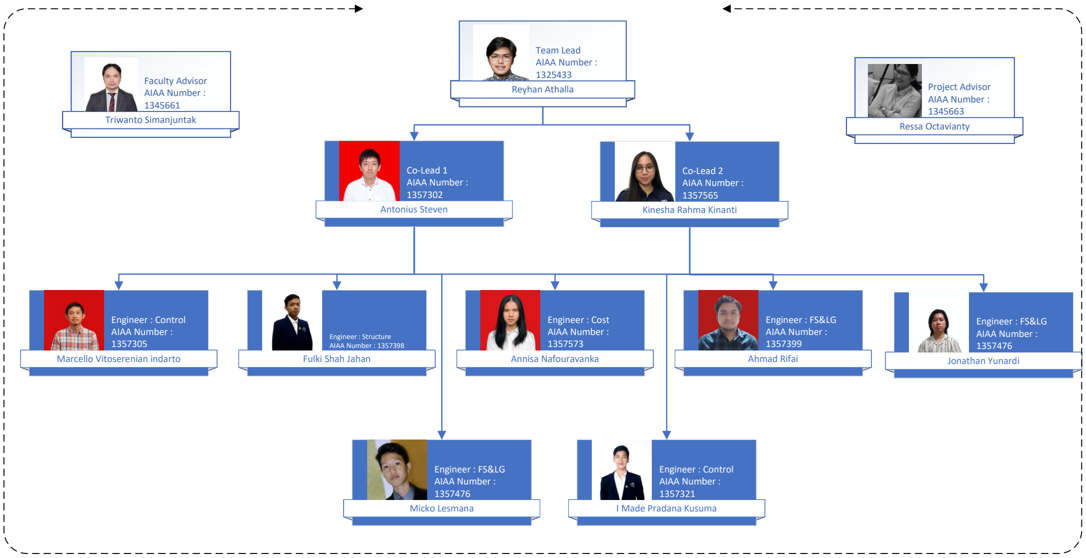

Ahmad Rifai Purboyo

Annisa Nafouravanka

Antonius Steven

Fulki Shah Jahan

Jonathan Yunardi

Kinesha Rahma Kinanti

Marcello Vitoserenian Indarto

Micko Lesmana

Reyhan Athalla

I Made Pradana Kusuma Putra

Dr. Eng. Ressa Octavianty

Triwanto Simanjuntak, PhD

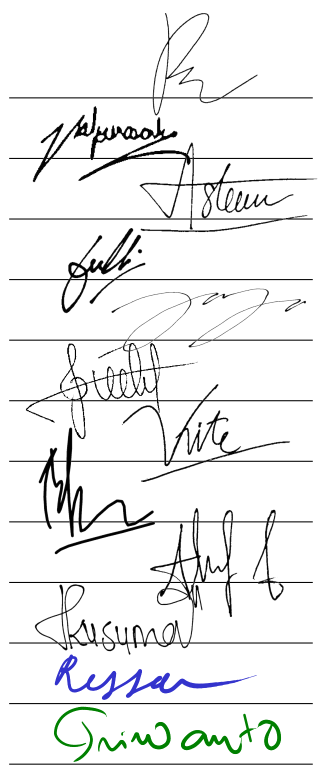

Acknowledgements

This report is the result of our education in the Aviation Engineering undergraduate courses in International University Liaison Indonesia (IULI). Precious memories of learning together as a group over the years as undergraduate students have led us, as a group, to the realization of what is the importance of education. Thus, from this point forward, having a place to quench the thirst of knowledge shall be a daily reminder for us to be grateful. As a part of what led us here, we would want to give our utmost gratitude towards everyone of the Aviation Engineering Faculty who have helped us making this project possible.

First and foremost, Triwanto Simanjuntak, S.T., M.Eng., Ph.D., and Ressa Octavianty, S.T., M.Eng., Ph.D. deserve a special recognition for their assistance and direction throughout whole process of realizing Baruna-1 as as project. With their views and inputs, they assisted us in taking our design to the next level. Not to be forgotten as well, they also gave us advice when we needed it the most.

We also want to thank the TAs — who just completed their bachelor degree — for the courses of Aviation System Design I, II and Flight Control I, II: Prana Rao, S.T. for his assistance in the writing process of the report, Dimas Hisyammadika, S.T. for sharing his CAD skill, and Faisal Tri M., S.T. for his generous assistance in advising the team in Cost and Stability analysis. We believe this project couldn't be completed without their help.

Contents

List of Figures

List of Tables

Nomenclature

Abbreviations and acronyms

(M)TO M/W (Max)Take-off Mass/Weight

AC Aerodynamic Center

AOA Angle of Attack

BP Battery Pack

C/E/T AS Calibrated/Equivalent/True Airspeed

CG Center of Gravity

DR Dutch Roll

EPMS Energy and Propulsion Management System

ESC Electronic Speed Controller

FAR Federal Aviation Regulation

FL Flight Level

FQ Flying Qualities

HUMS Health and Usage Monitoring System

IFR Instrument Flight Rules

IMU Inertial Measurement Unit

ISA International Standard Atmosphere

L/T E Leading/Trailing Edge

LND Landing

MAC Mean Aerodynamic Chord

MEW Maximum Empty Weight

ME Multi Engine

MFD Multi-function Display

NC Non-Continuous

OEI One Engine Inoperative

PFD Primary Flight Display

PGS Power Generation System

PH Phugoid

SEP Single Engine Piston

SE Single Engine

SP Short Period

TO Take-Off

VFR Visual Flight Rules

ZL Zero-Lift

List of Symbols

Symbol	Description	Unit
α	Angle of attack	deg
β	Side-slip angle	deg
δ	Control surface deflection	deg
δ_T	Thrust lever setting percentage	–
η	Efficiency	–
γ	Flight path angle	deg
λ	Taper ratio	–
$\mathbb{E}$	Energy density	Wh/kg
$\mathbb{P}$	Power density	W/kg
$\mathscr{L}, \mathscr{M}, \mathscr{N}$	Rolling, pitching, yawing moments	Nm
$\mathscr{R}$	Range	NM
$\mathscr{T}$	Period of oscillation	s
Φ	Bank angle	deg
ρ	Density	kg/m^3
σ	Crab angle	deg
σ	Stress	Pa
τ	Control surface effectiveness parameter	–
ε	Endurance	h
ξ	Non-dimensional x-axis coordinate	–
AR	Aspect ratio	–
b	Span	m
c	Mean aerodynamic chord	m
C_d, C_l, C_m	2D drag, lift, pitching moment coefficients	–
c_p	Brake specific fuel consumption	$N/(Ws)$
C_{D_0}	Zero-lift drag coefficient	–
D, Y, L	3D drag, side-force, lift	N
E	Energy	J, Wh
e	Oswald efficiency factor	–
F	Control force	N, lbs
F	Power index	–

Symbol	Description
f	Frequency Hz
G	Gearing ratio rad/ft
g	Gravitational acceleration m/s^2
h	Altitude ft
H_n	Static margin –
i	Incidence deg
K	Induced drag coefficient –
L/D	Lift-to-drag ratio –
L_t	Distance between AC of the wing and of the tail m
L_{TO}	Take-off length m, ft
M	Mach number –
m	Mass kg
M_h	Hinge moment Nm
n	Load factor –
p,q,r	Roll, pitch, yaw rates rad/s
P	Power W, hp
P_b	Shaft brake power W, hp
q	Dynamic pressure Pa
Re	Reynolds number –
S	Surface m^2, ft^2
T	Temperature $^{\circ}C$
t	Thickness m
V	Airspeed m/s, kt
V_1	Take-off decision speed kt
V_A	Maneuvering m/s, kt
V_D	Design diving speed m/s, kt
V_F	Designed flap speed m/s, kt
V_V	Vertical speed fpm, m/s
V_X	Steepest climb speed kt
V_Y	Fastest climb speed kt
V_{ht}, V_{vt}	Horizontal and vertical tail volume coefficients –
$V_{max\mathscr{E}}$	Max endurance speed kt
$V_{max\mathscr{R}}$	Max range speed kt
V_{MC3}	Velocity minimum control with 3 EMI kt
V_{NE}	Velocity never exceed m/s, kt
V_{S0}	Stall speed with fully deployed flaps kt
V_{S1}	Stall speed in clean configuration kt
W	Weight N, lbs

Superscripts

Symbol Description

a	Airframe or aileron
bat	Batteries
C	Cruise
c	Elevator
est	Estimated
F	Fuel
f	Flap
fus	Fuselage
h	Hinge
ht	Horizontal
$misc$	Miscellaneous
p	Propilsive
pl	Payload
r	Rudder
rec	Recharge
ref	Reference
$regr$	Regression
t	Trim tab
vt	Vertical Tail
w	Wing
wet	Wetted

Chapter 1

Introduction

1.1 Introduction

Wildfires have been a complex and contingent problem that requires continual attention to the changing situation of stakeholders, landscapes, and ecosystems and also occur at different temporal and spatial scales headlined by the loss of lives and homes [1]. Generally, however, it is administered to any unfortunate effects of unplanned fires on a broad range of social, environmental, and economic assets [1]. Some recent extreme wildfire events that were considered catastrophic, i.e., Australian bushfire back in 2019 through 2020 and August Complex fire back in 2020 [2, 3, 4] caused massive losses. Although the total area burned at a global level over the past decade showed a decreasing trend [2, 3, 4], the mitigation on how to keep the damage to a minimum should still be an utmost concern. According to [5], wildfires affect approximately 4 million km^2 of the Earth's land every year (see Figure. 1.1 for the area affected by wildfires between 1982-2018). In the United States alone, the trend is on the rise in terms of frequency and scale [6].

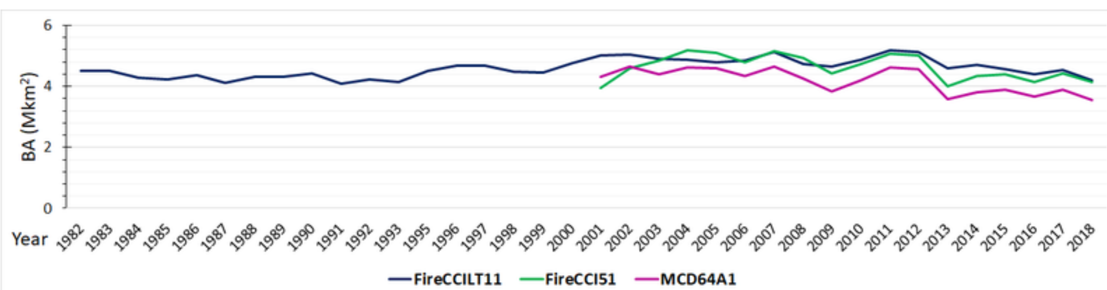

FIGURE 1.1: Burned area (Mkm^2) 1982-2018 showing the FireCCILT11 (based on AVHRR-LTDR data) alongside FireCCI51 and MCD64A19 [5]

During the pre-industrial period, wildfires were strongly caused by precipitation. However, after the industrial revolution, wildfires are now caused anthropogenically (human intervention plays a significant role) [7]. Because of it, especially in the 21st century, global temperature has been rising, creating an unprecedentedly fire-prone environment. Additionally, lightning strikes have been happening more frequently [8], and as the effect of global warming, larger wildfires frequently occur [9, 10].

Frequent wildfires negatively affect various aspects of life, from environmental damage to health problems. Wildfires are known to be a source of tropospheric ozone (O^3), a greenhouse gas that results in the impacts mentioned above [11]. Respiratory problems, burns, cardiovascular morbidity, and psychological are examples of health problems we might face [12]. Water and land pollution caused by the ashes of the wildfire are some examples of the environmental aspects impact [13]. As a result, the local inhabitants have the imposing danger of losing the ability to survive inside the wildfire-produced contaminated environment [13]. An additional point to be accounted for is the potential social impact of wildfire, and the most straightforward one would be the demographic impact. i.e., potential economic, infrastructure losses and the resources needed to protect human populations from wildfire risk[14]. Thus ways of combating wildfires are needed, and according to [15, 16], there are two main stages in wild-land fire fighting,

1. **Initial attack**, the actions taken by the first responders of a wildfire incident. Typically, it only involves a handful of resources and the incident is at a small scale; and
2. **Extended attack**, the suppression activity for a wildfire that is unable to be contained or controlled by the initial attack responders.

Both of them involve fire suppression and fuel treatments in fire regimes [1]. The most common approach to deal with this is by the application of water spray, foam spray, foamed water spray, and superabsorbent polymer gels either by fire hoses, by air delivered by aircraft [17], or by employing ground autonomous robot [18]. With the stated approach, the main problem with suppressing wildfires is rooted in the accessibility of the fire site. Harsh terrains would be a total disaster for a retardant-carrying land vehicle to get access. One solution to avoid the terrain problem as quickly as possible is to use aerial fire fighting, which enables personnel to extinguish the fire quickly [19, 20].

In doing so, modifications to the aircraft designs are required. Fortunately, such aircraft existed already and come in different types, e.g., land-based air tankers [21] with single [22] or multiple engines [23], scoopers [24] and helicopters [25]. However, according to AIAA Request For Proposal (RFP) [26], current air tankers have several flaws. The majority of in-service air tankers for firefighting are the result of modifying commercial or military airframes. Internal or external integration of equipment on the airframes creates inefficiencies caused by the difference in payload delivery in comparison to the aircraft's original design missions [26]. Hence, this should be an incentive for researchers in the related fields to develop an idea of a fire-fighting-dedicated aircraft design.

1.2 Market Analysis

1.2.1 Market Size

The aerial firefighting fleet may consist of several different types of aircraft. The classification mainly depends on the size of the aircraft. Smaller-sized aircraft such as OV-10A and B200 King Air can act as air tactical aircraft; relaying information about the spread of a wildfire to the firefighting team. On the other end of the spectrum, bigger-sized aircraft such as MD-87 or C-130 may carry water or retardant to execute "Fire Attack" to wildfire hotspots. The same mission can also be carried out with the help of helicopters equipped with water buckets/scoopers.

Table. 1.1 displays some publicly available firefighting fleets information for some government and private institutions. The total fleet sizes shown are a mix of various types of aircraft (e.g. fixed-wing, rotary-wing, tactical, air tanker). The aircraft may also be under lease, day contracts (e.g. 90 or 160-days

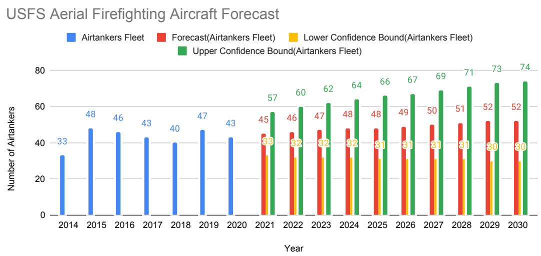

FIGURE 1.2: USFS fleet growth.

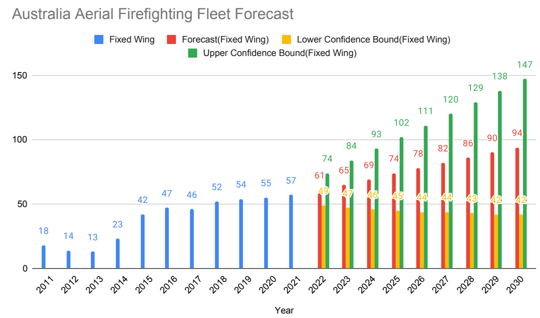

FIGURE 1.3: NAFC fleet growth.

contract), or on Call-When-Needed (CWN) contracts and hence not directly owned by the institutions.

Institution	Fleet Size	Operator
Babcock [**babcock**]	70+	Private
CAL Fire [**calfire**]	50+	Govt.
South Australian Country Fire Service [**cfs**]	26	Govt.
Tasmanias Government [**tasmanian**]	32	Govt.
Dauntless Air [**dauntless**]	15	Private
Alaska Department of Natural Resources [**alaska**]	12	Govt.
Kishugu Aviation [**kishugu**]	40+	Private
Victoria Government [**victoria**]	50	Govt.

TABLE 1.1: Firefighting fleet sizes.

1.2.2 Market Forecast

Predicting the size of an aerial firefighting fleet requires a lot of data and is often very region-specific; not to mention the availability of the data to produce a logical extrapolation. For the USA and Australia, we have created a demand forecast for fixed-wing air tankers from 2022 to 2030 judging by the data collected from the United States Forest Service (USFS) [**usfs**] and the Australia's National Aerial Firefighting Center (NAFC) [**nafc1**] [**nafc2**].

The forecasts presented in Figure. 1.2 and Figure. 1.3 shows linear extrapolations of the fixed-wing aircraft fleet growth for the USFS and the NAFC, respectively. The lower and higher growth scenarios are also included in the charts to provide some perspectives on future fluctuations and/or uncertainties. By considering the current wildfire trend, it is safe to say that the scenarios with positive fleet growth is the most probable ones.

On average, the USFS' fleet will increase with a steady pace between 2 and 3 aircraft per year up to the year 2030. On the other hand, the NAFC's fleet grows relatively sharper around 4 to 9 aircraft per year. Considering the available fleet data, these numbers may be used as a preliminary baseline for projecting fleet growth for other countries that have similar environmental conditions as the USA and Australia; which in turn can be used to predict the global aerial firefighting fleet growth. These estimates are able provide the aircraft manufacturers a preliminary insight on the desired production rate for 2030 and beyond.

1.3 Design Requirements and Objectives

The project aims to design a "Responsive Aerial Fire Fighting Aircraft" which complies with the design requirements and objectives (DRO) specified in AIAA Request For Proposal. The detail of this DRO is specified in Table. 1.2.

Code	RFP	Mandatory	Goal
R0	Entry into service (EIS)	Year 2030	Year 2030
R1	Engine readiness year	$\leq$ Year 2028	$\leq$ Year 2028
R2	Specific fuel consumption/ efficiency, thrust/power and weight	Assumptions must be documented	
R3	Fire retardant capacity (gallons)	4000	8000
R4	Multi-drop capability	Yes	Yes
R5	Volume per drop	$\geq$ 2000	$\geq$ 3000
R6	Fire retardant reload rate	$\geq$ 500 gal / min	750 gal / min
R7	Retardant density	$\geq$ 9 lbs/gal	9 lbs / gal
R8	Drop speed	$\leq$ 150 kts	$\leq$ 125 kts
R9	Drop altitude	$\leq$ 300 ft AGL	150 ft AGL
R10	Design radius with full payload (n mi)	200	400
R11	Design ferry range (kts)	2000	4000
R12	Dash speed (kts)	300	400
R13	Balanced field length	$\leq$ 8000 ft @ 5,000 ft MSL elevation on a +35°F hot day	$\leq$ 5000 ft @ 5,000 ft MSL elevation on a +35°F hot day
R14	Certification	VFR and IFR flight with an autopilot	VFR and IFR flight with an autopilot
R15		Flight in known icing conditions	Flight in known icing conditions
R16		FAA 14 CFR Part 25	FAA 14 CFR Part 25
R17		Autonomous operations	

TABLE 1.2: Design requirements as per specified in the Request for Proposal for Responsive Aerial Fire Fighting Aircraft by AIAA [26].

1.4 Initial Sizing

One of the primary steps in aircraft design is determining the initial size of the aircraft. The easiest way to do this is a benchmark study of other firefighting aircraft. As shown in Figure. 1.4, the competitor aircraft have empty weight $\pm$ 0.57 of the MTOW. Regarding AIAA's requirements, the payload is considerably heavy at around 38,800 kg of retardant mass ($\approx$ gallons). From the statistical study of those aircraft data, there are only a few aircraft competitors that can fill the gap for aerial tankers that can carry more than 5,000 gallons and less than 12,000 gallons (see the shaded region in the Figure. 1.4). So it is expected that the new aircraft will fall into this range of weight. In addition to that, amongst those data, the number of aircraft with two-drop capability is only a few. Therefore, it is a challenge to meet the design requirement of multiple-drop capability and other performances set by RFP. Reducing the empty-MTOW

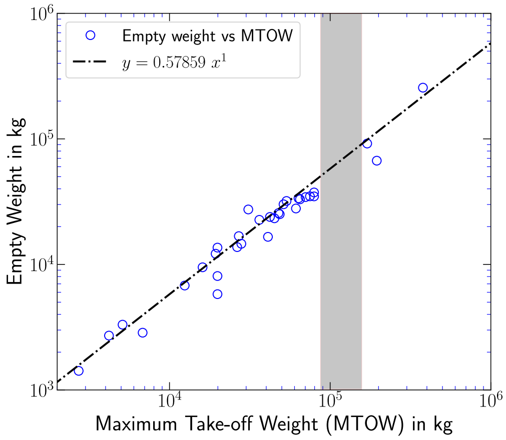

FIGURE 1.4: Empty weight vs MTOW

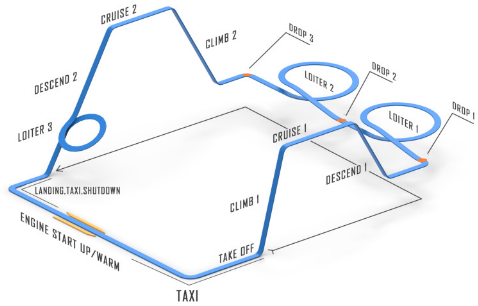

FIGURE 1.5: Mission profile of a 3 payload-drop missions.

ratio as close as a military cargo/bomber aircraft will be a feasible approach to meet all the DRO, that is about 0.35 - 0.454 of the MTOW [27].

In addition to the benchmark study, an initial sizing calculation was also carried out. A mission profile was set to find initial dimensions, e.g., wing loading ($\frac{W}{S}$) and power-to-weight ratio ($\frac{P}{W}$), in the form of a matching chart. The mission profile with three-payload drop segments is presented in Fig.. 1.5.

For each mission profile, the weight fractions ($\frac{W_i}{W_{i-1}}$) were estimated for turboprop configuration. The values of $\frac{W_i}{W_{i-1}}$ are mostly taken from [27]. The empty weight was calculated for various wing areas S and used to iterate the fuel fraction needed to perform all the mission segments. Consequently, the maximum take-off can be estimated. In this analysis preliminary analysis, several assumptions were used as follow:

1. For each payload-drop segment, $\frac{1}{3}$ of the total retardant was dropped,
2. The cruising altitude is $\sim$ 6,000 m,
3. Take-off and landing are at 1,524 m altitude at +1.67°C,
4. The aspect ratio is assumed constant (AR=8),
5. The payload drop is assumed at $\sim$ 100 m altitude,
6. The loitering is assumed $\pm$ 30 minutes, and
7. The maximum velocity is assumed 210 $\frac{m}{s}$.

The result of the calculation is summarized in the matching chart shown in Figure. 1.6. The contour represents the MTOW range for various $\frac{P}{W}$ and W/S that can meet all the mission segments.

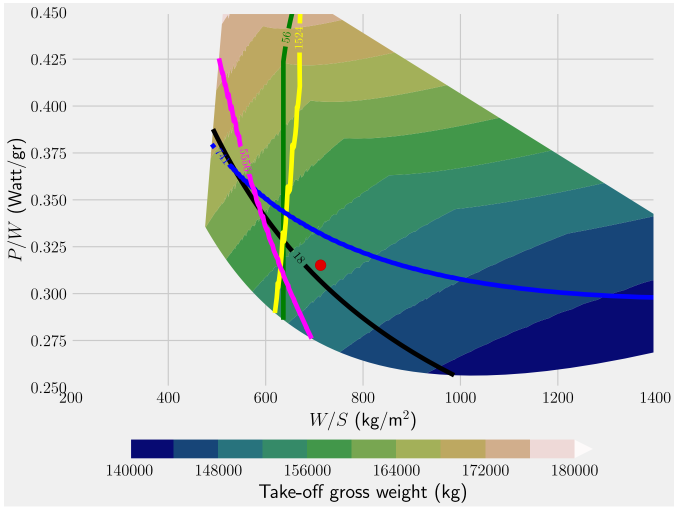

FIGURE 1.6: Wing Loading W/S vs Power-to-Weight P/W Ratio for various maximum take-off gross weight.

The yellow, magenta, blue, green, and black lines all represent the balanced field length (m), design ferry range with no payload (km), design radius with full payload (km), stall speed ($\frac{m}{s}$), and the rate of climb ($\frac{m}{s}$), respectively. The annotated values in the plot are the design objective that the airplane should achieve as stated in RFP, except for the green and black colored lines.

As the initial design point, the red dot was selected in the plot, that is, the maximum take-off weight $\approx$ 150,000 kg, where the corresponding wing loading $\dfrac{W}{S}$ and a power-to-weight ratio $\dfrac{P}{W}$ are 750 kg and 0.313 $\dfrac{Watt}{gr}$, respectively. Consequently, the wing planform area of $\approx$ 200 m^2 was selected as the guidelines to start our design and analysis. Following those values, the engine size will be chosen as well.

1.5 Design Configuration

Figure of Merits (FOM) was specified based on the featured qualities to be pursued. The list of FOM is shown in Table. 1.3. Each potential configurations of all aircraft sub-systems was graded in order to calculate Design Indexes (DIs) based on [28] using equations 1.1 and 1.2. The DIs were divided into design index maximum (DImax) and design index minimum (DImin). DImax comprises performance, flying qualities, maintainability, reliability, safety, operational availability, and producibility. DImin categories are production cost, operational cost, support cost, weight, and design period.

$$DI_{min} = p_1 PcI + p_2 OcI + p_3 ScI + p_4 WI + p_5 PdI \tag{1.1}$$

$$DI_{max} = p_6 PeI + p_7 FqI + p_8 MI + p_9 SI + p_{10} OaI + p_{11} PeI \tag{1.2}$$

Based on the calculation Of DImax and DImin, the final optimum design was chosen as the best candidate configuration for baruna-1 aircraft. The list of all the aircraft systems are tabulated in the Table. 1.4.

No	Figure of Merit (FOM)	Index	Priority (%)
1	Production Cost	p1	6
2	Operational Cost	p2	7
3	Support Cost	p3	7
4	Weight	p4	8
5	Period of design	p5	5
6	Performance	p6	10
7	Flying Qualities	p7	11
8	Maintainability	p8	9
9	Reliability	p9	11
10	Safety	p10	11
11	Operational availability	p11	9
12	Producibility	p12	6
Total			100

TABLE 1.3: Figure of Merits and each of their priority.

No	Index	Alternative Number	Configurations Constructing Code	1 A1-B3-C4-D2-E1-F1-G1-H2-I2-J1-K1-L1-M1-N1-O1-P1-Q1-R2-S2-T2-U1-V1-W5-X5-Y6-Z3-AA2-AB1-AC3-AD2-AE2-AF1-AG3-AH2-AI3-AJ3-AK2-AL3-AM3
1	A	1	Type	Conventional
2	B	3	Propulsion	Turboprop
3	C	4	Number of engines	Double twin-engine
4	D	2	Engine and aircraft cg	Tractor
5	E	1	Engine installation	Fixed
6	F	1	Engine location	Under wing
7	G	1	Number of wings	One-wing
8	H	2	Wing Geometry	Tapered
9	I	2	Dihedral angle	Non-dihedral
10	J	1	Wing sweep	Fixed sweep angle
11	K	1	Wing setting angle	Fixed setting angle
12	L	1	Wing placement	High-wing
13	M	1	Wing installation	Cantilever
14	N	1	Wing control surfaces	Aileron and Flap
15	O	1	High-lift devices	Trailing-edge flap
16	P	1	Wing-tail control surfaces	Conventional (elevator, aileron, and rudder)
17	Q	1	Tail or Canard	Tail
18	R	2	Tail type	T-shape
19	S	2	Vertical Tail (VT)	One VT at the fuselage
20	T	2	Horizontal tail control surfaces	Adjustable horizontal tail
21	U	1	Vertical tail control surfaces	Vertical tail and rudder
22	V	1	Power system	Fly-by-wire
23	W	5	Landing gear type	Multi-bogey
24	X	5	Shock Absorber	Oleo pneumatic
25	Y	6	Landing gear Layout	Dual Twin Tandem

26	Z	3	Landing gear	Retractable
27	AA	2	Fuselage	Single long-fuselage
28	AB	1	Material for structure	Full metal
29	AC	3	Equipment Installation	Semi Modular
30	AD	2	Way of Collecting Water	Land Tanker
31	AE	2	Number of Payload Tanks	Multitank
32	AF	1	Pump System	Hydraulic Pump
33	AG	3	Pressure Delivery System	Bleed Air
34	AH	2	Tank Internal Structure	Unbaffle
35	AI	3	Tank Material	Stainless Steel
36	AJ	3	Tank Head Shape	Semi Ellipsoidal Head
37	AK	2	Payload Tank Shape	Cuboid
38	AL	3	Retardant Delivery System	Pressurized Tank System
39	AM	3	Situational Awareness	Conventional + Thermal Imaging Devices

TABLE 1.4: Best suited configuration for Baruna-1

Chapter 2

Aerodynamics

In designing subsonic aircraft, getting the maximum lift-to-drag ratio $\left(\frac{C_L}{C_D}\right)_{\max}$ will improve the aircraft performance. Other lift-drag polar coefficients such as $\left(\frac{C_L^3}{C_D^2}\right)_{\max}$ and $\left(\frac{C_L}{C_D^2}\right)_{\max}$ are just as important as the $\left(\frac{C_L}{C_D}\right)_{\max}$ since they are also used to maximize or minimize other crucial parameters such as turning, gliding, and other performances. [29].

2.1 Fuselage Aerodynamics

The first approach ensures that all the carry-on payload, such as the retardant tank, fits inside the fuselage. Since baruna-1 aircraft used the semi-modular firefighting system, two candidates of retardant tank arrangement were considered, a series or parallel arrangement. Based on design fuselage parameters in Roskam [30] (see Figs. 2.1 and 2.2), several designs were constructed using OpenVSP to analyze its aerodynamics characteristics, specifically the drag coefficient C_D. Note that the parameter in d_f the Figure 2.1 is replaced by H in the analysis. From the potential configurations shown in Figure. 2.3, the important parameters of each fuselage are tabulated in the Table. 2.1.

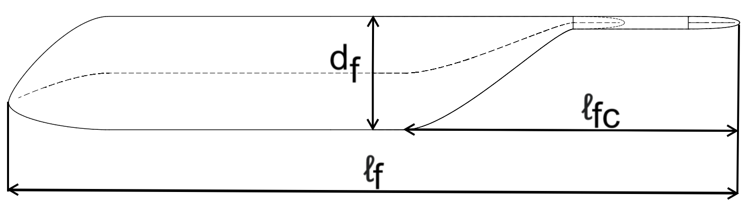

FIGURE 2.1: Fuselage Dimensions

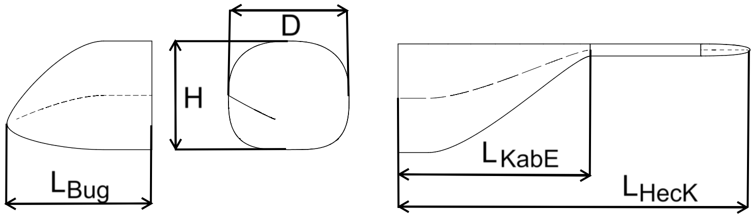

FIGURE 2.2: Cockpit and Empennage Dimensions

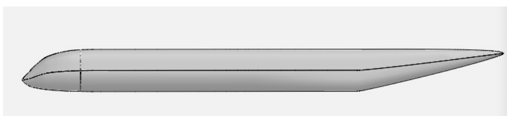

(a) Circular A Fuselage Series Arrangement

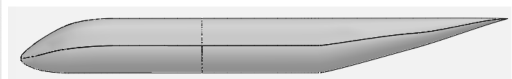

(b) Circular B Fuselage Series Arrangement

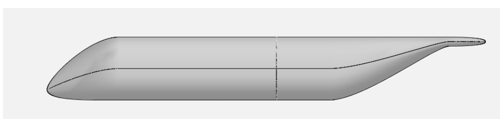

(c) Elliptical A Fuselage Parallel Arrangement

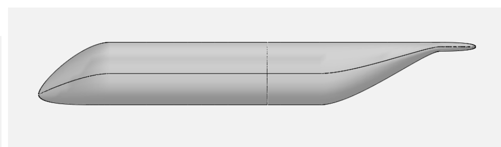

(d) Elliptical B Fuselage Parallel Arrangement

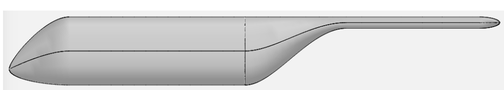

(e) Elliptical C Fuselage Parallel Arrangement

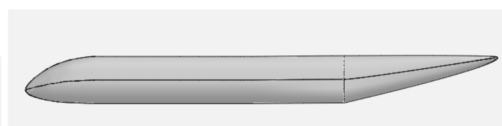

(f) Elliptical D Fuselage Parallel Arrangement

(g) Elliptical E Fuselage Parallel Arrangement

FIGURE 2.3: Fuselage arrangements consideration

	Circ-A	**Circ-B**	**Ellip-A**	**Ellip-B**	**Ellip-C**	**Ellip-D**	**Ellip-E**
L_f (m)	40.25	40.5	24.5	24.5	32.78	40.25	40.25
L_{fc} (m)	21	18	8.75	8.75	17.02	21	21
L_{KabE} (m)	6.65	8.55	7.95	7.95	6.76	7.11	7.11
L_{HeCk} (m)	12.25	15.75	14.64	14.64	10.26	13.1	13.1
L_{Bug} (m)	5.95	7.65	7.11	7.11	7.11	6.36	6.36
H (m)	3.5	4.5	3.5	3.5	4.5	4	4
D (m)	3.5	4.5	5	4.8	5	3.5	3.5
θ_{fc} (°)	11	14	25	25	31	14	16

TABLE 2.1: Fuselage Parameters

Considering the movement of the center of gravity (C.G) of the aircraft during the payload-drop mission, a series retardant tank arrangement is out of option, although, from an aerodynamics point of view, this configuration is favorable. The decision on fuselage configuration is on the parallel retardant tank arrangement, which gives the lowest C_{D0} value. The C_{D0} value was calculated using OpenVSP's parasite drag solver, and the results are summarized on Table. 2.2.

	Ellip-A	**Ellip-B**	**Ellip-C**
$\mathbf{C}_{D0}$ (100% Laminar)	0.00001	0.00001	0.00023
$\mathbf{C}_f$ **(1e^{-3})**	0.11	0.11	0.11
C_D	0.000176	0.000172	0.000553

TABLE 2.2: Fuselage Aerodynamic Features

From Table. 2.2, the fuselage with the lowest C_{D0} is the Ellip-A and -B fuselage. However, when the retardant tank was installed, there was no room for installing the fire fighting system. As a result, the Ellip-C fuselage was chosen as the retardant tank and the fire fighting system fits perfectly inside the fuselage. The value of C_{D0} for this configuration is 5.53×10^4.

2.2 Wing Aerodynamics

2.2.1 Airfoil Selection

During the airfoil selection process, three airfoil candidates were chosen. These airfoils can be seen in Figure. 2.4.

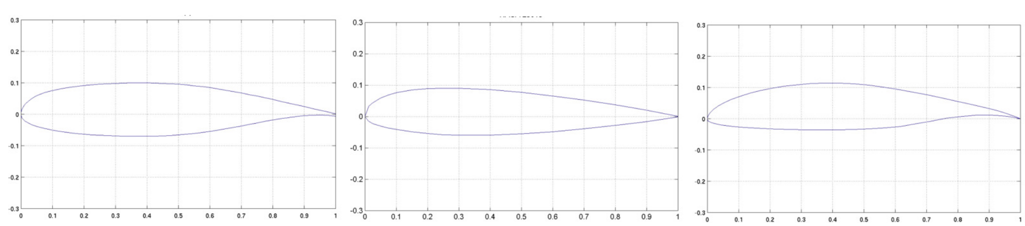

(a) MS(1)-0317 Airfoil (b) NACA 23015 Airfoil (c) NLF(1)-0215F Airfoil

FIGURE 2.4: Airfoil candidates

From the three candidates shown in Figure. 2.4, the MS(1)-0317 airfoil is chosen for Baruna-1 due to its volume and aerodynamics profile at higher subsonic speed. The aerodynamics characteristics of the MS(1)-0317 airfoil are shown in Figure. 2.5 (a) through (e) for various Reynolds numbers in the plot of $c_l - \alpha$, $c_l - c_d$, $c_m - \alpha$, $c_d - \alpha$ and $\frac{c_l}{c_d} - \alpha$.

2.2.2 Wing Geometry

From initial sizing analysis in section 1.4, the approximated wing planform area for MTOW 150,000 kg is 200 m^2. The aspect ratio AR for Baruna-1 was based on other aircraft competitors, which ranges from $6 - 12$. For subsonic turboprop engines, the AR range usually lies within $8 - 10$. From the empirical equation from Raymer [27], the increment of aspect ratio is proportional with the weight of the wing for general aviation aircraft (see Eq. 2.1). Therefore, the $AR = 10$ will add 14% of the total wing weight W_w. Based on this information, the $AR = 8$ was selected for Baruna-1 configuration. Consequently, the wingspan of Baruna-1 is 40 m. The wing taper ratio λ was selected based on the elliptical lift distribution as shown in Fig. 2.6. Hence, for Baruna-1, a taper ratio of 0.5 was used for our wing design. Other parameters of wing planform are specified in Table. 2.3.

Based on these parameters, five potential wing candidates were made as depicted in Figs. 2.7 (a) through (e), and their related parameters can be seen in the Table. 2.4.

Based on the Table. 2.4, out of the five candidates, ST4 with Wingbox MS(1)-0317 has the largest amount of volume with a value of 119.52 m^3. Since we want the wing to have as much volume as possible in order to be able to carry a larger volume of fuel in the wings, the ST4 with Wingbox MS(1)-0317 was chosen. The C_{D0} values between each wing configuration does not have that much of a difference as well. The aerodynamics characteristic of the selected configuration is also confirmed by CFD analysis (using OpenFOAM software) with laminar flow assumption for $\alpha = 0$ deg at $Re = 6.7 \times 10^6$, $M = 0.58$. The flow around the wing and the convergence results of aerodynamics forces are shown on Figure. 2.8. At time step 500, all the aerodynamics coefficient reached convergence where a C_L, C_D and C_{MLE} values are 0.2722, 0.008922 and -0.1305, respectively. Note that the drag coefficient from OpenFOAM and OpenVSP only slightly different.

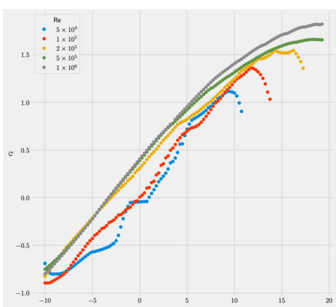

(a) cl vs α for Various Reynolds Number

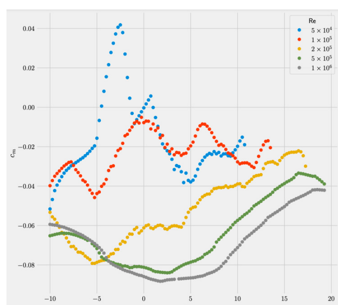

(b) cm vs α for Various Reynolds Number

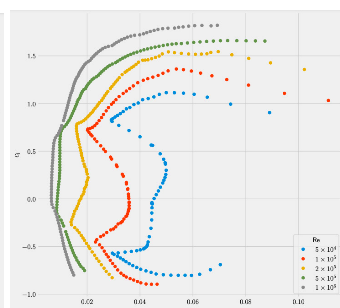

(c) cl vs cd for Various Reynolds Number

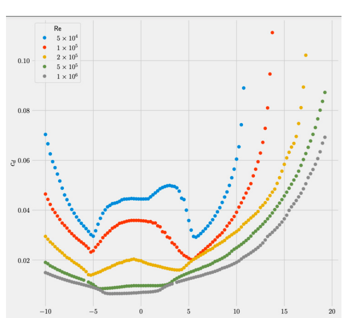

(d) cd vs α for Various Reynolds Number

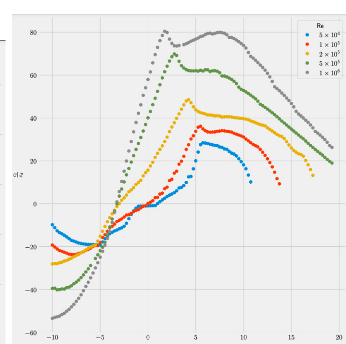

(e) $\frac{cl}{cd}$ vs α for Various Reynolds Number

FIGURE 2.5: MS(1)-0317 airfoil characteristics

$$W_w \propto AR^{0.6} \tag{2.1}$$

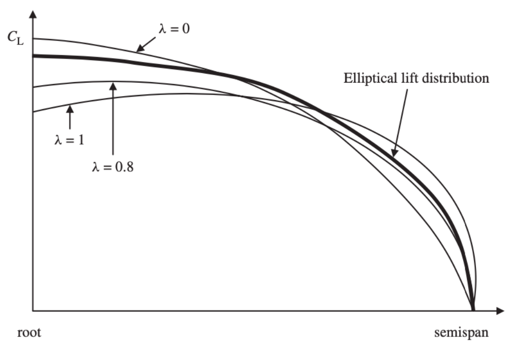

(a) Various tapers

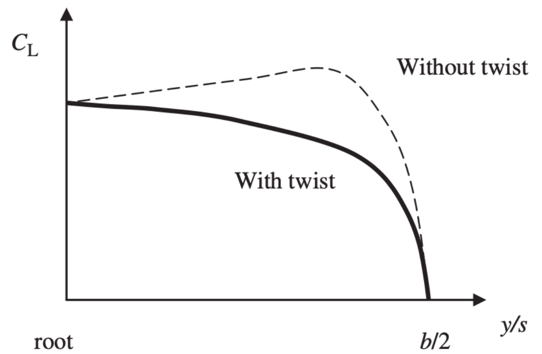

(b) With twist

FIGURE 2.6: Lift Distribution of various taper (a) and with twist (b) [28]

Parameter	Value
Wing Planform Area (S_{ref}) (m^2)	200.00
Wing Span (m)	40.02
Aspect Ratio	8.00
Taper Ratio	0.50
Twist Angle (°)	-2.00
Dihedral Angle (°)	-2.00

TABLE 2.3: Wing Parameter

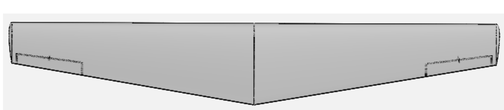

(a) ST4 Wing with NACA 23015 Airfoil

(b) MP4 Wing with NACA 23015 Airfoil

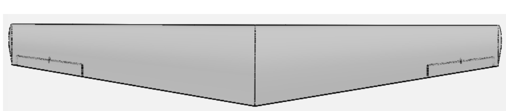

(c) ST4 Wing with NLF-0215F Airfoil

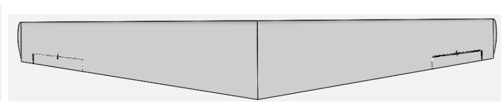

(d) ST4 Wing with MS(1)-0317 Airfoil

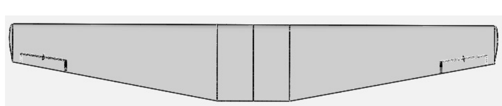

(e) ST4 Wing with Wingbox and MS(1)-0317 Airfoil

FIGURE 2.7: Potential wing candidates

	ST4 NACA 23015	MP4 NACA 23015	ST4 NLF-0215F	ST4 MS(1)-0317	ST4 with Wingbox MS(1)-0317
C_{D0} (100% laminar)	0.00074	0.00074	0.00074	0.00079	0.00089
C_f ($1e^{-3}$)	0.23	0.23	0.23	0.23	0.27
f (m^2)	0.1487	0.1481	0.1484	0.1572	0.1772
MAC (m)	5.00	5.52	5.00	5.00	5.60
Theoretical Area (m^2)	415.30	409.27	414.54	419.21	418.56
Theoretical Volume (m^3)	106.14	72.62	99.55	118.98	119.52
Wetted Area (m^2)	415.30	409.27	414.54	419.21	418.56
Wetted Volume (m^3)	106.14	72.62	99.55	118.98	119.52

TABLE 2.4: Wing aerodynamics parameters

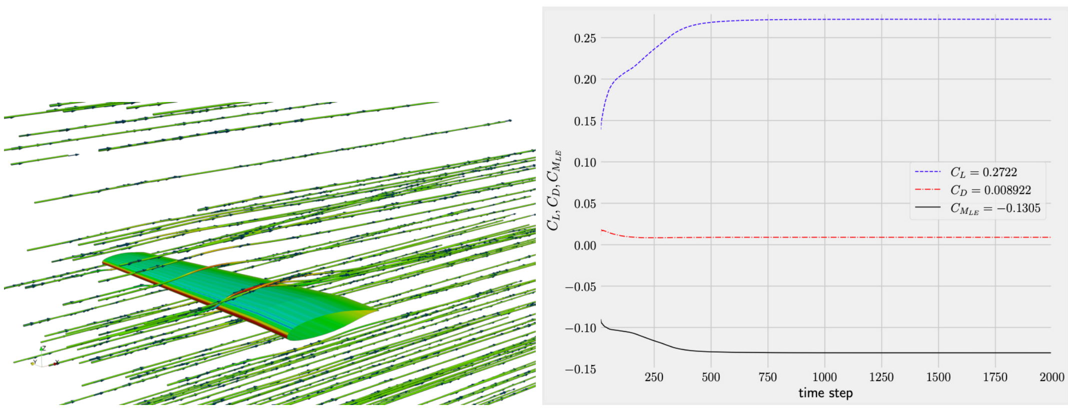

(a) Flow around wing.

(b) C_L, C_D, C_{MLE} for each time step.

FIGURE 2.8: CFD results for Baruna-1 wing configuration.

2.2.3 Estimation of $\alpha_{\mathbf{max}}$

The α_{max} of the aircraft was estimated from MS(1)-0317 airfoil profile and the distribution of lift coefficient along the wing. Experimental data taken from NASA Technical report [31] showed that at $Re = 12 \times 10^6$, this airfoil underwent a near-stall condition of $\alpha = 19^\circ$ and $c_{l_{max}} \approx 2.0$.

From geometry constructed in the OpenVSP software, at cruise configuration (clean configuration), the spanwise lift distributions were analyzed for various angles of attack α. This computation was done using linear wing theory, i.e., Vortex Lattice Method (VLM). The result of selected α near stall region, can be seen in Figure. 2.9. The plot revealed that the onset of the stall of the wing occur at $\alpha > 17^\circ$. At $\alpha = 18^\circ$, some region around the mid-wing reached the $c_{l_{max}} = 2.0$. Therefore, in this preliminary analysis, for cruise configuration, the estimated α_{max} of Baruna-1 is 17°.

2.2.4 Estimation of C_{L_α} and $C_{L_{max}}$

This analysis was also using VLM in OpenVSP. The coefficient of lift C_L of the aircraft at various α for clean configuration is presented in Figure.2.10 at constant Reynolds number $Re = 1 \times 10^8$ and constant Mach number $M = 0.5$. The C_L values obtained from the output was also confirmed by manual calculation,

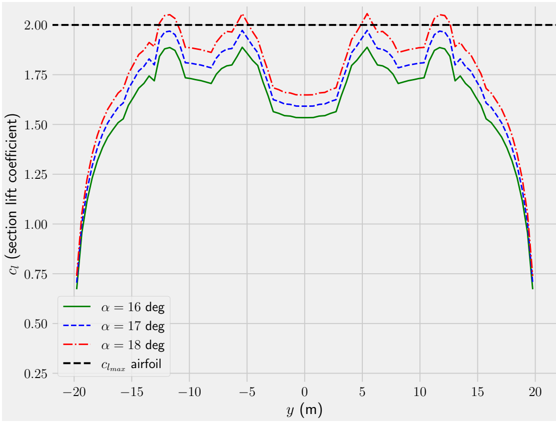

FIGURE 2.9: The c_l distribution in spanwise direction for various α (AoA).

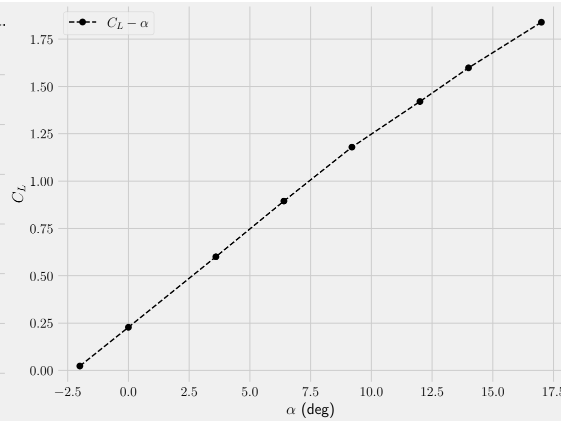

FIGURE 2.10: The C_L vs α.

using Eq. 2.2, from the available data of the spanwise section lift coefficient distribution. Here, the $c_l(\eta)$ and $c(\eta)$ are the lift coefficient and chord length at particular spanwise location, respectively.

$$C_L = \frac{1}{S}\int_0^{2y/b} b\, c_l(\eta)\, c(\eta)\, d\eta \tag{2.2}$$

Small discrepancies occurred between the calculated C_L from spanwise c_l distribution and the output C_L value from VSPAero analysis, i.e., at 12°, the calculated C_L and the output C_L values were 1.4 and 1.42, respectively, which give $\pm 1.4\%$ error. These discrepancies were also shown for other angle of attack conditions. Nevertheless, it can be neglected due to the small difference of $\pm 1 - 2\%$. The results from the direct output of VSPAero were summarized (see Figure. 2.10) and were also used in the performance analysis. We should note that at the vicinity of $\alpha_{max} = 17°$, the result from linear theory such as VLM and panel method deviated significantly from the experiment or CFD results using the turbulence model.

From the computation, The C_{L_α} or $\dfrac{dC_L}{d\alpha}$ for this aircraft is 0.10478/deg or 6.0086/rad at the linear region of $\alpha = -2° - 10°$. The value of $C_{L_{max}}$ is approximately around 1.839.

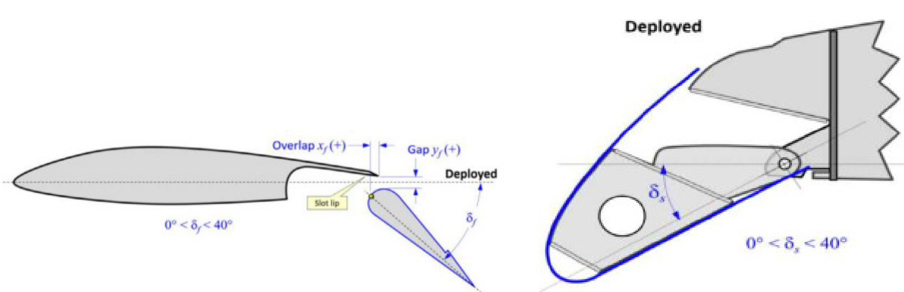

(a) (b)

FIGURE 2.11: Schematic of extended fowler flap and drop nose slat.[32]

To meet other performance requirements, the $C_{L_{max}}$ must be larger than that shown in Figure.2.10. The high-lift devices (HLD) are needed to achieve higher value of the $C_{L_{max}}$. Therefore, single-slotted

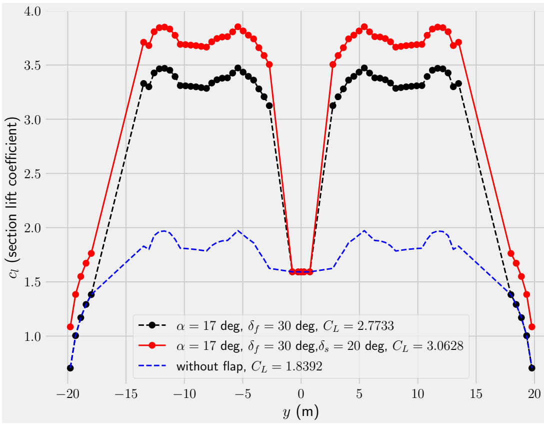

FIGURE 2.12: The c_l distribution for various configuration.

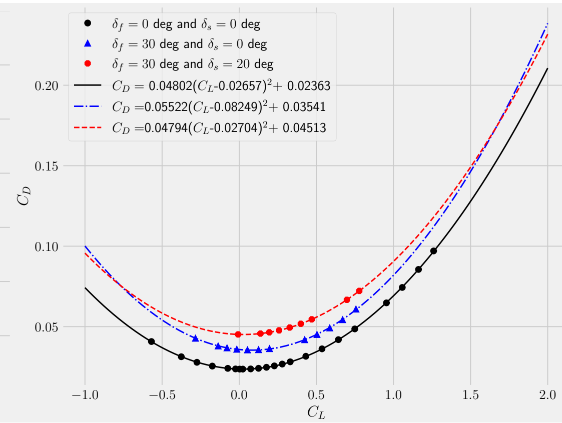

FIGURE 2.13: The C_D vs C_L (drag polar) of the aircraft.

fowler flap was chosen due to its effectiveness. Pátekk and Zabloudil [33], showed that the MS(1)-0317 with fowler flap configuration can add Δc_l to the sectional lift coefficient in the range of $1.28 - 1.58$ at $Re = 1.65 \times 10^6$. The increment is highly dependent with the y_f and x_f parameters (see Figure. 2.11). For Baruna 1, the selected values of y_f and x_f are $0.03c$ and $0.002c$, respectively. The chord length of the flap is $c_f = 0.3c$, and the span lies within range of $\pm 0.7b/2$. It is known that the implementation of such devices do not alter the α_{max}, so the $C_{L_{\alpha=17^o}}$ would still be the $C_{L_{max}}$ of this aircraft.

Additionally, a simple slat, i.e. droop nose; was chosen due to its simplicity and light weight. This configuration allows the increment of $\Delta c_{l_{max}} = 0.58$ and $\Delta\alpha_{stall} = 7.8$. In this aircraft, the dimension of the slat is $c_s = 0.12c$. Since limited study was carried out for airfoil MS-0317, the estimation of $c_{l_{max}}$ and α_{stall} for the airfoil was based on the statistical data of various slat types[32]. The equation used are Eq. 2.3 and Eq. 2.3, where $\delta_{s_{ref}}$ and $c_{s_{ref}}$ are the deflection angle and chord length of the slat respectively. For airfoil MS(1)-0317, at $\delta_s = 20°$, the sectional lift coefficient c_{lmax} and α_{max} are 2.38 and 22.2 deg, respectively.

$$c_{l_{max_{slat}}} = c_{l_{max}} + \Delta c_{l_{max}} \left(\frac{\delta_s}{\delta_{s_{ref}}}\right)\left(\frac{c_s}{c_{s_{ref}}}\right) \tag{2.3}$$

$$\alpha_{stall_{slat}} = \alpha_{stall} + \Delta\alpha_{stall} \left(\frac{\delta_s}{\delta_{s_{ref}}}\right)\left(\frac{c_s}{c_{s_{ref}}}\right) \tag{2.4}$$

The comparison of c_l distribution along the span for clean, flap extended, and all HLD (flap and slat) extended is shown in Figure. 2.12. By integrating the spanwise coefficient of lift distribution with Eq. 2.3, the C_L for various configuration can be estimated.

2.2.5 Drag polar

The lift and drag profile of several configurations of the aircraft are plotted in Figure. 2.13. A correction of drag due to the deployment of HLD were taken into account, that is $\Delta c_d = 0.004$ for flap correction and no significant correction due to the extension of droop nose slat [32]. The discretized data was optimized for quadratic function using curve-fitting. The important parameters for performance analysis are tabulated in Table.2.5.

Case	C_{D_o}	k	C_{L_o}
$\delta_f = 0$ deg, $\delta_s = 0$ deg	0.02363	0.04802	0.02657
$\delta_f = 30$ deg, $\delta_s = 0$ deg	0.03541	0.05522	0.08249
$\delta_f = 30$ deg, $\delta_s = 20$ deg	0.04513	0.04794	0.02704

TABLE 2.5: Drag polar parameters.

2.3 Tail Design

From design configuration in Sec. 1.5, Baruna-1 tail is the T-tail type. This configuration was chosen because the tail would be placed in a location where it could avoid regions of wing wake, wing downwash, wing vortices and engine exit flow which allows the horizontal tail to provide a much higher efficiency and a safer structure [28]. Furthermore, as a result of avoiding the regions stated above, it lessens the vibration and buffeting of the tail which leads to the lessening of fatigue problems [28]. additionally, it also helps the tail to have a smaller area for the horizontal and vertical tail [28]. This means that fatigue maintenance costs can be reduced. Although using a T-tail configuration requires the vertical tail to be stronger due to the bending moment transferred from the horizontal tail which results in a heavier structure for the vertical tail [28], it would only require us to pay more in the manufacturing process the aircraft. This way we can reduce the maintenance cost as stated above when using this configuration compared to others. Deep stall is also one of the concerns when using this configuration, however, this can be countered by implementing a stick pusher to the control column / stick of the airplane or by installing angle of attack (AoA) limiters [34].

The horizontal tail setting configuration selected is the fixed setting. The reason for this is that by using a fixed horizontal tail, the airplane will be lighter which means that it would need less money to manufacture which also leads to lower maintenance cost [28]. Not only it is structurally easier to design, which would take less time to make, it is also more reliable since it has less moving components which reduces the risk of failure [28].

Both vertical and horizontal tail has a sweep angle of 30° with no dihedral angle applied to the horizontal tail. The taper ratio selected is 5.5 for both vertical and horizontal tail and their aspect ratios are 1.2 and 4.5 respectively. The tabulated form of these parameters can be seen on Table. 2.6 and Table. 2.7.

Parameter	**Value**
Vertical Tail Planform Area (S_v) (m^2)	31.32
Horizontal Tail Span (m)	6.13
Aspect Ratio	1.20
Taper Ratio	0.55

TABLE 2.6: Vertical Tail Parameter

Parameter	**Value**
Horizontal Tail Planform Area (S_h) (m^2)	48.93
Horizontal Tail Span (m)	14.84
Aspect Ratio	4.50
Taper Ratio	0.55

TABLE 2.7: Horizontal Tail Parameter

The airfoil used for the horizontal and vertical stabilizer of Baruna-1 is the NACA 0012 airfoil. Its shape and aerodynamics characteristics can be seen on Figures. 2.14.

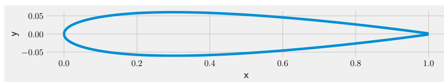

(a) NACA 0012 Airfoil

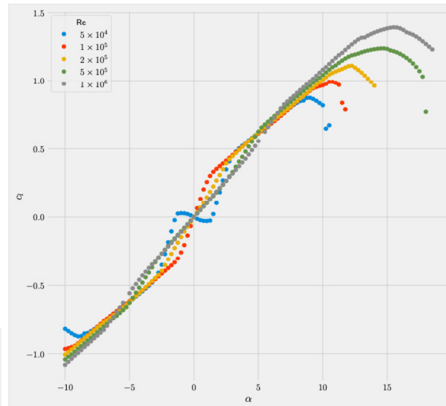

(b) cl vs α for Various Reynolds Number

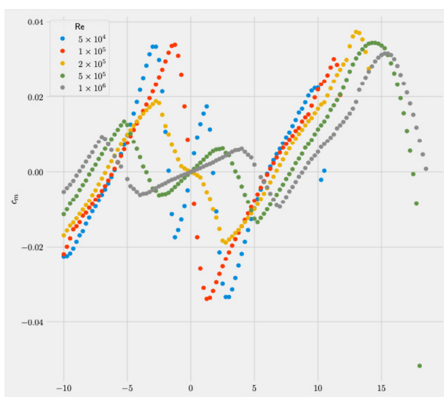

(c) cm vs α for Various Reynolds Number

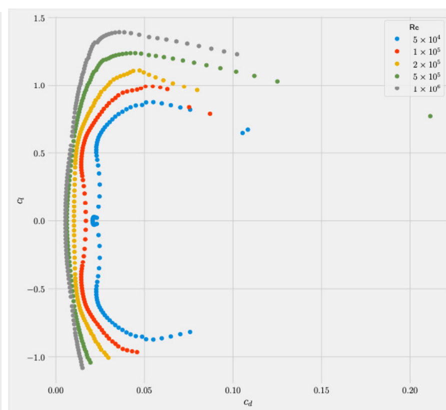

(d) cl vs cd for Various Reynolds Number

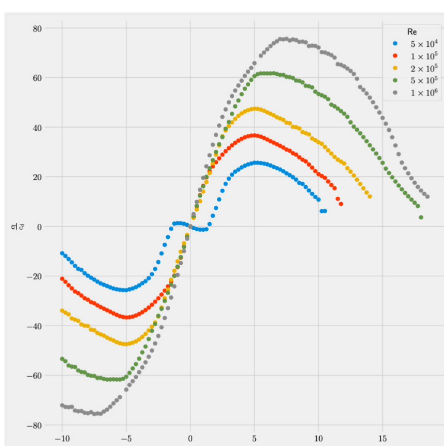

(e) cd vs α for Various Reynolds Number

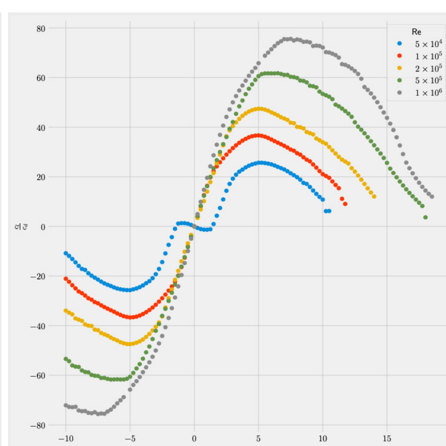

(f) $\frac{cl}{cd}$ vs α for Various Reynolds Number

FIGURE 2.14: NACA 0012 airfoil characteristics

Chapter 3

Structures

3.1 Aircraft Loads

The load factor limit was set according to FAR 25.337, where the design speed must be complied to FAR 25.335. All the values presented in Figure. 3.1 was analyzed at sea-level condition and maximum take-off weight. The stall speed V_S, maneuvering speed V_A, cruise speed V_C, and dive speed V_D are 54 $\frac{m}{s}$, 86 $\frac{m}{s}$, 151 $\frac{m}{s}$, and 236 $\frac{m}{s}$, respectively. The V_s was estimated for aircraft with extended flap and $V_A > V_S\sqrt{n_{+limit}}$. The maximum cruise speed is $\approx$ 189 m/s based on the avalaible power at sea-level condition. The diving velocity was selected such that $\frac{V_C}{M_C} < 0.8\frac{V_D}{M_D}$.

At higher altitude condition, a consideration for maximum cruise speed was also taken in regard of the critical Mach number M_{cr} of sectional wing / airfoil. The estimation of M_{cr} was made using Prandtl-Glauert corection factor $C_p = \frac{C_{p,0}}{\sqrt{1-M_\infty^2}}$ with isentropic flow assumption. As a reference, minimum $C_{p,0}$ at $\alpha = 0$ for airfoil MS(1)-0317 at $Re = 9 \times 10^6$ was evaluated to estimate the M_{cr} (see the pressure distribution data in [31]). Regarding this, the computed M_{cr} is ~0.6332.

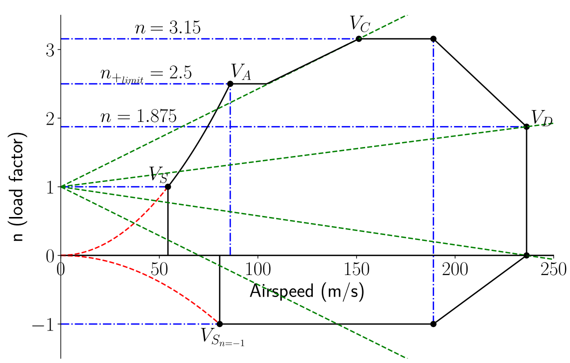

FIGURE 3.1: V-n and gust diagram at sea-level.

3.2 Structural configuration and dimension

According to the FAR25, the structural configuration of this aircraft must be able to sustain a load of -1 to +3.15. For the ultimate load, the load factor in Figure. 3.1 must be multiple with the factor of safety 1.5. Nevertheless, for Baruna-1, the dimension of the main part of the structure, such as spar, rib, stringer, longeron, and skin, were estimated to sustain the load below the fatigue strength limit. At the midsection of half span of the wing, at fuselage center of mass, and in vicinity of the retardant tank are some of the region where the load is at maximum.

3.3 Structures

The Fuselage, wings, empennage, landing gear, and powerplant are all substructures of the aircraft structure. Structural analysis was performed to identify the ideal Fuselage, Wing, and Tail structural elements, while CAD models were utilized to estimate the aircraft structure's forces, moments, and torques.

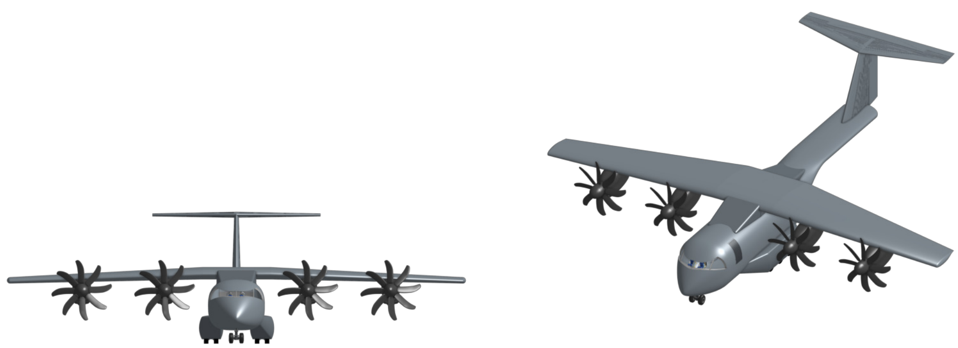

(a) (b)

FIGURE 3.2: Baruna-1 Final Design.

3.4 Initial Sizing

After the fixed Fuselage and Wing design were set, the initial sizing of the aircraft structure was then calculated. An aircraft's initial sizing sets its rough size and weight depending on the targeted requirements. The detailed specifications of the sub-structures used for the aircraft are defined in this section.

3.4.1 Fuselage

All of the preliminary sizing and spacing of the Fuselage are based on Roskam [30]. The fuselage structure sizing is provided in Table. 3.1 and visualized in Figure. 3.3

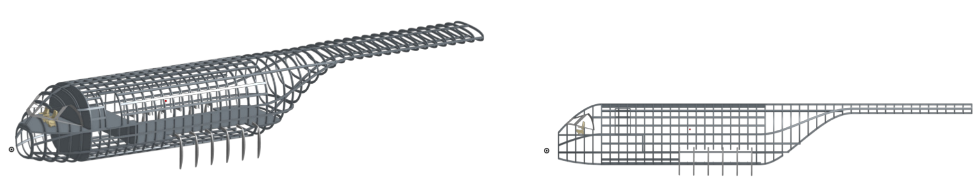

(a) Fuselage Substructure ISO View (b) Fuselage Substructure Side View

FIGURE 3.3: Fuselage structure views.

PARTS	SIZING (mm)
Frame Spacing	558.88
Frame Depth	74.471
Longeron Spacing	∼12
Skin Thickness	0.35
Fuselage Length	5,000
Fuselage Width	4,500

TABLE 3.1: Fuselage Detail Sizing

3.4.2 Wing

The Wing structure sizing is provided in Table.3.2 and visualized in Figure. 3.4. The primary and aft spars are located at 0.2c and 0.65c, respectively. After some calculations, the aircraft's number of spars and longerons were determined [30]. We decided to use two spars and 14 longeron ribs.

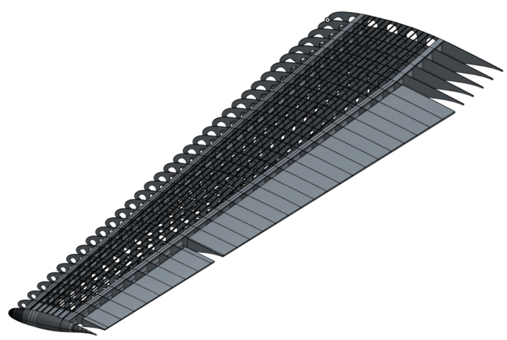

FIGURE 3.4: Wing Substructure.

PARTS	SIZING (mm)
Rib Spacing	600 [30]
Rib Thickness	1
Stringer Spacing	152.4 [35]
Skin Thickness (Uniform)	0.8
Spars Web Thickness	1
Spars Flange Thickness	3
Stringers Thickness	1.5

TABLE 3.2: Wing Detail Sizing.

3.4.3 Tail

The tail structure sizing is provided in Table. 3.3 and visualized in Figure. 3.5 As shown in the table, all substructure configurations and sizing are identical to the Wing substructure sizing.

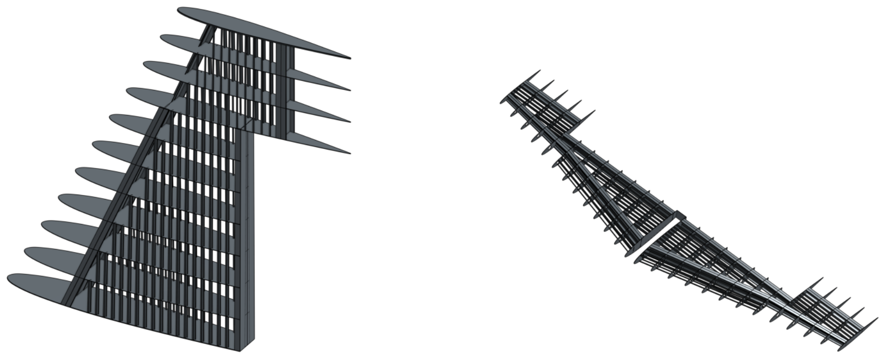

(a) Vertical Stabilizer (b) Horizontal Stabilizer

FIGURE 3.5: Tail Substructure.

PARTS	SIZING (mm)
Rib Spacing	600 [30]
Rib Thickness	1
Stringer Spacing	152.4
Skin Thickness (Uniform)	0.8
Spars Web Thickness	1
Spars Flange Thickness	3
Stringers Thickness	1.5

TABLE 3.3: Tail detail sizing.

3.5 Materials

After doing some calculations using the specific data for each material property provided in ASM [36], various materials were chosen for different structure / substructures parts,

STRUCTURE	SUBSTRUCTURE	MATERIAL
Fuselage	Skin	Al 2024
	Frames	Al 2024
	Longerons	Titanium Alloy Grade 5
	Stringers	Titanium Alloy Grade 5
Wing	Skin	Al 2024
	Ribs	Al 2024
	Spars	Al 2024
	Stringers	Titanium Alloy Grade 5
	Wing Mounting	Al 2024

Tail	Skin	Al 7075
	Ribs	Al 7075
	Stringers	Al 7075
	Spars	Al 7075
Wheel Housing	Skin	Al 2024
	Ribs	Al 2024

TABLE 3.4: Baruna-1 Substructures Material List.

Because the tail would highly be under stressed, AL 7075 was chosen since it contains more zinc, making it one of the strongest and most complex alloys. Furthermore, it is highly corrosion-resistant [36].

Although it is much lighter than AL 7075, its high strength and fatigue resistance and outstanding corrosion resistance make AL 2024 ideal for components and structures where a high strength-to-weight ratio is desired. Thus, AL 2024 was chosen for both fuselage and wing sub-structures [36].

Titanium, a lightweight, robust and corrosion-resistant metal; is widely used to construct airplane structures [37]. In order to minimize aircraft weight as much as possible, titanium is the optimum material for particular fuselage and wing construction sections. The specific type of titanium alloy used in Baruna-1 would be Titanium Grade 5 (Ti-6Al-4V) since it is highly corrosion-resistant, lightweight, strong, and able to withstand high temperatures. [38]

3.6 Fuel Tank

The tanks are subjected to be dispersed across the wing and fuselage to make the most of aircraft fuel tank placements, with primary fuel tanks at the Wing and secondary fuel tanks at the Fuselage.

After researching aluminum materials, AL 5052 was determined to be the most suitable material to be used for fuel tanks, due to its lightweight, large in volume, corrosion-resistant (hence the need for regular cleaning), and easy to weld while remaining strong properties [36].

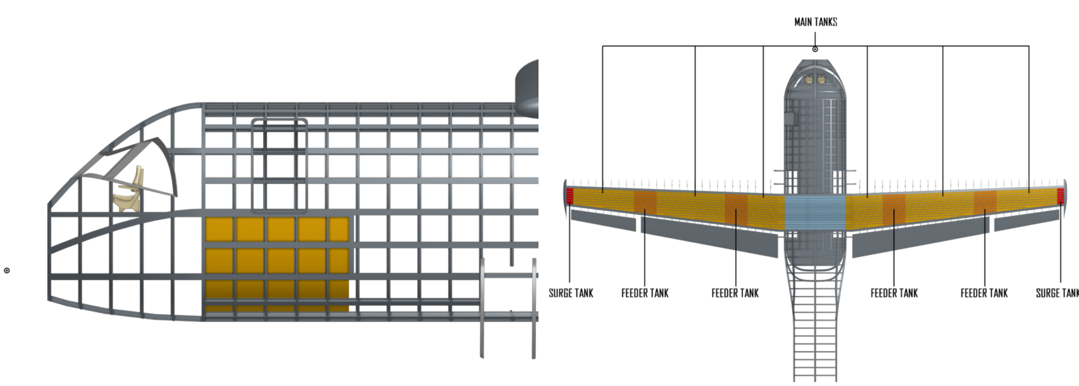

(a) Secondary Fuel Tank at Fuselage (b) Primary Fuel Tank at Wing

FIGURE 3.6: Baruna-1's fuel tanks.

3.7 Requirements for Structural Load

FAR 25 [35] defined the specified structural strength limit as shown below:

§ **25.337 Limit maneuvering load factors.** [39]

(a) Except where limited by maximum (static) lift coefficients, the airplane is assumed to be subjected to symmetrical maneuvers resulting in the limit maneuvering load factors prescribed in this section. Pitching velocities appropriate to the corresponding pull-up and steady turn maneuvers must be taken into account.

(b) The positive limit maneuvering load factor n for any speed up to Vn may not be less than 2.1+24,000/ (W +10,000) except that n may not be less than 2.5 and need not be greater than 3.8—where W is the design maximum takeoff weight.

(c) The negative limit maneuvering load factor—

i. May not be less than ¥1.0 at speeds up to VC; and

ii. Must vary linearly with speed from the value at VC to zero at VD.

(d) Maneuvering load factors lower than those specified in this section may be used if the airplane has design features that make it impossible to exceed these values in flight.

[Doc. No. 5066, 29 FR 18291, Dec. 24, 1964, as amended by Amdt. 25–23, 35 FR 5672, Apr. 8, 1970]

§ **25.335 (a) Design cruising speed, VC. For VC, the following apply.** [40]

(a) The minimum value of VC must be sufficiently greater than VB to provide for inadvertent speed increases likely to occur as a result of severe atmospheric turbulence.

(b) Except as provided in §25.335(d)(2), VC may not be less than VB + 1.32 U^{REF} (with 32 U^{REF} as specified in §25.341(a)(5)(i)). However VC need not exceed the maximum speed in level flight at maximum continuous power for the corresponding altitude.

(c) At altitudes where VD is limited by Mach number, VC may be limited to a selected Mach number.

[Doc. No. 5066, 29 FR 18291, Dec. 24, 1964, as amended by Amdt. 25–23, 35 FR 5672, Apr. 8, 1970; Amdt. 25–86, 61 FR 5220, Feb. 9, 1996; Amdt. 25–91, 62 FR 40704, July 29, 1997]

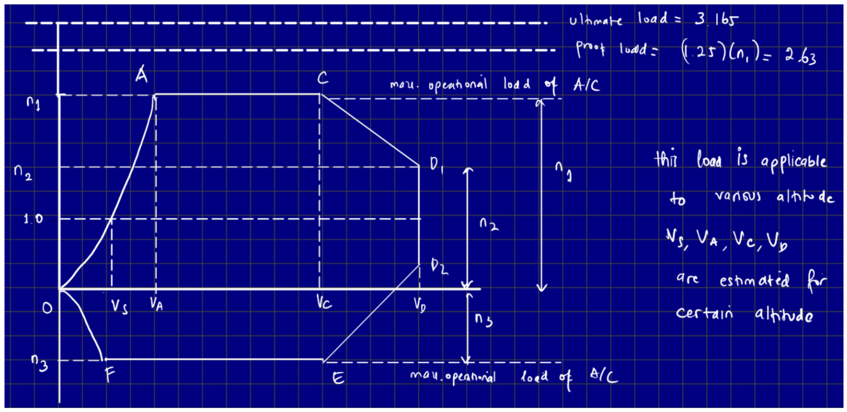

FIGURE 3.7: Baruna-1 Flight Envelope

Based on MTOW, engine performance, and wing loading, The V_s, V_a, and V_d are the stall speed, minimum cruising speed, maximum cruising speed, and dive speed. The V_s. is estimated for an aircraft with extended flaps, while Va is determined based on FAR 25.335, V_a ¿ V_{sn}. The maximum cruising speed (V_c) at sea level is 195 $\frac{m}{s}$. The maximum cruising speed (V_c) was determined using the engine's maximum continuous output, around 7,971 kW per engine. The computation was performed using the equation below:

$$V_{cmax} = \sqrt{\frac{T}{\rho C_{D0} S}\left[1 \pm \sqrt{4\frac{C_{D0}}{\pi ARe}\left(\frac{W}{T}\right)}\right]} \tag{3.1}$$

The critical Mach number (M_{cr}) of the airfoil was also regarded. The Prandtl-Glauert correction factor was used to estimate the M_c under the assumption of isentropic flow shown in the equation below:

$$C_p = \frac{C_{p,0}}{\sqrt{1 - M_\infty^2}} \tag{3.2}$$

The minimal C_{p0} at α = 0 for airfoil MS-0317 at Re = 9 x 10^6 was used as a reference. In this case, the M_{cr} is 0.633 circa, equivalent to around 215 $\frac{m}{s}$ at sea level. This number is greater than the V_{Cmax} determined by the maximum continuous power. The dive velocity was set to approximately be 240 $\frac{m}{s}$ so that $\frac{V_c}{M_c}$ ¡ 0.8 $\frac{V_d}{M_d}$.

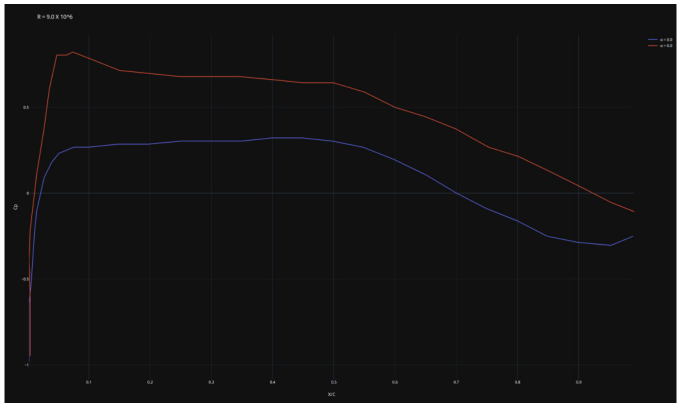

FIGURE 3.8: $\frac{X}{C}$ vs C_p Plot

3.8 Structural Configurations and Dimensions

According to the FAR25, this aircraft's structural configuration must withstand loads ranging from 1 to +3. In this regard, the dimensions of the critical structural components, such as the spar, rib, stringer, longeron, and skin, were evaluated to withstand loads below the fatigue strength limit of AL-7075, which is approximately 159 MPa.

The following is a list of the form and area of various essential configurations in vital regions where the load is at its peak:

PART	SHAPE	AREA (mm^2)
Wing Rib (Half span of the wing)		3,151,240.766
Wing Spars & Web (Half span of the wing)		11,795.129
Wing stringer (Half span of the wing)		60.975
Frame (at fuselage center of mass)		461.33

TABLE 3.5: Detail Configuration of Various Parts in Vital Regions

3.9 Weight Estimation

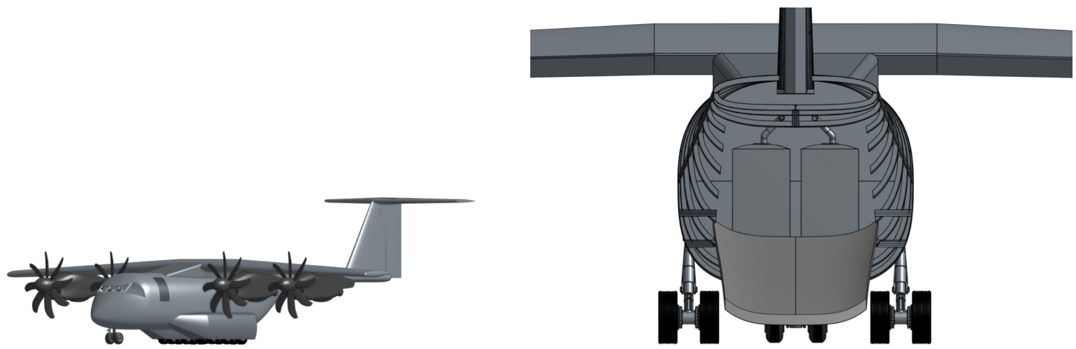

(a) Baruna-1 full components. (b) Rear cargo door.

FIGURE 3.9: Baruna-1 full components depiction (a) and the rear cargo door (b)

The weight estimations are based on the methods found in Roskam's Airplane Design Vol. 8 [30]. Table. 3.6 listed the design parameters determined in this chapter.

NO	COMPONENTS	WEIGHT (kg)
1	Engine (x4)	7,840.0
2	Landing Gears (Nose and Main)	5,116.0
3	Retardant System	6,863.0
4	Retardant	36,800.0
5	Fuel Tank (Wing)	568.891
6	Fuel (Wing)	30,611.969
7	Fuel Tank (Fuselage)	182.307
8	Fuel (Fuselage)	20,609.851
9	Fuselage Substructure	24,782.61
10	Fuselage Skin	153.899
11	Main Horizontal Wing Substructure (Aileron, etc.)	3,290.221
12	Main Horizontal Wing Skin	917.272
13	Tail Horizontal Wing Substructure	1,139.376
14	Tail Horizontal Wing Skin	
15	Tail Vertical Wing Substructure	609.802
16	Tail Vertical Wing Skin	
17	Rear Cargo Door	31.001
18	Fuselage Door	27.112
19	Wing Mounting	109.271
20	Wheel Housing	1,110.422

21	Air Conditioning, Deicing System Weight (W_{api})	1,010.18
22	Auxiliary Power Unit Weight (W_{apu})	566.172
23	Electrical System Weight (W_{els})	332.392
24	Flight Control System Weight (W_{fc})	683.569
25	Instrumentation, Avionics, and Electronics System Weight (W_{iae})	591.965
26	Paint Weight (W_{pt})	424.628
27	Crew x2	162.0
28	Pilot Seat x2	26.1
TOTAL		**144,560.0**

TABLE 3.6: Baruna-1's weight estimation.

All Class II Fixed Equipment Weight Estimations are calculated using the bomber method's Torenbeek and military aircraft approach [30]. From the data, the EMTOW and MTOW are determined to be 107.760 tons and 144.560 tons, respectively.

3.10 Cockpit Design

Baruna-1 is a manned aircraft, hence a cockpit is required to accommodate the flight crew. We used [30] and [28] as reference to design our cockpit. The details of Baruna-1 cockpit design can be seen in the following sections.

3.10.1 Cockpit Schematics

An air transport aircraft cockpit controls are typically divided into four main panels, namely:

1) **Overhead Panel**

   Located just above the pilots' head while they are sitting on their respective pilot seats. Consists of controls for a lot of the aircraft systems, such as electrical, hydraulics, fuel, environmental, bleed air, engines, anti-icing and de-icing, and other miscellaneous aircraft systems.

2) **Glareshield Panel**

   Located just in front of the pilot's view. This is where pilots can give inputs to the autopilot system, because the autopilot control panel, commonly known as Mode Control Panel (MCP), is usually placed on the glareshield. Other than that, it usually has two barometric pressure or altimeter setting control panels, master caution and master warning lights, and two Electronic Flight Instrument System (EFIS) control panels. However, for the Baruna-1 Aircraft, instead of placing the Radio Management Panels on the central pedestal, we planned to place them on the glareshield panel. This is done so that pilots can still have a view of the front cockpit window while setting radio frequencies. Other than that, the HUDs and HMDs control panels are also planned to be placed on the glareshield panel.

3) **Main Instrument Panel**

Located just below the glareshield panel. This is the panel that will be monitored the most by pilots, because it contains the main flight displays, namely, the Primary Flight Display (PFD) and Navigation Display (ND), each pilot will have each of their own main displays. The PFD shows the airspeed, altitude, attitude, vertical speed, flight mode, heading, and angle of attack of the aircraft, while the ND works like a digital map, showing a bigger heading display, the flight path, and the aircraft's position along with the surrounding waypoints, airports, navaids, terrain, and weather. In Baruna-1, as mentioned in the systems and avionics section, the main displays can also be used to display electronic charts. Moreover, the main instrument panel also houses the Aircraft Monitoring Displays (AMDs), which monitor the conditions of the aircraft systems for the pilots. Crucial aircraft components interfaces are also typically installed on the main instrument panel, such as the landing gear lever and autobreak selector.

4) **Central Pedestal Panel**

Located in the center of the cockpit and in between the pilot seats. The panel typically consists of throttle levers, flaps lever, speedbrakes lever, RMPs, weather radar display controls and the Multi-purpose Control and Display Units (MCDUs). However, as mentioned before, the RMPs of Baruna-1 are planned to be placed on the glareshield panel.

Baruna-1 will have four of the mentioned panels above. As for the primary controls, Baruna-1 will have two yoke or control columns, and two rudder pedals, one for each pilot (see Figure. 3.10).

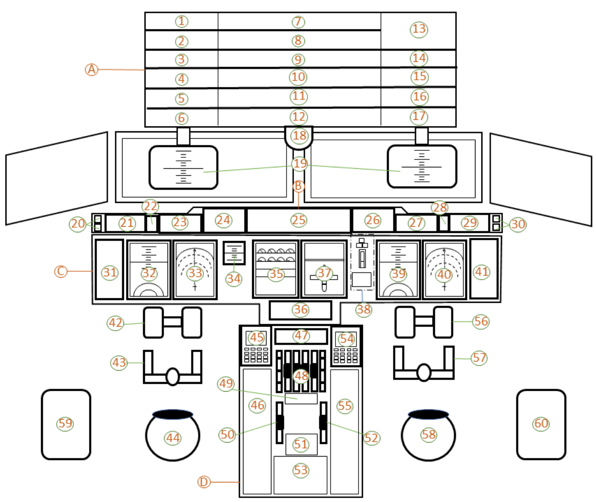

FIGURE 3.10: Baruna-1's cockpit schematic.

The letters in Figure. 3.10 indicates the aforementioned four main panels, respectively. As for the numbers they are called as listed in Table. 3.7.

No.	Component(s)	No.	Component(s)
1	IRS control panel	31	Captain's radio and speakers volume control panel, along with radio channel switching controls
2	Flight control computers control panel	32	Captain's PFD, shows the aircraft's attitude, altitude, airspeed, vertical speed, flight mode, etc. Can be used to display electronic charts, and can also be switched to show the ND if the pilot desires to

3	TAWS/GPWS system control panel	33	Captain's ND, shows the aircraft's position, course, and heading. It can also show the surrounding weather and terrain, airports, waypoints, and mission profiles. Similar to the PFD, it can be used to display electronic charts, and can also be switched to show the PFD if the pilot desires to
4	Emergency generators control panel	34	Standby flight instrument
5	FDR and CVR control panel	35	Left AMD, shows the aircraft's engine parameters, flap position, warnings, fuel weight, and fuel flow
6	Cockpit oxygen control panel, as well as the captain's windshield wiper and water repellant control panel	36	Firefighting system control panel
7	Engine and APU fire extinguisher control panel	37	Right AMD, shows the conditions of the aircraft systems: flight control, hydraulics, electrical, bleed air, fuel, landing gear, doors, and especially the firefighting system
8	Hydraulics system control panel	38	Landing gear lever and indicator, as well as autobrakes system control panel
9	Fuel system control panel	39	F/O's PFD, shows the aircraft's attitude, altitude, airspeed, vertical speed, flight mode, etc. Can be used to display electronic charts, and can also be switched to show the ND if the pilot desires to
10	Electrical system control panel	40	F/O's ND, shows the aircraft's position, course, and heading. It can also show the surrounding weather and terrain, airports, waypoints, and mission profiles. Similar to the PFD, it can be used to display electronic charts, and can also be switched to show the PFD if the pilot desires to
11	Bleed air system, de-icing, and anti-icing control panel	41	F/O's radio and speakers volume control panel, along with radio channel switching controls
12	Anti-icing and deicing control panel, along with exterior and interior lighting control panel, seat belt signs and chime switch, ground crew call switch, and APU switch	42	Captain's rudder pedals
13	Third RMP for the ACARS	43	Captain's control column
14	Flight control computers control panel	44	Captain's HMD
15	Cargo hold fire suppression system control panel and RAM air inlet door control panel	45	Captain's MCDU
16	Engine manual start control panel and propeller autofeather system switch	46	Weather radar control panel, cargo door control panel, and parking break switch
17	The F/O's windshield wiper and water repellant control panel	47	AMD display control panel and display switching controls
18	Standby compass	48	Throttle quadrant and horizontal stabilizer trim wheel
19	Captain and F/O's Head up displays (HUDs)	49	Engine ignition switches
20	Captain's master caution and master warning light	50	Speedbrake lever
21	Captain's HUD and HMD control panel	51	Rudder trim and aileron trim control panel
22	Captain's barometric pressure setting panel	52	Flap lever
23	Captain's EFIS control panel	53	Cockpit door control panel and emergency landing gear lever
24	Captain's RMP	54	F/O's MCDU
25	Autopilot control panel or MCP	55	TCAS and transponder control panel
26	F/O's RMP	56	F/O's rudder pedals
27	F/O's EFIS control panel	57	F/O's control column
28	F/O's barometric pressure setting panel	58	F/O's HMD
29	F/O's HUD and HMD control panel	59	Captain's oxygen mask
30	F/O's master caution and master warning light	60	F/O's oxygen mask

TABLE 3.7: Corresponding components for numbers shown in Figure. 3.10

3.10.2 Cockpit Visibility and Geometry

According to [30], the minimum angle of sight from the horizontal line of the pilot's eye point to the cockpit window edges are 15 degrees below, and 20 degrees above the line. On the other hand, [28] states (Han is still not done with the cockpit CAD) that the angle must at least be 18 degrees below, and 5 degrees above the horizontal line. At the end, we decided that the view angle below the pilot eye horizontal line would be 18 degrees, while the angle above it is 20 degrees. Moreover, the geometry of Baruna-1's cockpit is also made using [1] and [2] as references. Baruna-1's cockpit visibility and geometry can be seen in Figure. 3.11 with the corresponding letters' name in Table. 3.8.

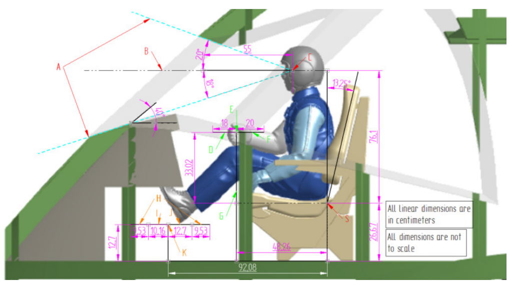

(a) Baruna-1's cockpit visibility and geometry (side view).

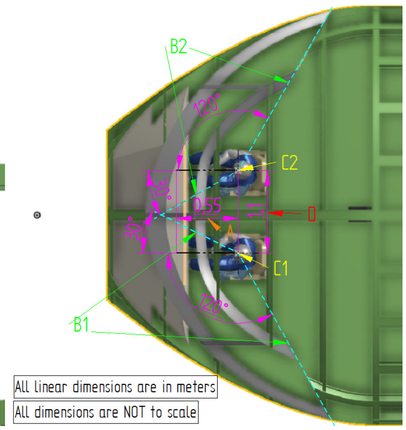

(b) Baruna-1's cockpit visibility and geometry (top view).

FIGURE 3.11: Baruna-1's cockpit visibility and geometry.

Letters	Depiction
A	Pilot's eye vectors
B	Pilot's eye point horizontal axis
C	Pilot's eye point
D	Forward yoke movement length
E	Yoke neutral position point
F	Backward yoke movement length
G	Control column line
H	Forward rudder movement length
I	Forward rudder adjustment length
J	Backward rudder adjustment length
K	Backward rudder movement length

Letters	Depiction
A	Distance between both pilots' eye point toward to windshield
B1	Captain's eye vectors
B2	F/O's eye vectors
C1	Captain's eye point
C2	F/O's eye point
D	Length between each pilot's eyepoint, or between each pilot seat's horizontal centerline

TABLE 3.8: Baruna-1's cockpit visibility and geometry letters indicator

Chapter 4

Propulsion System

From the initial sizing analysis in subsection 1.4, the power-to-weight ratio of our design point at 150,000 kg MTOW is $P/W \approx 0.31$, that is 46,500 kW power ($\sim 35,000$ hp) needed to satisfy the objective performances. In addition to that, the turboprop engine was selected in the baseline configuration (see subsection 1.5) to accommodate the required low-altitude flight during payload drop. The value of required power and the engine type are the constraints used in engine selection. A shortlisted engine candidate is tabulated in Table. 4.1.

4.1 Baruna-1 Engine and Specification

The Europrop TP400-D6 was selected for Baruna-1 Firefighting Aircraft due to its latest technology compared to other engine candidates. Since it is relatively new in the market, it would have better manufacturer support. The TP400-D6 will have a modular design that could improve the engine availability for operational support and efficiencies for all maintenance activities [46]. According to Rolls-Royce, TP400-D6 has a low-risk design and has optimized life cycle cost, and low fuel consumption that would minimize the operational and maintenance cost [47, 48].

The Europrop TP400-D6 is a three-spool axial flow turboprop engine consisting of a Propeller Reduction Gearbox, a five-stage axial-flow intermediate pressure compressor, a six-stage axial-flow high-pressure compressor, an annular combustion chamber, a single-stage axial-flow high-pressure turbine, a single-stage axial-flow intermediate pressure turbine, a three-stage axial-flow low-pressure turbine, an accessory gearbox, and a Full Authority Digital Engine Control (FADEC) [41]. The schematic of this engine is shown in Fig. 4.1

The Europorop TP400-D6 has a maximum uninstalled power of 11,065 shp with fuel consumption of 0.228 kg/kW h at take-off condition. The engine weighs around 1,960 kg including the complete engine accessory equipment, without fluid and instrumentation. The overall length is 4.18 m (from the front of PGB to the rear of the primary nozzle) with a maximum diameter (radius) of 1.218 m (radius from centerline measured at the lowest point). The TP400-D6 comes with two different kinds, the baseline engine (propeller clockwise) and the handed engine (propeller counter-clockwise) [41]. This engine specification is summarized in Tabel 4.2. With approximately 35,000 hp needed for Baruna-1, four Europrop TP400-D6 engine is installed at the wing.

NO	Engine Name	Power (hp)	Dimension Length (m)	Diameter (m)	Mass (kg)	SFC	Images
1	Europrop TP400-D6 [41]	11,065	3.5	1.218	1960	0.228	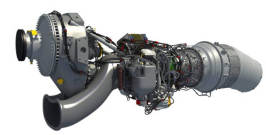
2	Kuznetsov NK-12 [42] [43]	10,880	6	1.15	3170	0.219	
3	Pratt and Whitney T34 [44]	7,500	4	0.85	1163	0.257	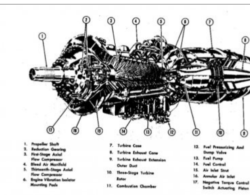
4	Progress D-27 [45]	13,240	4.195	1.259	1650	0.243	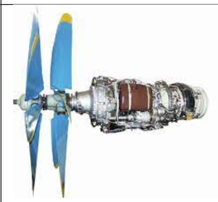

TABLE 4.1: Engine Candidate Specifications.

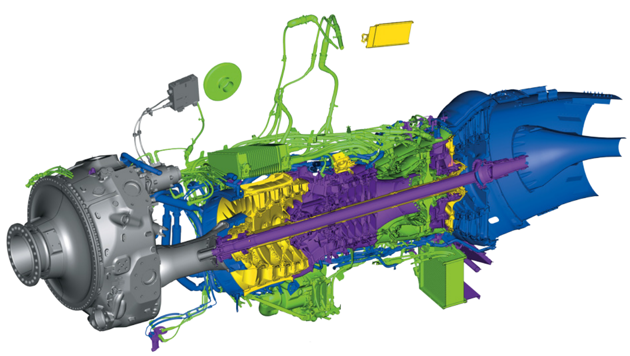

FIGURE 4.1: Cutaway drawing of TP400-D6, cr: europrop international [49]

Performance		
Maximum Power	11,065	shp
SFC (TO)	0.228	kg/kW h
SFC (Cruise)[50]	0.167	kg/kW h
Weight and Dimension		
Weight	1,960	kg
Length	3.5	m
Overall Length	4.18	m
Diameter	1.218	m.
Engine Information		
Overall Pressure Ratio	25	-
Control System	FADEC	-
EIS	2003	

TABLE 4.2: Europrop TP400-D6 Specification [41]

4.2 Propeller

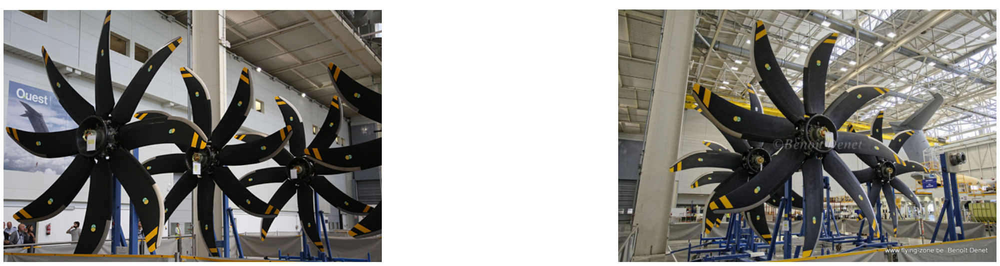

FIGURE 4.2: Propellers of interest (FH385 (Left) and FH386 (Right) Propellers

Dimension and Weight		
Diameter	5.334	m
Weight	683	kg
Operating Limits		
Maximum Takeoff:		
Power	11,065	shp
Speed	860	rpm
Torque	91,618	N.m
Maximum Continuous:		
Power	7,971	kW
Speed	842	rpm
Torque	90,407	N.m
Propeller Pitch Angle	-21.7 ° up to +83 ° at 75% blade radius	

TABLE 4.3: FH385 and FH386 Specification [51]

As for the propellers, the selection bounds to the Ratier Figeac FH385 as well as the FH386 for contra-rotating type. Both Figeac FH385 and FH386 are eight-bladed variable pitch tractor propellers with feathering reversing capability. The hub for both propeller are made out of steel, and the eight blades have a steel shank bonded to a graphite spar and an aramid fiber envelope. The leading edge of this propeller blade is protected by an electrical de-icer boot and a nickel sheath. The propeller hydro-mechanical blade pitch actuator is controlled by a propeller control module which is connected to the engine FADEC (Full Authority Digital Engine Control) [51]. Both propellers have a diameter of 5.334 m wide and weighting around 683 kg. At maximum power of 8,251 kW (11,065 shp), the maximum rotational speed of this propeller is 860 rpm and could handle up to 91,618 N.m of torque [51].

Chapter 5

Landing Gear

As mentioned before in the Chapter 2, the dual wheels landing gear concept will serve as the nose landing gear and the triple bogie landing gear concept will serve as the main landing gear. The total number of wheels will be 14 (two for the nose and six for each side of the main landing gear). In designing the landing gear, we have thought of several steps needed in the iteration of coming up with the optimum design of it,

1) Step 1: Find references or inspirations related to the wanted design, First we defined that we have to find references or inspirations from previous designs and researches of the same interest of our needs.

2) Step 2: Try to imitate and modify existing inspirations, Next, we started to design the starting ground of the landing gear by imitating the given resources.

3) Step 3: Finalization of the design, Lastly, re-checking and re-testing the design to logically work in a real-world environment.

5.1 Design Factor and Consideration

Below are the design factors and some considerations that we have been through before finalizing the designs, especially the landing gear designs.

5.1.1 Airport Accessibility

While we can roughly predict when is the highest probability of wildfires to occur, it will not give an exact time of when it will happen. Hence, the aircraft must have the ability to use any aerodrome with an appropriate runway length and conditions.

5.1.2 Ease of Ground Handling

As mentioned previously, not every aerodrome can support all types of aircraft. Baruna-1 needs to efficiently operate with the bare minimum ground equipment.

5.1.3 Carrying Large Amount of Payload

Due to the heavy payload that Baruna-1 will be carrying, a VLAT class water bomber, the landing gear must sustain the load subjected to its strut, wheel, and suspension.

5.2 Landing Gear Configuration

5.2.1 Tricycle Nose Gear Setup

For the layout of the landing gear, a nose gear layout is superior than other layout. This due to the ease of handling of the aircraft because of the visibility of the surrounding area for the pilot given by the layout [52]. Also, since Baruna-1's cargo bay door is on the aft side, the nose gear is a must configuration in this regard. Also, since the aircraft has an aft side, the center of gravity or CG must be reconsidered to be able to maintain the control and stability of the aircraft.

5.2.2 Multi-Bogey Landing Gear

The heavier the aircraft, the number of landing gear increases. Multiple wheels attached to a common strut are called multi-bogey landing gear systems. The multi-bogey landing gear configuration offers a more excellent safety and reliability due to its multiple wheels that can be backed up if some of landing gear fails. Other than just providing security and reliability for the aircraft, multi-bogey has very stable control on the ground or during taxiing [28].

5.2.3 Retractable Landing Gear

Landing gear can be as simple as attaching a steel bar and suspension to the fuselage or as complex as mechanical assembly that is able move to store itself in a landing gear bay.

5.2.4 Fuselage Podded Landing Gear Bay

Baruna-1 put all of its fire fighting system components in its lowest compartment. The lower part of the fuselage portion is taken by valve assembly and actuator, which is why the fuselage podded landing gear bay (a pod body on each side of the aircraft) is the best option to store the landing gear and its system, so that it would not interfere with other system.

5.2.5 Oleo-Pneumatic Shock Absorbers

Modern and heavy aircraft commonly use an oleo-pneumatic shock absorber type. Oleo-pneumatic uses a gas and oil system, where the gas acts like a spring and the oil acted as a damper [28].

5.3 Technical Parameters and 3D Design

Fuselage to Ground Height	1,200 mm
Main gear strut position with respect to LE	1,860 mm
Nose gear position with respect to LE	7,892 mm
Clearance Angle	14.62°
Tip back Angle Requirements	36.13°
Wheel Base	7,990 mm
Wheel Track	4,500 mm

TABLE 5.1: Landing gears placement and clearance

	Main Gear	Nose Gear
Total Mass	2,244 kg	628 kg
Tire Sizing	$43\text{x}15.5^{-17}$	$37.\times\ 14.0^{-14}$
Tire Models	Dunlop DR32622T	Dunlop DR20523T [53]
Tire Loaded Rated Inflation	148 psi	154 psi

TABLE 5.2: Landing gears physical parameters

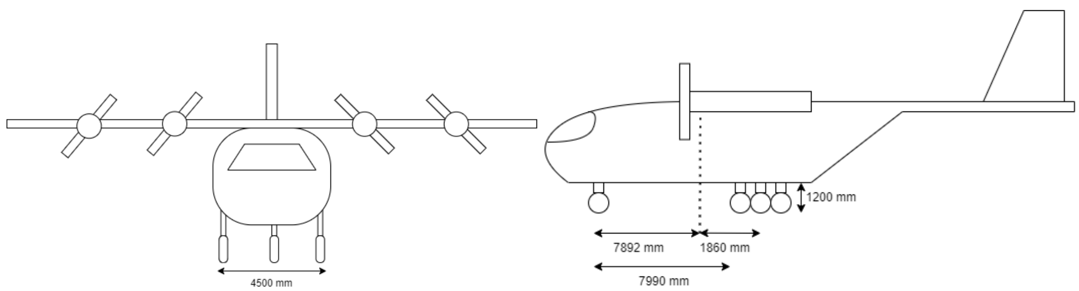

(a) front view (b) side view

FIGURE 5.1: Landing gear position (front view and side view)

(a) Main landing gear design concept (b) Nose landing gear design concept

FIGURE 5.2: Nose landing gear and main landing gear concepts (ISO view)

Chapter 6

Auxiliary Systems

6.1 Avionics

6.1.1 Integrated Modular Avionics (IMA)

For the Baruna-1, we proposed to implement the Integrated Modular Avionics (IMA) concept into our avionics architecture.

6.1.2 Baruna-1's Avionics Subsystems

Baruna-1's avionics system is based on FAR 25 Subpart F's requirements [54]. However, additional military equipment is considered to ease firefighting operations. The Baruna-1 will have 4 of the main avionics subsystems listed in Figure. **??** with the addition of a firefighting subsystem, firefighting system displays and panel, Head-Up Displays (HUDs), and Helmet Mounted Displays (HMDs) added to the avionics system. Thus the simplified avionics system diagram for Baruna-1 would be drawn as shown in Figure. 6.1.

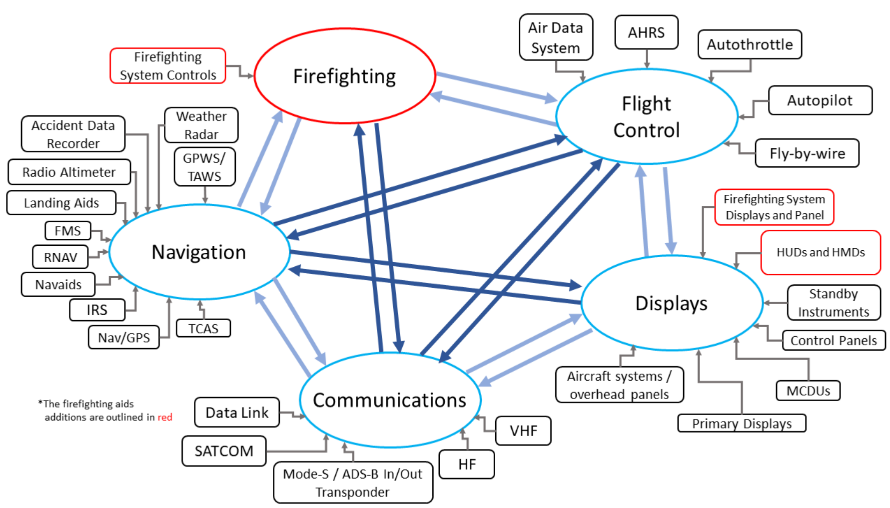

FIGURE 6.1: Baruna-1's avionics subsystems (addition of firefighting subsystem, firefighting system displays and panel, HUDs, and HMDs).

We use off-the-shelf avionics to keep costs low and reduce production time. Our plan is to have two aircraft types with different avionics systems: a semi-military and military avionics system. The Baruna-1 aircraft type with a semi-military avionics architecture is planned to have a military-grade Flight Management System (FMS), HUDs, and HMDs, which can help with airdropping operations, while the rest of the avionics systems use commercial-grade avionics. This is done so that the aircraft can be reliable in firefighting operations while keeping the production and maintenance costs relatively low. To summarize, the comparison of the semi-military and military avionics system for Baruna-1 is listed in Table. 6.1.

Capabilities	Baruna-1 with:	
	Semi-Military Avionics System	Military Avionics System
Firefighting	YES	YES
Military FMS (allows airdropping and low altitude flight management)	YES	YES
HF and VHF communication and navigation	YES	YES
SATCOM	YES	YES
UHF communication and navigation	NO	YES
TACAN	NO	YES

TABLE 6.1: Comparison between Baruna-1's semi-military and military avionics system.

Our main focus here would be on the semi-military avionics system, because it can give the most performance to our aircraft while keeping the cost relatively low. The military avionics system is just a consideration. What is written in sections 6.1.2 until 6.1.2 are the details regarding the avionics subsystems for Baruna-1's semi-military avionics system.

Flight Control Subsystem

Baruna-1 utilizes a fly-by-wire (FBW) flight control system. To briefly explain the mechanism of fly-by-wire here is a general idea on the process.

Besides that, Baruna-1 has an autopilot and autothrottle system, Attitude and Heading Reference System (AHRS), and Air Data System (ADS). The autopilot and autothrottle system is used to reduce the pilots' workload.

System	Product Name	Manufacturer	Mass	Dimensions
Fly-By-Wire System	Thales Flight Control Computer (FCC)	Thales	N/A	N/A
	Remote Electronic Units	Thales	N/A	N/A
ADS	SmartProbe Air Data System	Rockwell Collins	N/A	N/A
AHRS	AHS-3000S	Rockwell Collins	AHC-3000S Aittitude Heading Computer: 2.09 kg (4.61 lbs.)	AHC-3000S Attitude Heading Computer: (33.83 x 6.35 x 12.7) cm or (13.32 x 2.5 x 5) in.
			ECU-3000 External Compensation Unit: 0.09 kg (0.2 lbs.)	ECU-3000 External Compensation Unit: (7.16 x 5.08 x 3.63) cm or (2.82 x 2.00 x 1.43) in.
			MMT-3010 Multi Modular Mount: 0.40 kg (0.9 lbs.)	MMT-3010 Multi Modular Unit: (38.35 x 6.98 x 5.08) cm or (15.10 x 2.75 x 2.0) in.
			323A-2G Flux Detector Unit: 0.68 kg (1.5 lbs.)	323A-2G Flux Detector Unit: (12.144 x 12.144 x 6.825) cm or (4.781 x 4.781 x 2.687) in.

Autopilot and Autothrottle	APS-85 Autopilot System	Rockwell Collins	N/A	N/A

TABLE 6.2: Baruna-1's flight control subsystem avionics list.

The avionics in table X.2 are all off-the-shelf avionics. We chose Thales' FBW system [55] because of their experience in the FBW field, especially in their Airbus projects [55]. The ADS would be covered by Rockwell Collins' SmartProbe Air Data System [56], [57], providing integrated architecture of the ADS [56], [57]. The SmartProbe ADS provides all the necessary air data components for a transport aircraft, which includes: pitot tubes, pitot-static tubes, angle of attack (AOA) sensors, stall protection system, total air temperature (TAT) sensors, and outside air temperature (OAT) sensors [56], [57]. Lastly, the AHRS, and the autopilot and autothrottle system shall be taken care of by Collins' AHS-3000S [57]–[58] and APS-85 [59] respectively. Note that we will make our own autopilot panel layout. The APS-85 will only be used as an autopilot and autothrottle software for our aircraft. All the avionics and components in the flight control system are interconnected via electrical wires.

The schematic of Baruna1's flight control system is shown in Figure. 6.2

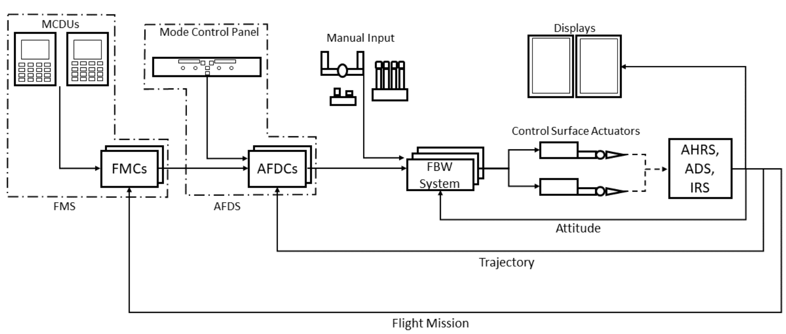

FIGURE 6.2: Baruna-1's flight control subsystem schematic, using [60], [61] as a reference.

The schematic in figure c.cc can be divided into three loops, the inner (Attitude), middle (Trajectory), and outer loop (Flight Mission) [60], [61]. Each loop describes how Baruna-1's flight control system works.

1. **Inner Loop**, is the manual manipulation of the primary flight control using the control column will be tracked by the FBW system via electrical wires.
2. **Middle Loop**, now the AFDS (regarded as the autopilot and autothrottle system) is involved. The AFDS consists of the Mode Control Panel (MCP), and the Autopilot and Flight Director Computers (AFDCs).
3. **Outer Loop**, includes the FMS in the cycle. The FMS consists of the Multipurpose Control and Display Units (MCDUs) and the Flight Management Computers (FMCs).

Navigation Subsystem

Baruna-1's navigation subsystem is divided into several systems, namely as the followings:

1) Inertial Reference System (IRS),

2) Global Positioning System (GPS),

3) Flight Management System (FMS),

4) Traffic Collision and Avoidance System (TCAS),

5) Ground Proximity Warning System/Terrain Awareness Warning System (GPWS/TAWS),

6) Radio Altimeter,

7) Flight Data Recorder (FDR) and Cockpit Voice Recorder (CVR),

8) Emergency Locator Transmitter (ELT),

9) Instrument Landing System (ILS),

10) VHF Omni-directional Range (VOR),

11) Distance Measuring Equipment (DME),

12) Automatic Direction Finder (ADF),

13) Weather Radar.

Baruna-1's navigation system follows the standard equipment requirements required for a typical transport aircraft. It allows the aircraft to conduct Visual Flight Rules (VFR) and Instrument Flight Rules (IFR) operations. The aircraft would also be able to navigate with ground-based navigation equipment and GPS. It would also be capable of doing a precision approach (ILS approach CAT I, CAT II, and CAT III autoland) and a non-precision approach (VOR, NDB, RNAV, and RNP approach). Moreover, Baruna-1 is designed to be able to navigate around weather and terrain using the weather radar and GPWS/TAWS respectively. When an incident or accident happens to the aircraft, the FDR and CVR installed on the aircraft can help its investigation. Most importantly, we planned to use military FMS for Baruna-1. With it, Baruna-1 would be able to conduct airdropping and low altitude operations simply by typing in commands to the FMS, reducing pilot workload significantly. Airdropping, in this case, meant dropping firefighting retardant into burning areas. The list of avionics that would be used in the Baruna-1's navigation systems are shown in Table. 6.3.

System	Product Name	Manufacturer	Mass	Dimensions
IRS	ADIRS (Air Data and Inertial Reference System)	Honeywell	7 kg (15.43 lbs.)	4 MCU: (32.41 x 12.40 x 19.41) cm or (12.76 x 4,88 x 7.64) in.
FMS	FMC-4500	Rockwell Collins	8 kg (17 lbs.)	1/2 ATR short enclosure, 31.8 (L) x 12.38 (W) x 19.3 (H) cm (12.5 (L) x 4.9 (W) x 7.6 (H) in.)
	CDU-7000	Rockwell Collins	4.94 kg (10.9 lbs)	Without connector: (20.32 x 14.61 x 18.10) cm or (8.0 x 5.75 x 7.125) in. With connector: (23.78 x 14.61 x 18.10) cm or (9.32 x 5.75 x 7.125) in.
GPS	GPS-4000S	Rockwell Collins	2.9 kg (6.3 lbs.)	2 MCU: (36.88 x 6.17 x 20.00) cm or (14.52 x 2.43 x 7.87) in.

TCAS	TTR-4100 TCAS	Rockwell Collins	6.2 kg (13.7 lbs.)	4 MCU: (38.76 x 12.85 x 19.41) cm or (15.26 x 5.06 x 7.64) in.
GPWS/ TAWS	EGPWS (Enhanced Ground Proximity System) MK VIII	Honeywell	1.77 kg (3.9 lbs)	(26.16 x 7.72 x 17.75) cm or (10.30 x 3.04 x 6.20) in.
Radio Altimeter	ALT-4000	Rockwell Collins	2.3 kg (4.7 lbs.)	(35.37 x 9.05 x 8.42) cm or (13.93 x 3.56 x 3.31) in.
FDR & CVR	FA5000 Cockpit Voice and Data Recorder (CVDR)	L3Harris	3.7 kg (8.16 lbs.)	(25.20 x 14.94 x 16.71) cm or (9.92 x 5.88 x 6.58) in.
ELT	Artex ELT 5000 Distress Tracking (DT) For GADSS Compliance	ACR Electronics	2.54 kg (5.60 lbs.)	(22.80 x 16.60 x 8.71) cm or (8.98 x 6.54 x 3.43) in.
ILS Receiver	NAV-4000	Rockwell Collins	1.54 kg (3.4 lbs.)	2.5 MCU: (35.56 x 5.84 x 8.38) cm or (14 x 2.3 x 3.3) in.
VOR Transceiver				
ADF Transceiver				
DME Transceiver	DME-4000	Rockwell Collins	1.54 kg (3.40 lbs.)	(35.87 x 6.35 x 8.64) cm or (14.12 x 2.5 x 3.4) in.

TABLE 6.3: Baruna-1's navigation subsystem avionics list.

Firstly, we plan to use Honeywell's ADIRS (Air Data and Inertial Reference System) [62], [63] for Baruna-1's IRS, since it has been used on a number of FBW aircraft [62], [63]. For the FMS, Rockwell Collins' FMC-4500 [64], [65] and CDU-7000 [66], [67] will be used. Both of those avionics can be used for civil and military operations [64]–[67]. The GPS and TCAS are provided by Rockwell Collins' GPS-4000S [68], [69] and TTR-4100 [70], [71] respectively. Honeywell's EGPWS MK VIII [72], [73] covers the GPWS/TAWS of Baruna-1. Aside from showing terrain displays and giving aural terrain warnings, it allows Enhanced Ground Proximity Warning System (EGPWS) [72], [73] to be used on Baruna-1. Moreover, Rockwell Collins' ALT-4000 [74], [75] will be used for the aircraft's radio altimeter. The FDR and CVR of Baruna-1 will be provided by L3Harris' FA5000 Cockpit Voice and Data Recorders (CVDRs) [76], which can either function as a CVR or FDR [76]. The ELT 5000 [77] from L3Harris will take care of Baruna-1's ELT system. The Rockwell Collins' NAV-4000 [78], [79] will act as an ILS receiver, VOR Transceiver, and ADF Transceiver in one unit [78], [79]. Finally, the DME transceiver of our aircraft would be provided by Rockwell Collins' DME-4000 [80], [81]. Baruna-1's navigation subsystem schematic is shown in Figure. 6.3.

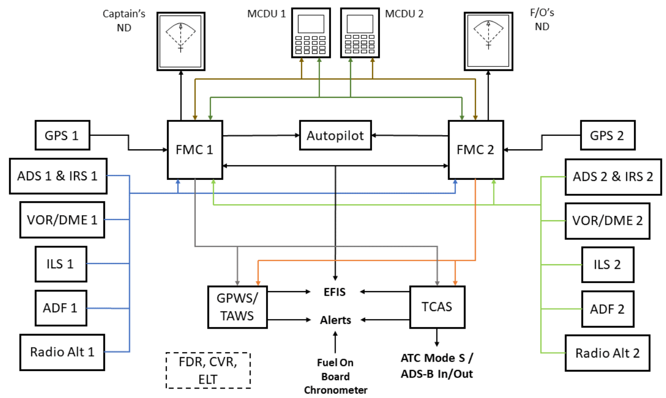

FIGURE 6.3: Baruna-1's navigation subsystem schematic, using [60], [61] as reference.

From Figure. 6.3, we can see that there are two separate avionics systems performing the same duties and feeding each other information for every system. This is done for safety reasons — redundancy.

Communications Subsystem

Baruna-1 will have a Very High Frequency (VHF) and High Frequency (HF) communications system, and Satellite Communications (SATCOM) for its communications subsystem. It will also have an ACARS (Aircraft Communications Addressing and Reporting System) or data link system to allow seamless integration with other avionics within the communications subsystem and other subsystems.

System	Product Name	Manufacturer	Mass	Dimensions
ACARS Management System	CMU Mark II+	Honeywell	5.44 kg (12 lbs.)	4 MCU: (32.41 x 12.40 x 19.41) cm or (12.76 x 4.88 x 7.64) in.
VHF	VHF-4000	Rockwell Collins	1.59 kg (3.50 lbs)	(35.87 x 6.35 x 8.74) cm or (14.12 x 2.50 x 3.44) in.
			Receiver/Exciter: 2.50 kg (5.50 lbs.)	Receiver/Exciter: (27.43 x 7.87 x 12.70) cm or (10.8 x 3.1 x 5.0) in.
			Receiver/Exciter Install Kit (Rack only): 0.14 kg (0.30 lbs.)	Receiver/Exciter Install Kit (Rack only): (27.94 x 8.38 x 0.64) cm or (11.0 x 3.3 x 0.25) in.
			Power Amplifier: 3.45 kg (7.60 lbs.)	Power Amplifier: (32.26 x 18.29 x 4.57) cm or (12.7 x 7.2 x 1.8) in.
			Power Amplifier Install Kit (Rack only): 0.32 kg (0.70 lbs.)	Power Amplifier Install Kit (Rack only): (32.51 x 18.54 x 0.64) cm or (12.8 x 7.3 x 0.25) in.
			Antenna Coupler: 7.12 kg (15.71 lbs.)	Antenna Coupler: (34.29 x 11.94 x 18.29) cm or (13.5 x 4.7 x 7.2) in
			Antenna Coupler Vertical Install Kit (Rack only): 0.23 kg (0.50 lbs.)	Antenna Coupler Vertical Install Kit (Weight for Rack only): (34.54 x 11.94 x 0.64) cm or (13.6 x 4.7 x 0.25) in.

HF	Honeywell Primus HF 1050 HF Radio System	Honeywell	Antenna Coupler Horizontal Install Kit (Rack only): 0.32 kg (0.70 lbs.)	Antenna Coupler Horizontal Install Kit (Weight for Rack only): (34.54 x 18.29 x 0.64) cm or (13.6 x 7.2 x 0.25) in.
			Antenna Coupler Dual Vertical Install Kit (Rack only): 0.50 kg (1.10 lbs.)	Antenna Coupler Dual Vertical Install Kit (Weight for Rack only): (34.54 x 25.40 x 0.64) cm or (13.6 x 10 x 0.25) in.
			Primus II Select HF Control Head, Amber/Gray: 0.50 kg (1.10 lbs.)	Primus II Select HF Control Head, Amber/Gray: (13.65 x 6.03 x 6.67) cm or (5.375 x 2.375 x 2.625) in.
			TOTAL: 15.08 kg (33.21 lbs.)	
SATCOM	IRT NX SATCOM System	Rockwell Collins	- IRT-4000 Satellite Data Unit: 3.49 kg (7.7 lbs.)	- IRT-4000 Satellite Data Unit : (38.750 x 6.172 x 20.008) cm or (15.256 x 2.430 x 7.877) in.
			- ICM-4000 Satellite Configuration Module: 0.23 kg (0.5 lbs.)	- ICM-4000 Satellite Configuration Module: (10.198 x 11.468 x 2.578 cm or (4.015 x 4.515 x 1.015) in.
			- LGA-4000 Low-Gain Antenna: 1.00 kg (2.2 lbs.)	- LGA-4000 Low-Gain Antenna: (21.18 x 13.97 x 8.51) cm or (10.7 x 5.5 x 3.35) in.
			- HGA-4000 High-Gain Antenna: 1.81 kg (4 lbs.)	- HGA-4000 High-Gain Antenna: (33.02 x 13.97 x 7.62) cm or (13.0 x 5.5 x 3.0) in.
ADS-B In/Out / MODE-S Transponders	TPR-901-205/225 Transponders	Rockwell Collins	6.3 kg (13.8 lbs.)	4 MCU: 32.5 x 12.5 x 19.3) cm or (12.8 x 4.9 x 7.6) in.
ELT	Artex ELT 5000 Distress Tracking (DT) For GADSS Compliance	ACR Electronics	2.54 kg (5.60 lbs.)	22.80 x 16.60 x 8.71) cm or (8.98 x 6.54 x 3.43) in.
ILS Receiver VOR Transceiver ADF Transceiver	NAV-4000	Rockwell Collins	1.54 kg (3.4 lbs.)	2.5 MCU: 35.56 x 5.84 x 8.38) cm or (14 x 2.3 x 3.3) in.
DME Transceiver	DME-4000	Rockwell Collins	1.54 kg (3.40 lbs.)	35.87 x 6.35 x 8.64) cm or (14.12 x 2.5 x 3.4) in.

TABLE 6.4: Baruna-1's Communication subsystem avionics list.

First of all, we choose Honeywell's CMU Mark II+ [82], [83] ACARS management unit or Communications Management Unit (CMU) to handle the ACARS system of our aircraft. The VHF transceiver would be taken care of by Rockwell Collins' VHF-4000 [84], [85]. The schematic of Baruna-1's communications subsystem can be seen in figure X.5. On the other hand, Baruna' 1's HF communications system will be provided by Honeywell's Primus HF-1050 HF Radio System [86], [87]. The SATCOM system will be provided by Rockwell Collins' IRT NX SATCOM System [88], [89]. The SATCOM system will include the IRT-4000 Satellite Data unit, ICM-4000 Satellite Configuration Module, LGA-4000 Low-Gain Antenna, and HGA-4000 High-Gain Antenna [88], [89]. Finally, the ADS-B in/out and Mode-S capable transponders for Baruna-1 would be provided by Rockwell Collins' TPR-901-205/225 Transponders [90]–[91].

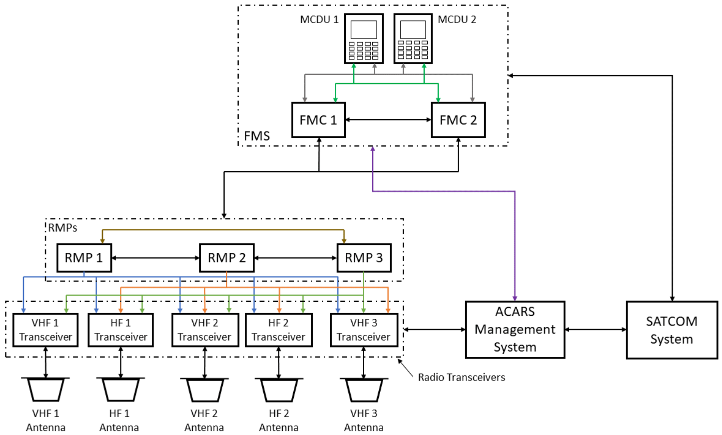

FIGURE 6.4: Baruna-1's communications subsystem schematic, using [60] as reference.

As shown in Figure. 6.4, the avionics are laid out as such that each system can back each other up if one or several systems fail, just like the other avionics subsystems. The pilots can interact with the communications system through the Radio Management Panels (RMPs) or the MCDUs.

Displays Subsystem

Following the advancements in cockpit displays, Baruna-1 will have glass-cockpit displays, where the primary displays use Liquid Crystal Display (LCD) screens. Moreover, most of the flight instruments are digital. To help the pilots with firefighting operations, We will implement Head-up-Displays (HUDs) and Helmet-Mounted Displays (HMDs) with vision enhancement technologies. Table. 6.5 shows the list of avionics that Baruna-1 will be using for its displays subsystem.

System	Product Name	Manufacturer	Mass	Dimensions
Vision Enhancement	HGS-6000 with EVS-3600	Rockwell Collins	N/A	N/A
	HMD TopOwl Digital Display	Thales Group	N/A	N/A
Primary and Monitoring Displays	AFD-3010E	Rockwell Collins	5.85 kg (12.9 lbs.)	(21.46 x 20.83 x 25.25) cm or (8.45 x 8.20 x 9.94) in.
Standby Instrument System	GH-3900	L3Harris	1.36 kg (3.0 lbs.)	Chassis Dimensions: (21.2 x 8.1 x 8.1) cm or (8.33 x 3.19 x 3.19) in.
				Overall Dimensions: (24.5 x 8.3 x 8.3) cm or (9.62 x 3.28 x 3.28) in.

TABLE 6.5: Baruna-1's displays subsystem avionics list.

Collins' Head-up Guidance System (HGS), HGS-6000 [92], along with their Enhanced Vision System (EVS-3600) [66], allow the pilots to see through fog, smog, clouds, and especially smoke [66]. They are integrated into a HUD system. In firefighting operations, they help detect fire in low visibility conditions. They also allow for nighttime firefighting operations because of their night vision capability [66]. In addition, The Thales HMD TopOwl Digital Display [93], [94] can further help with spotting burning areas.

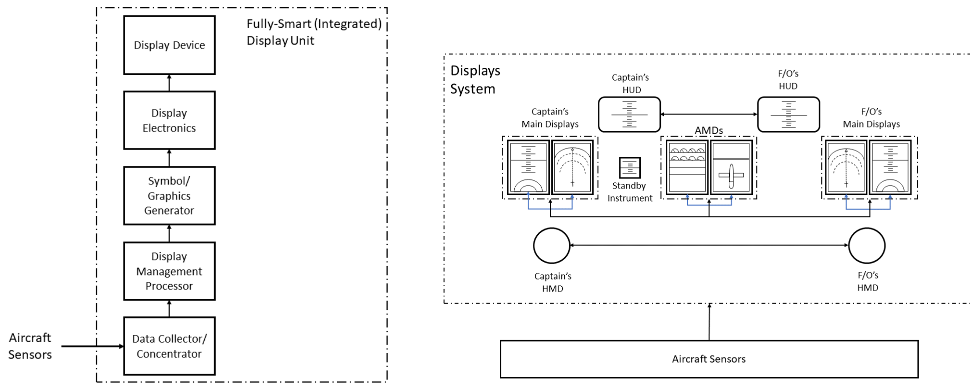

(a) Fully smart (integrated) display unit architecture using **6** as reference.

(b) Baruna-1's displays subsystem schematics using **6** as reference.

FIGURE 6.5: Overview of Baruna-1's complete displays subsystem schematics using [60] as reference.

It is a helmet-mounted display or HMD with a vision enhancement system [93], [94]. The enhancements include night vision and FLIR (Forward Looking Infrared) vision, which further eases firefighting operations [94]. Unlike the HUD, Because the HMD is attached to the pilot's head, the pilot can orient the helmet's display to their liking, which increases the chance of spotting fires.

Aside from the vision enhancement system, Baruna-1 will also have head-down displays. The head-down displays include the two Primary Flight Displays (PFDs), two Navigation Displays (ND), and two Aircraft Monitoring Displays (AMDs). The AFD-3010E [95], [96] displays from Rockwell Collins are chosen for this aircraft, because they have a fully smart (integrated) display architecture [60]. In other words, they are integrated display units. The schematic of a fully smart display unit is shown in Figure. 6.5(a) with reference to [60]. Besides that, the displays are able to display electronic charts and enhanced navigation maps [95], [96], reducing the pilot's workload. Lastly, a standby instrument system will be installed on the aircraft for safety reasons. We chose L3Harris' GH-3900 [97], [98] for this system, because it has integrated all the basic flight displays into one screen, reducing the amount of avionics needed for the standby instrument system alone [97], [98]. The schematic of Baruna-1's Displays subsystem is shown in Figure. 6.5(b).

As shown in Figure. 6.5(a), a display unit consists of a data collector/concentrator, display management processor, symbol/graphics generator, display electronics, and display device [60]. In a fully smart display unit, all the five components are integrated into one unit, reducing space and weight [60]. In Baruna-1, six of these displays will be installed. As seen from figure X.7, Four of them would be used for the main displays, the other two for AMDs.

From Figure. 6.5(b), the aircraft will have two of each display unit. The captain and first officer will each have their own displays. Both of their displays also have to be the exact copy of each other to ensure similarities for both seats.

Baruna-1's main displays are used as the PFD and ND. Other than that, they can show electronic flight charts and advanced map displays. On the other hand, the AMDs are used to monitor all the aircraft systems.

Firefighting Subsystem

To manage the procedure of the retardant delivery of Baruna-1, the aircraft firefighting system is equipped with Advance Retardant Control Circuit, abbreviated as ARCC. ARCC contains the controller unit, the so-called Fire Fighting System Control Unit, abbreviated as FFSCU, and Fire Fighting System Interface and Display Unit, abbreviated as FFSIDU, as a control display interface module.

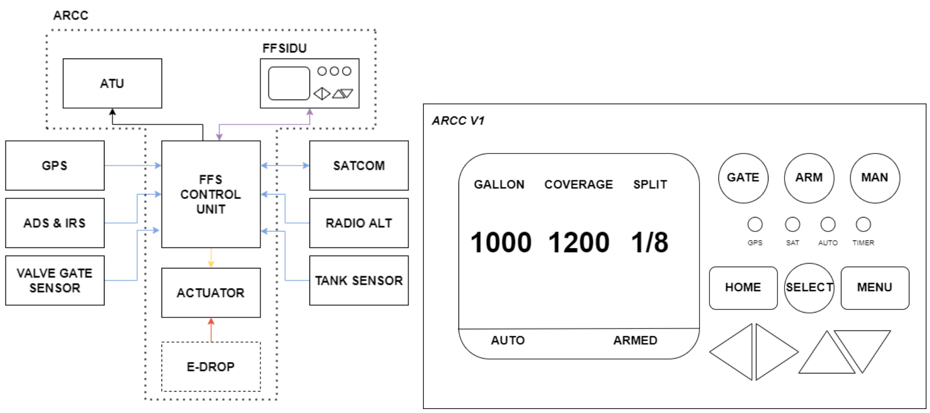

(a) ARCC system general system layout using [60] as reference

(b) FFSIDU module

FIGURE 6.6: General layout of the AARC system and an overview of FFSIDU module

FFSCU is responsible for all systems related to fire fighting operations. Such as controlling the actuator movement based on pilot input and various sensors in the fire fighting system and the aircraft onboard avionics system. FFSCU also manages the data transfer of the fire fighting system using an Additional Telemetry Unit or ATU [99].

FFSIDU is an interface module. The crew can input the parameters of the fire fighting operation, such as how much liquid volume to drop or how vast is the ground coverage. FFSIDU contains a display unit with various buttons to navigate all the options and tweak the parameters.

Other Avionics System

It is also worth mentioning that Baruna-1 will have an ice detector system. Baruna-1 will use Rockwell Collins' 0871 ND Series Ice Detectors [100], [101]. Its details are shown in Table. 6.6.

System	Product Name	Manufacturer	Mass	Dimensions
Ice-Detectors	Ice Detector Model 0871ND	Rockwell Collins	0.45 kg (1 lb.)	Max Height: 19.8 cm, Max Diameter: 8.4 cm

TABLE 6.6: Rockwell Collins' 0871 ND Series Ice Detector details.

Chapter 7

Fire Fighting System

7.1 Aerial Fire Fighting System

Baruna-1 Firefighting system is intended as a solution to every aspect of aerial fire fighting. It allows operators to precisely control and manage the retardant delivery operation from a fully automatic dropping mode to a fully manual delivery, while also providing a backup system in the case of an emergency. Not only does it provide the control of retardant delivery, but it also relays the information regarding all aspects of the fire fighting system for the ground personnel to analyze.

Baruna-1 fire fighting system implemented the semi-modular approach to the Fire Fighting System (FFS). The semi-modular approach has the benefit of ease of maintenance. Therefore a reduction in maintenance cost compels us to develop the Baruna-1 FFS as modular as possible.

7.1.1 Fire Fighting Control System

As its name might suggest, the fire fighting control system serves to manage the procedure of the retardant delivery of Baruna-1. The aircraft fire fighting system is equipped with Advance Retardant Control Circuit (ARCC) for which the design was referred to [102]. The ARCC Fire Fighting system is built in reference from FFRDS GEN III by Trotter Control [103]. The components of the ARCC system can be seen in Figure. 7.1 as well as in the following list,

1. Fire Fighting System Control Unit (FFSCU)
2. Fire Fighting System Interface and Display Unit (FFSIDU)
3. Actuator Assembly
4. Emergency Drop (E-DROP)
5. Additional Telemetry Unit (ATU)
6. By Using Air Tanker Information System (ATIS) [99] to relay the information to the operator of Baruna-1. The relayed information describes the parameter of the aircraft, such as position. And we are also providing all the data on the fire fighting system.

Fire Fighting System Control Unit (FFSCU)

As the central processing of the fire fighting system, FFSCU is responsible for all manner of control in the fire fighting system. To work appropriately, FFSCU needs all the necessary data regarding the operation of the fire fighting system. Such data are retrieved from fire fighting system sensors and aircraft flying parameters. Fire fighting sensor data are provided by the valve, gate, and tank sensors, while

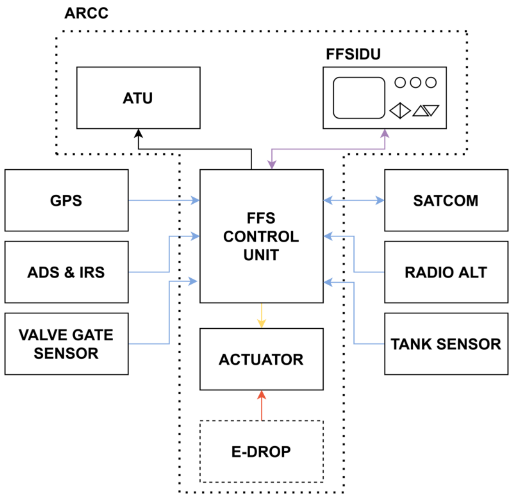

FIGURE 7.1: ARCC FFS system general layout.

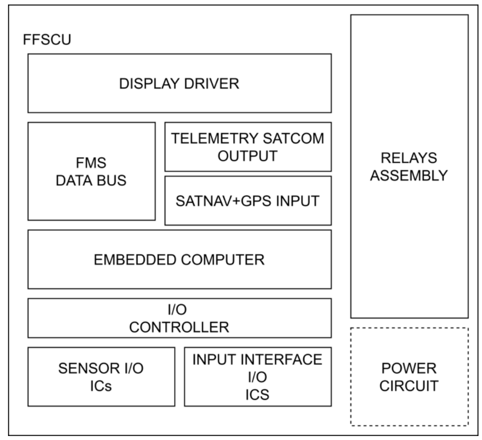

FIGURE 7.2: FFSCU system architecture.

aircraft parameters are received from the flight management system. The general architecture of FFSCU is composed of modules as seen in Figure. 7.2 as well as inside of Table. 7.1.

Module	**Description**
Embedded Computer	Main central processing unit. A System on a Chip design contains a processor, RAM, and flash memory, which run on embedded OS.
I/O controller	Managing input-output data from sensor and input interface
Sensor I/O	Data port and controller for firefighting system sensor
Input interface I/O	Data port and controller for firefighting interface unit
Power circuit	Providing and regulating power for the FFSCU
Relays assembly	Relays for controlling the actuator
FMS data bus	Integrated circuit for controlling the data between FFSCU SoC and Flight Management System data bus
Telemetry SATCOM output	Telemetry output for ATIS ATU and a connection to the satellite communication module.
SATNAV+GPS INPUT	Satellite Navigation data using GPS
Display driver	Display driver and controller for FFSIDU

TABLE 7.1: List of modules that comprises the FFSCU.

Fire Fighting System Interface and Display Unit FFSIDU

The FFSIDU is an interface and display module of Baruna-1's fire fighting system, it contains 1 main display, selection of input buttons, and small LED indicators.

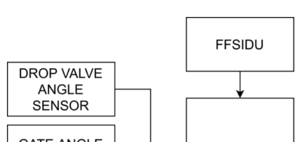

3) **MAN**, or the manual drop button.
4) **HOME, SELECT, MENU**, a set of buttons combination to navigate the parameters and the settings of the ARCC.
5) **DIRECTIONAL BUTTONS**, is in the shape of arrows and has a multiple purpose throughout the FFSIDU navigation control.
6) **LED INDICATORS**, it is an instant indicator for the pilot to know the current condition of the fire fighting system.

Inputs and Sensors

FFSCU requires the necessary data to operate correctly. Various sensors and systems in the aircraft provide the required data, which composed of modules as seen in Figure. 7.4 as well as inside of Table. 7.2.

Sensor	Description
FFS Sensor	
Drop Valve Angle Sensor	The position sensor of dropping valve in degree unit, with raw data given in analog voltage level
Gate Angle Sensor	The position sensor of the gate in degree unit, with raw data given in analog voltage level
Pressure Sensor	A pressure sensor in retardant tank displayed in pascal or psi, with raw data given in analog voltage level
Temperature Sensor	Temperature sensor in the retardant tank, tank head, and surrounding gate assembly, shown in Celcius or Fahrenheit, with raw data given in analog voltage level
Fill Level Sensor	Fill level sensor for measuring the volume of retardant, shown in liter or U.S gallon, with raw data given in analog voltage level
Bleed Valve Sensor	The position sensor of the bleed valve in degree unit, with raw data given in analog voltage level
Aircraft Sensor and Avionics	
GPS	Position and velocity data from GPS for general flight path and mission plan in firefighting system.
ADS IRS	Airspeed, angle of attack, and barometric altitude to calculate both the angle and timing of the drop valve and required for AUTO mode in a firefighting system
RADIO ALT	Low altitude and more precise altitude sensors are required to calculate the firefighting system's ground coverage.

TABLE 7.2: Sensors that are used for FFSCU system to work.

Fully Automatic Drop and Forget System

Our goal to deliver retardants as efficiently as possible is by employing a "fire and forget" system. Certainly, this autonomous system will reduce the workloads of the fire fighting crew. During the pre-drop procedure, the team will select the appropriate setting and dropping scheme in the FFS Interface Module, feeding it into the FFS Control System (FFSCS). The scheme is ranked from fully autonomous to fully manual.

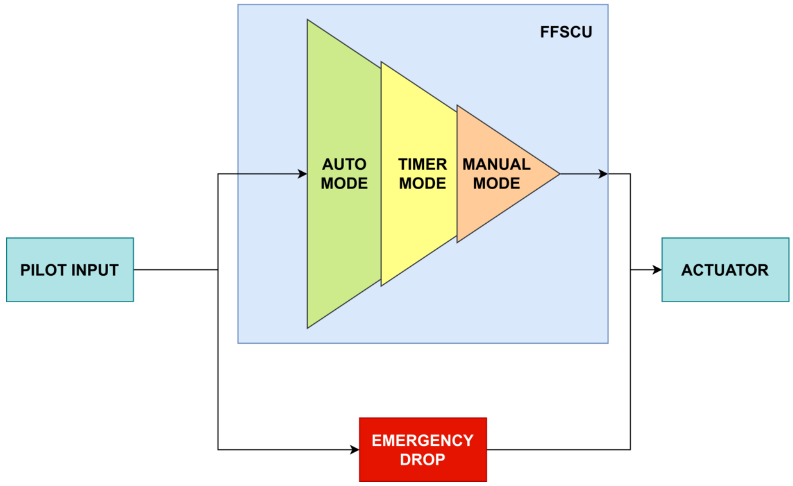

FIGURE 7.5: Modes of operation in the fire fighting system.

1) **Auto Mode**
The FFSCS module controls all aspects of electro-hydraulic management of the drop valve and the bleed air pressure valve to maintain a constant flow of the system. The data that FFSCS requires is obtained from the various FFS sensors and Aircraft sensors.

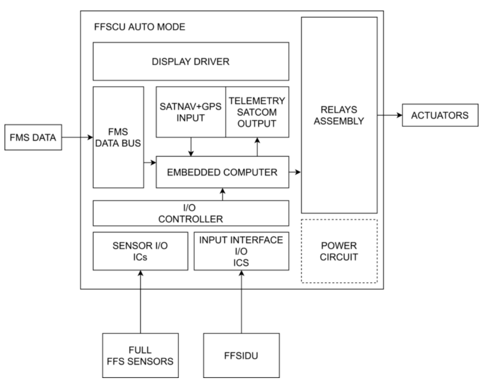

FIGURE 7.6: Auto mode signal pathway diagram.

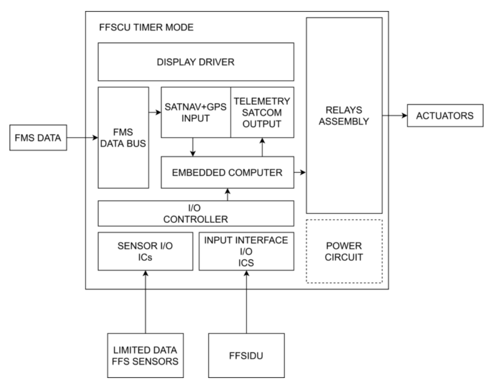

FIGURE 7.7: Timer mode signal pathway diagram.

2) **Timer Mode**
The FFSCS uses its internal timer to determine the valve opening and closing duration. The ability to deliver constant flow or constant pressure depends on the availability of the components

3) **Manual Mode**
Bypassing the FFSCS Automatic system but still provides pilot all electro-hydraulic assist drop. Each partition of the tank is released every time the pilot pushes the manual release button

4) **Emergency Dump**

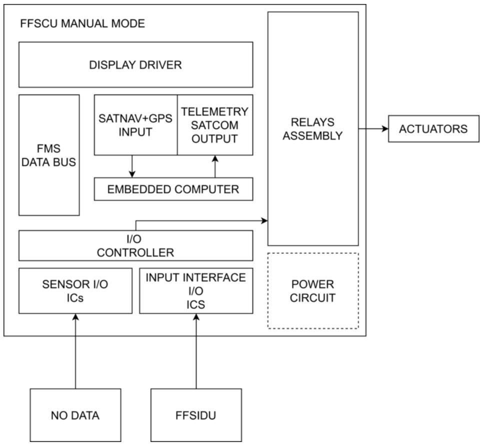

FIGURE 7.8: Manual mode signal pathway diagram.

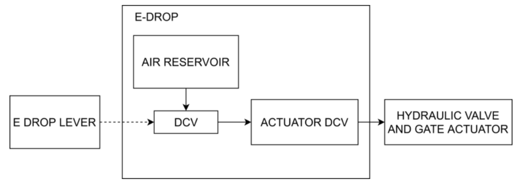

FIGURE 7.9: Emergency drop mechanism diagram.

Bypass all the electronics and release the pressurized air stored in a reservoir to move the DCVs and release all of the payloads manually.

7.1.2 Retardant Tank

General Working of Retardant Tank

The Retardant main tank is responsible for storing the retardant liquid. The tank can hold 4,000 US gallons of retardant liquid, and by utilizing a parallel configuration, the total maximum capacity can be increased to 8,000 US gallons. Each tank is divided into four equal size compartments to enable the multi-drop capability of the fire fighting system. Each tank section has fluid intake, pressure inlet ports, and drop valves.

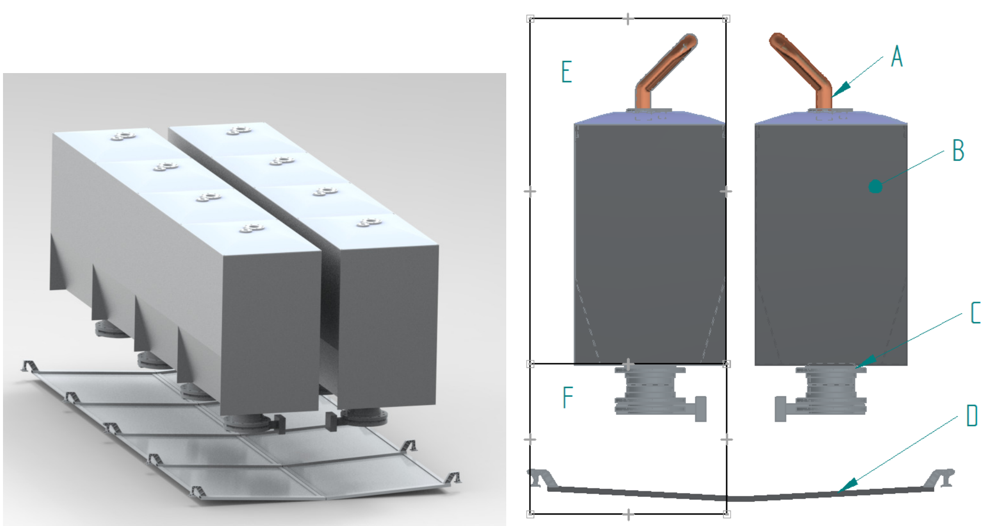

(a) Full Retardant tank assembly.

(b) Detailed description of retardant tank.

FIGURE 7.10: Retardant tank full assembly (a) and its detailed description (b).

Detail Working of Retardant Tank

1) **The Retardant Main Tank**

The retardant tank of Baruna 5 is divided into three main compartments, upper head assembly (A), main tank (B), valve assembly (C), and underbelly gate mechanism (D). The upper head assembly is where all the retardant fluid and pressurize air enter the retardant tank. The main tank is where the retardant liquid is stored. The valve assembly is a section where the valves and their actuator resides. And the underbelly gate is the bottom part, where the opening and closing mechanism and the gate itself are located.

The rectangular section of the main tank is where the main bulk of the liquid is being stored, while the trapezoidal shape at the bottom side of the tank is to ease the flow into the valve assembly.

As to the ASME code standard [104], where non-circular tank thickness constructed from steel must be at least 2.5 mm, the bottom-most part of the tank has a 10 mm wall and floor thickness while the upper part of the tank has a 5 mm thickness wall. And with the partition wall (A) has a thickness of 10 mm. Because of how heavy the steel is, the thickness between the upper and lower sections is differentiated to reduce the tank's weight while maintaining the safety margin imposed by the ASME code.

There is a mounting thread at the top part of the tank to attach the head assembly (B). 4 $\times$ M20 bolts secure every head tank assembly corresponding to every tank partition with a thread depth of 80 mm. And at the bottom of the tank, there is a 14-inch diameter hole to insert the lap joint stub ends and the flange assembly.

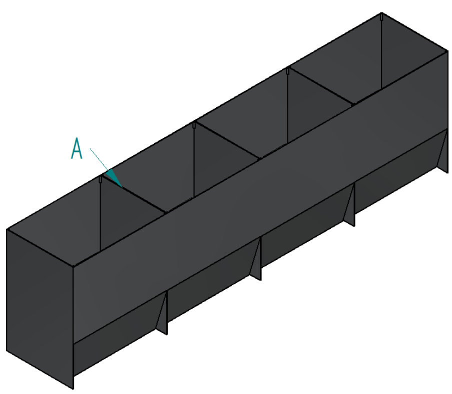

(a) Retardant tank partition separator

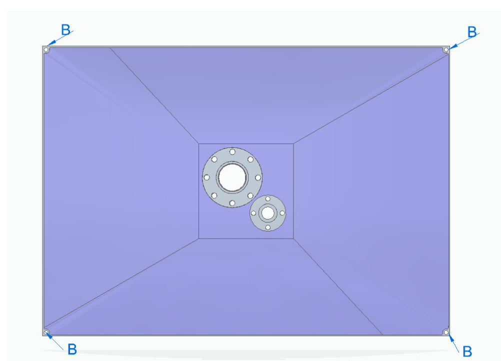

(b) Tank cover mounting threads

FIGURE 7.11: Retardant tank partition schematics (a) and the top view (b)

2) **Dropping Nozzle Assembly**

Baruna-1 FFS uses a butterfly valve as a flow regulator. The butterfly valve offers a compact and precise flow control of the retardant fluid. The valve is mounted using a lap-joint flange and following the class 150 ASME B16.5 and ASME BPVC [104] guideline. The main reason to use a lap-joint flange is to ensure the ease of maintenance. The dropping valve itself is a 14-inch size valve. This massive size is to provide a significant drop rate of retardant delivery. But of course, the crew can increase the drop rate by adjusting the parameter. The FFS then will combine multiple valves to increase the drop rate of the retardant delivery.

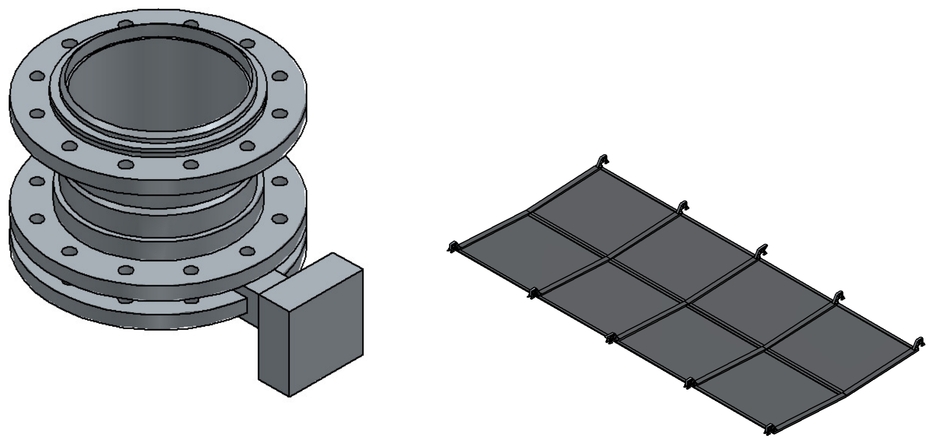

(a) Butterfly valve with its piping flange assembly. (b) Butterfly valve with its piping flange assembly.

FIGURE 7.12: Depictions on how the butterfly valve with its piping and the assembly would look like

3) **Dropping System Gate**

To ensure the lowest drag possible when cruising into the targeted area, we developed a gate right under the valve mechanism of the retardant tank. Not only for providing a smooth surface for the aircraft, but it also protects the fire fighting system.

Physical Properties

	Length	**Width**	**Height**	**Mass**	**Material**		
Retardant Tank	6858 mm	1220 mm	1930 mm	2455 kg	SA203		
Drop Gate	6858 mm	3100 mm	35 mm	363 kg	Al 6013, Al 6050		
Tank Head	1714.5 mm	1220 mm	105 mm	2.5 kg	SA203		
	Max OD	**Max ID**	**Length**	**Height**	**Mass**	**Material**	**Nominal Pipe OD**
Valve Assembly	563.4 mm	355.2 mm	146,1 mm	409.5 mm	150 kg	SA181	355.6 mm
	Length	**Width**	**Height**	**Mass**			
Full Retardant System	6858 mm	2676 mm	3700 mm	6863 kg			

TABLE 7.3: Physical and material properties of the retardant system.

7.1.3 Bleed Air Pressure System

A bleed air system is included in most turbojet and turboprop aircraft architecture. A bleed air system employs a network of ducts, valves, and regulators to transport medium to high-pressure air from the compressor portion of the engine(s) and APU to different points throughout the aircraft [105].

Baruna-1 uses bleed air pressure to minimize the cost of the firefighting budget as it is used for powering the firefighting system. Also, by using this concept, we can make the system more simplified than any other aerial firefighting aircraft. The reason on how precisely the bleed air plays an important role here because it is being used as the pusher for the retardants inside the tanks, which will give a minimum to maximum dropping rate, based on the pilot's desire.

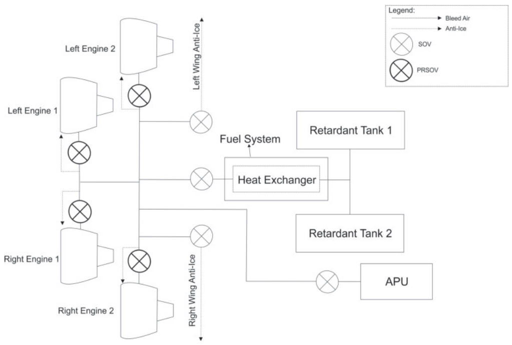

FIGURE 7.13: Bleed Air Pressure System Schematic of Baruna-1.

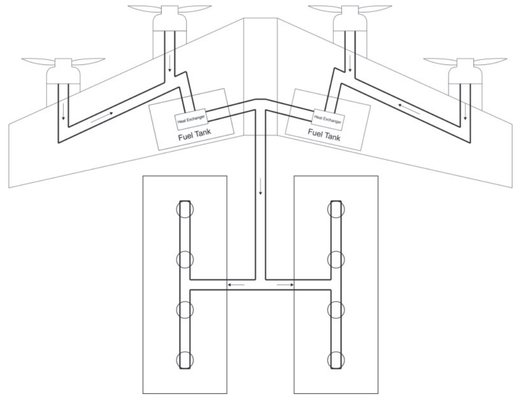

FIGURE 7.14: Baruna-1 Aerial Firefighting's Bleed Air Pressure System, specified to the mechanism of the firefighting system.

As we can see from Figure. 7.13, it shows the overall schematic of the Bleed Air Pressure System as well as it looks similar to the Pneumatic Systems. The components that are bounded with the bleed air pressure system are the 4 Europrop engines, the APU, The De-icing System, and the retardant tanks.

The flow can also be divided into the De-icing and Anti-ice Systems in case of freezing temperature outside of the aircraft. The APU itself could also supply bleed air, but for our aircraft, we decided to use APU as its main function that is to provide power for the engine starting processes.

Heat Exchangers

By looking at the heat exchanger schematic in Figure. **??**, we see that pipes go through the fuel tank to cool the bleed air pressure. The shape of the heat exchanger is similar to the Shell & Tube Heat Exchanger mechanism, where the hot bleed air pressure enters from the left side of the fuel tank and goes out on the right side by bringing cold bleed air pressure, ready to be used for the fire fighting system.

7.1.4 Situational Awareness

Targeting System

Mainly, a targeting system is used frequently in military aircraft. In the case of Baruna-1, we only need to implement Thermal Imaging Devices as our guide and targeting system since our aircraft is an aerial firefighting aircraft.

Using Thermal Imaging Devices as the Baruna-1's Situational Awareness

We have decided to choose Thermal Imaging Devices rather than Night Vision as our situational awareness guiding system because Thermal Imaging Devices are more likely to be advanced and superior to other competitors.

An example of Thermal Imaging Devices usage can be seen in the Figure. **??**. It shows the difference between using only a naked eye (on the left side) with Thermal Imaging Devices (on the right side).

Dropping Method	**Description**	**Time**
Assisted long drop	Maximum longest duration drop by dropping each partition at a time	64 s
Max constant flow salvo	Bleed air pressurized drop only available at auto mode and timer mode	8 s
Max constant pressure salvo	Nonpressurized drop available to manual mode and timer mode	11 s
Drop per single partition	Pressurized drop of each 1000 U.S gallon retardant partition	8 s

TABLE 7.4: Dropping performance of ARCC

Dash Speed	150 kts
Drop Speed	300 kts
Drop Altitude	300 ft AGL

TABLE 7.5: Baruna-1's aircraft performance when dropping

7.2 Ground Fire Fighting Support System

This supporting equipment is used in between flights and typically served to support in the ground power operations, aircraft mobility, and cargo/passenger loading operations.

In terms of ground support for fire fighting, the whole subsystem can be divided into two categories, namely fixed ground support and mobile ground support. The main difference between the fixed and mobile ground support is that the fixed ground support, the retardant and the equipment of supporting the infrastructures, e.g., hoses, pumps, and fixed retardant tank — are available in a particular site. On the other hand, the mobile ground support, utilizes a mobile vehicle with a role of transporting the retardant from the airfield (fixed ground support) to other places necessary.

In viewing their respective roles for Baruna-1's missions, we decided upon using two scenarios (see Table. 7.6). The main difference between the two scenarios lies within the pumps that will be used. For the first scenario, the first pump will be a water pump while the second pump will be a vacuum pump. On the contrary, the second scenario, both pumps will be vacuum pumps.

Scenario	Retardant Tank	Hose	Water Pump	Retardant	Vacuum Pump	Coupling
1	HDWE-FRP-40 [106]	6DJY-0025M [107]	Teflow IH200-150-400 [108]	Enviro class A foam [109]	RGB 510 1D3A [110]	OEM quick npt [111]
2	HDWE-FRP-40 [106]	6DJY-0025M [107]	RGB 510 1D3A [110]	Enviro class A foam [109]	RGB 510 1D3A [110]	OEM quick npt [111]

TABLE 7.6: Fixed ground support scenario

Retardant Tank Truck	Hose	Retardant	Vacuum Pump	Coupling
Tri Axles Diesel Oil Water fuel Tanker [112]	6DJY-0025M [107]	Enviro class A foam [109]	RGB 510 1D3A [110]	OEM quick npt [111]

TABLE 7.7: Mobile ground support scenario

7.2.1 Components of Fixed Ground Support System

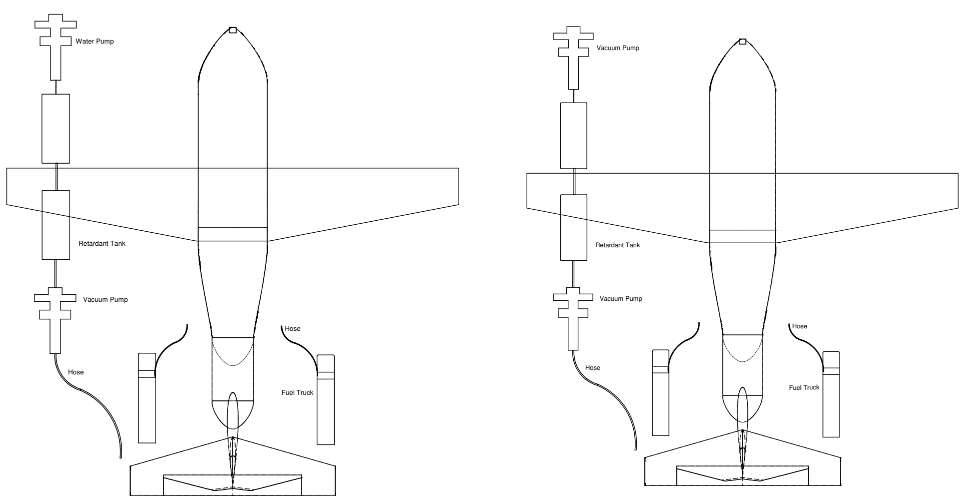

FIGURE 7.15: Description on Baruna-1's fixed ground support system scenarios

We have created schematics for both scenarios of the fixed ground support system, as seen in the the Figure. 7.15 (a) and (b).

Scenario 1

a) **Retardant Tank**, the retardant tank of interest is the HDWE-FRP-40 from Shandong Hard Win International Trading. The shape of the tank is cubical and has a dimension of (4,000 $\times$ 5,000 $\times$ 2,000) mm. volume-wise, it is able to hold 40,000 liters of liquid. The tank is 1,000 kg as the tank is made out of fiberglass. With the capacity in mind, we decided that the number of tank needed is only one unit.

b) **Hose**, the hose of interest is the 6DJY-0025M from FireHoseSupply. The hose has a 6-inch inner diameter and has a length of 25-30 m. The hose uses a double jacket, as it is necessary for an extra layer protection, since the hose will be dragged around on asphalt.

c) **Water Pump**, the water pump of interest is the Teflow from Anhui Tenglong Pump and Valve. The pump has a flow rate of 6,666.7 $\frac{l}{min}$. With this flow rate, the retardant tank will be filled in 4.54 minutes. The dimension of the pump is (2,150 $\times$ 730 $\times$ 890) mm.

(a) Retardant Tank [106].

(b) Hose [107].

(c) Water pump [108].

FIGURE 7.16: Reference images regarding the tank, hose, and water pump

d) **Retardant**, the retardant we have in mind is the Enviro Class A Foam from Fomtec. The retardant has a viscosity of 30 Centipoise at a reasonable price of approximately 1,262 USD [109].

e) **Vacuum Pump**, is used because it can transport dry retardant as well as a liquid such as water, e.g. RGB 510-1D3A from Dongguan Hank Electrical Technology. The pump itself has a dimension of (319.53 $\times$ 333.75 $\times$ 373.88) mm. The flow rate that the pump provided is competitive at 3,500 $\frac{l}{min}$. The vacuum pump has a price of approximately 175 USD.

f) **Coupling**, is used to connect the hose with the pump. The coupling of interest is the Great Wall from Anqing Great Wall Pipeline, as it is quick to install and has corrosion resistance. It has a 6-inch diameter and constructed of a ductile iron. The price per unit of this coupling is approximately 17.85 USD. The number of coupling that we need is six units.

(a) Retardant [109]. (b) Vacuum pump [110]. (c) Coupling [111].

FIGURE 7.17: Reference images regarding the retardant, vacuum pump, and coupling

In summary, the total cost of the scenario 1 would approximately be 6,575.47 USD.

Scenario 2

The difference of scenario 1 and scenario 2 can be seen in the Table. 7.6. For the scenario 1, as it is explained in subsection 7.2.1, we are implementing two kinds of pumps, a regular water pump and a vacuum pump. On the other hand, the scenario 2 will implement only vacuum pumps. The vacuum pump that will be used is the same as describes in subsection 7.2.1 part **e**). The approximate time needed for both vacuum pumps will to operate is 8.65 minutes. The total cost of the scenario 2 would approximately be 8,298.98 USD. The number of personnel we have in mind is at around two to three people — two people in charge of the pumps, and one person in charge of the hose.

7.2.2 Components of Mobile Ground Support System

In a mobile ground support system, we use the same pumps, hose, retardant, and coupling. The only difference in the components that build up the system are the tank, the number of hoses, and the number of couplings (see Figure. 7.18). The difference in fixed and mobile is the means of containing the retardant.

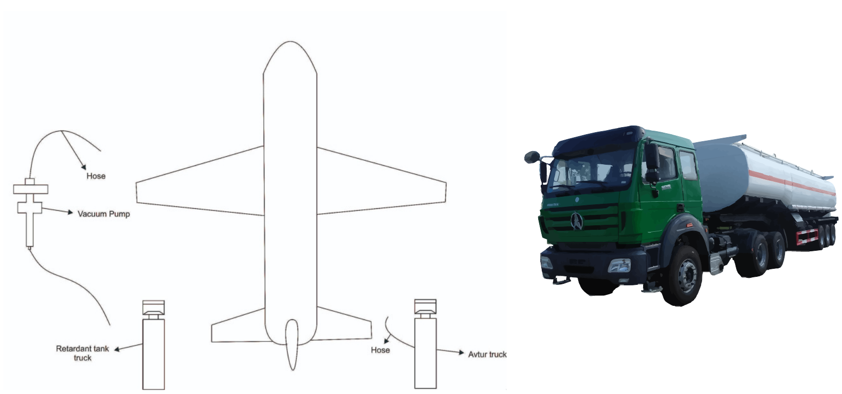

(a) Description on Baruna-1's mobile ground support system (b) Firetruck with tank [112].

FIGURE 7.18: Baruna-1's mobile ground support system

For mobile support the retardant will be carried by a truck, e.g. Tri Axles Diesel Oil Water Fuel Tanker from Chucheng Vehicle Group. The truck has a dimension of (13,800 $\times$ 2,500 $\times$ 3,850) mm, weighting at 14,500 kg. The volume of the tank is 50,000 liters, thus we only need to use one tank/truck in the operation. The time needed for the mobile ground support to do its operation is the same as the scenario 2 of the fixed ground support system, at around 8.65 minutes. This is due to the similar selection of vacuum pump. The price of the truck with a tank is 40,600 USD. Thus, the total cost of this mobile support system is approximately 43,552 USD. The number of personnel we have in mind is at around two to three people; one person driving the truck, one person in charge of the pump, and one person in charge of the hose.

Chapter 8

Stability and Control Design and Analysis

8.1 Static Stability

8.1.1 Tail Design

The horizontal and vertical tails are also important for the aircraft's stability, with the ability to restore the aircraft from yaw and pitch perturbations and control. The T-tail is chosen to be the Baruna-1 tail arrangement, with a smaller vertical tail, because of end-plate effect. The T-tail lifts the horizontal tail clear of the propwash and wing wake which makes the tails more efficient and also reduces buffet on the horizontal tail, which gives an impact of fatigue reduction for the structure and the pilot [113].

There are several steps in designing a tail [114], for which, this is an iterative process based on the analysis of the longitudinal and lateral-directional stability of the Baruna-1 aircraft.

Geometric Properties of Tails and Control Surfaces

The horizontal tail of the Baruna-1 has these geometric parameters: the aspect ratio of 4.5, with a taper of 0.5, 12° sweep angle and the vertical tail has 1.2 aspect ratio with with a taper of 0.5, 12° sweep angle. The NACA 23102 airfoil is used for both horizontal and vertical tail which has a maximum thickness of 12% at 29.8% chord and 1.8% maximum camber at 12.7% chord. This provides a higher maximum lift coefficient and low pitching moment.

The typical values for both horizontal and vertical tail volume coefficient is used as an approach in designing the tail, with horizontal and vertical tail volume coefficient are $\vec{V}_H = 1$ and $\vec{V}_V$ for Bomber/Military transport according to Sadrey[114]. The tail arm that associated with the horizontal and vertical tail which denoted as l_T is expressed by[32]:

$$l_T = \sqrt{\frac{2 \cdot S\,(V_{HT} \cdot \vec{c} + V_{VT} \cdot b)}{\pi\,(R_1 + R_2)}} \tag{8.1}$$

Furthermore, the control surfaces, elevators and rudder is designed based on the typical values for control surfaces geometry[114]. The elevators is located in 65% of the horizontal tail root chord, with the elevator chord is 35% of the horizontal tail root chord. The rudder is located in 70% of the vertical tail root chord, with the rudder ratio to the vertical tail area is 25% and the rudder chord is 30% of the vertical tail root chord.

Based on the value of tail arm and the definition of the control surfaces geometry, the geometric properties of the horizontal and vertical tail are shown in the table below and in Figure. 8.1.

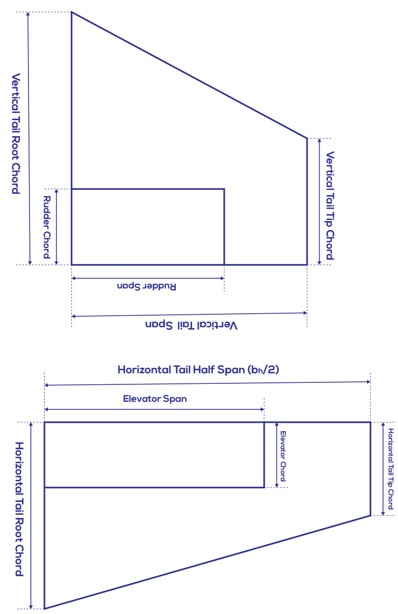

FIGURE 8.1: Geometric properties of the tail and control surfaces

Geometric properties	Horizontal tail	Vertical Tail
Setting angle (deg)	0	0
Area (m^2)	48.9337	31.3176
Chord (m)	3.2976	5.1086
c_{root} (m)	4.2398	6.5682
c_{tip} (m)	2.1199	3.2841
Span (m)	14.8392	6.1303
Dependent Tail Arm (m)	20.4358	
Geometric properties	**Elevator**	**Rudder**
Area (m^2)	7.4196	7.8294
Chord (m)	1.4839	1.9705
Span (m)	5	3.9734

TABLE 8.1: Geometric Properties of the Tails and Control Surfaces

8.1.2 Static Stability

Longitudinal Static Stability

The longitudinal static stability is characterized by the pitching moment coefficient changes with the angle of attack (C_{m_α}), the aircraft neutral point ($\vec{X}_{np}$) and the static margin (SM)[114].

1. The pitching moment coefficient changes with the angle of attack (C_{m_α}) The longitduinal static stability is calculated at cruise condition. Requirement for Static Stability:

$$C_{m_\alpha} = \frac{\partial C_m}{\partial \alpha} < 0 \tag{8.2}$$

The C_{m_α} mathematically is calculated using the Snorri Gudmundsson's methodology (Snorri) as shown below.

$$\begin{aligned} C_{m_\alpha} =& C_{m_{\alpha_W}} + C_{m_{\alpha_{FUS}}} + C_{m_{\alpha_{HT}}} + \dots \\ C_{m_\alpha} =& C_{L_{\alpha_{WF}}} (\vec{X}_{CG} - \vec{X}_{AC_{WF}}) - \eta_{HT} V_{HT} C_{L_{\alpha_{HT}}} \left(1 - \frac{d\varepsilon}{d\alpha}\right) \end{aligned} \tag{8.3}$$

The contribution of the wing and fuselage are calculated parallel, with the correction K_{WB} in the calculation of $C_{L_{\alpha_{WF}}}$. The wing+fuselage aerodynamic center is calculated using the Torenbeek's methodology.

$$\left(\frac{X_{ac}}{\bar{c}}\right)_{wf} = \left(\frac{X_{ac}}{\bar{c}}\right)_{w} + \frac{\Delta_{f1} X_{ac}}{\bar{c}} + \frac{\Delta_{f2} X_{ac}}{\bar{c}} \tag{8.4}$$

Where, the correction $\Delta_{f1} X_{ac}$ indicates the forward shift due to the fuselage sections forward and aft of the wing and the correction $\Delta_{f2} X_{ac}$ accounts for the lift loss in the region where the wing-fuselage lift carry-over is focused. The η_{HT} is considered to be 1 for T-tail configuration which the wing and fuselage do not impact the tail dynamic pressure (Snorri). As a result, the pitching moment coefficient changes with the angle of attack C_{m_α} is -2.939, which this result is fulfill the requirement as shown above and the Baruna-1 aircraft is longitudinal statically stable at cruise condition.

2. The aircraft neutral point ($\vec{X}_{np}$) The aircraft neutral point $\vec{X}_{np}$, also called as the aircraft aerodynamic center $\vec{X}_{AC}$ is calculated using the Marcello R. Napolitano's methodology[115].

$$\vec{X}_{AC} = \frac{\vec{X}_{AC_{WF}} + \frac{C_{L_{\alpha_{HT}}}}{C_{L_{\alpha_W}}} \eta_{HT} \frac{S_{HT}}{S} \left(1 - \frac{d\varepsilon}{d\alpha}\right) \vec{X}_{AC_{HT}}}{1 + \frac{C_{L_{\alpha_{HT}}}}{C_{L_{\alpha_W}}} \eta_{HT} \frac{S_{HT}}{S} \left(1 - \frac{d\varepsilon}{d\alpha}\right)} \tag{8.5}$$

As a result, the neutral point of the Baruna-1 is located on 57.644% with respect to the wing mean aerodynamic chord.

3. The static margin (SM) The static margin is the distance between the aircraft aerodynamic center and the aircraft CG with respect to the wing mean aerodynamic chord, as expressed below [32]:

$$SM = -100\left(\vec{X}_{CG} - \vec{X}_{AC}\right) \tag{8.6}$$

The static margin for Baruna-1 is 54.957% which in general for cargo aircrafts, having larger values for the static margin, will allows the loading flexibility and wider allowed ranges of the aircraft CG [115].

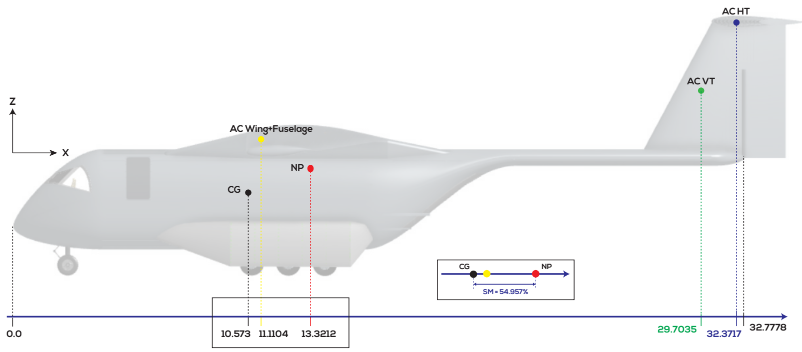

FIGURE 8.2: Location of the CG, AC, neutral point and the static margin of Baruna-1

Lateral Static Stability

Lateral stability is the tendency of an aircraft to level its wing during yaw and the aircraft is lateral statically stable if it generates a negative rolling moment when subjected to a positive sideslip angle β[32]. The lateral static stability is calculated at cruise condition.

The requirement for the lateral static stability[32]:

$$C_{l_\beta} = \frac{\partial C_l}{\partial \beta} < 0 \quad \text{and} \quad Cl = 0 \quad \text{if} \quad \beta = 0 \tag{8.7}$$

Where the C_{l_β} is calculated using the Marcello R. Napolitano's methodology[115], as expressed below.

$$\begin{aligned}
C_{l_\beta} &= C_{l_{\beta_{WB}}} + C_{l_{\beta_{HT}}} + C_{l_{\beta_{VT}}} \\
C_{l_{\beta_{WB}}} &= 57.3 \cdot C_{L_1} \left(\left(\frac{C_{l_\beta}}{C_{L_1}} \right)_{\Lambda_{c/2}} K_{M_\Lambda} K_f + \left(\frac{C_{l_\beta}}{C_{L_1}} \right)_{AR} \right) \\
&\quad + 57.3 \left(\Gamma_W \left(\frac{C_{l_\beta}}{\Gamma_W} K_{M_\Gamma} + \frac{\Delta C_{l_\beta}}{\Gamma_W} \right) + \left(\Delta C_{l_\beta} \right)_{Z_W} + \varepsilon_W \tan \Lambda_{c/4} \left(\frac{\Delta C_{l_\beta}}{\varepsilon_W \tan \Lambda_{c/4}} \right) \right) \\
C_{l_{\beta_{HT}}} &\approx 0 \\
C_{l_{\beta_{VT}}} &= C_{y_{\beta_{VT}}} \cdot \frac{(Z_V \cos \alpha_1 - X_V \sin \alpha_1)}{b}
\end{aligned} \tag{8.8}$$

As a result, the C_{l_β} is -0.006, which meets the requiremet $C_{l_\beta} < 0$ and the Baruna-1 aircraft is lateral statically stable at cruise condition.

Directional Static Stability

Directional stability is the capability of the aircraft to weathervane with the slope of the yawing moment curve must have a positive slope[32], which in matematical expression is shown below. The directional static stability is calculated at cruise condition.

The requirement for the directional static stability[32]:

$$C_{n_\beta} = \frac{\partial C_n}{\partial \beta} > 0 \quad \text{and} \quad Cn = 0 \quad \text{if} \quad \beta = 0 \tag{8.9}$$

Where the C_{n_β} is calculated using the Marcello R. Napolitano's methodology[115], as expressed below.

$$\begin{aligned}
C_{n_\beta} &= C_{n_{\beta_W}} + C_{n_{\beta_B}} + C_{n_{\beta_{HT}}} + C_{n_{\beta_{VT}}} \\
C_{n_{\beta_W}} &\approx 0 \\
C_{n_{\beta_B}} &= -57.3 \cdot K_N K_{R_l} \frac{S_{B_S}}{S} \frac{l_B}{b} C_{n_{\beta_{HT}}} \approx \quad 0 \\
C_{n_{\beta_{VT}}} &= -C_{y_{\beta_{VT}}} \cdot \frac{(X_V \cos\alpha_1 + Z_V \sin\alpha_1)}{b}
\end{aligned} \tag{8.10}$$

As a result, the C_{n_β} is 0.00062, which meets the requiremet $C_{n_\beta} > 0$ and the Baruna-1 aircraft is directional statically stable at cruise condition.

8.2 Dynamic Stability

8.2.1 Dynamic Stability

The dynamic stability is reffered as the tendency of an aircraft, without pilot assistance, to recover to the initial steady-state trim condition after the effect of a disturbance[32]. The Baruna-1 aerodynamic and control stability derivates are calculated using the Snorri Gudmundsson's[32], Marcello R. Napolitano's[115], Torenbeek's[116], Sadrey's[114] and Roskam's[30] methodologies. The stability derivatives are used to construct the linear equation of motions in form of state-space matrix form.

The result of the calculation for the Baruna-1 stability and control derivatives are shown below in Table.8.2 for Longitudinal and Lateral-Directional.

Stability and Control Derivatives of Baruna-1					
Longitudinal			**Lateral-Directional**		
Derivatives	**Take-off**	**Cruise**	**Derivatives**	**Take-off**	**Cruise**
C_{D_α}	0.698090	0.223829	C_{y_β}	-2.555388	-2.555388
C_{L_α}	5.822459	5.822459	C_{l_β}	0.030368	-0.006050
C_{m_α}	-2.939053	-2.939053	C_{n_β}	0.001983	0.000615
C_{D_u}	0.104000	0.104000	C_{y_p}	0.003964	-0.032782
C_{L_u}	0.103135	0.211526	C_{l_p}	-0.458280	-0.458280
C_{m_u}	-0.050000	-0.050000	C_{n_p}	-0.026360	0.002898
C_{L_q}	13.282255	13.878096	C_{y_r}	0.194946	0.192210
C_{m_q}	-41.872091	-41.872091	C_{l_r}	0.327548	0.148225
$C_{L_{\dot\alpha}}$	3.768147	3.768147	C_{n_r}	-0.479696	-0.181171
$C_{m_{\dot\alpha}}$	-17.088355	-17.088355	$C_{y_{\delta_a}}$	0.000000	0.000000
$C_{L_{i_H}}$	0.996924	0.996924	$C_{l_{\delta_a}}$	0.101347	0.101347
$C_{D_{i_H}}$	0.000000	0.000000	$C_{n_{\delta_a}}$	0.003245	0.001040
$C_{m_{i_H}}$	-4.521002	-4.521002	$C_{y_{\delta_r}}$	0.087917	0.087917
$C_{L_{\delta_e}}$	0.342796	0.342796	$C_{l_{\delta_r}}$	-0.003944	0.010111
$C_{m_{\delta_e}}$	-1.554561	-1.554561	$C_{n_{\delta_r}}$	-0.074331	-0.073746
$C_{T_{X_1}}$	0.084063	0.015183	$C_{n_{T_\beta}}$	0.002438	0.002438
$C_{m_{T_1}}$	0.000000	0.000000			
$C_{T_{X_u}}$	-0.252190	-0.045548			
$C_{m_{T_u}}$	-0.045184	-0.008161			
$C_{m_{T_\alpha}}$	0.000000	0.000000			

TABLE 8.2: Longitudinal and lateral-directional stability and control derivatives of Baruna-1.

The Baruna-1 Stability and Control State-Space Matrix

The state-space matrix is constructed to analyze the Baruna-1 dynamic stability using the stability and control derivatives8.2. The matrix form is:

$$\dot{x} = Ax + Bu \tag{8.11}$$

For longitudinal, A is the longitudinal state matrix, B is the longitudinal input matrix, x represents the set of longitudinal state variables $x = [u, \alpha, q, \theta]^T$ and u is the longitudinal control surface $u = [\delta_E]^T$. For lateral-directional, A is the lateral-directional state matrix, B is the lateral-directional input matrix, x represents the set of lateral-directional state variables $x = [\beta, p, r, \phi]^T$ and u is the input vector $u = [\delta_A, \delta_R]^T$. The aircraft transfer functions at take-off condition with 9.6 degree angle of attack, and at cruise condition with -1.244 degree trim angle of attack.

Take-off	Cruise
$\frac{u(s)}{\delta_e(s)} = \frac{-2.527s^4 - 0.111s^3 - 0.00102s^2 + 1.645e{-}06s + 1.505e{-}09}{s^4 + 0.4932s^3 + 0.02284s^2 + 1.582e{-}07s + 1.703e{-}08}$	$\frac{u(s)}{\delta_e(s)} = \frac{-8.144s^4 - 0.1298s^3 + 0.001333s^2 + 1.128e{-}05s - 2.554e{-}08}{s^4 + 0.7113s^3 + 0.01514s^2 + 2.923e{-}07s + 8.696e{-}08}$
$\frac{\alpha(s)}{\delta_e(s)} = \frac{-0.1168s^2 + 1.421e{-}05s + 1.046e{-}05}{s^4 + 0.4932s^3 + 0.02284s^2 + 1.582e{-}07s + 1.703e{-}08}$	$\frac{\alpha(s)}{\delta_e(s)} = \frac{-0.1817s^2 + 4.55e{-}05s + 5.155e{-}05}{s^4 + 0.7113s^3 + 0.01514s^2 + 2.923e{-}07s + 8.696e{-}08}$
$\frac{q(s)}{\delta_e(s)} = \frac{-0.02699s^3 - 0.0007653s^2 - 1.148e{-}07s - 5.319e{-}08}{s^4 + 0.4932s^3 + 0.02284s^2 + 1.582e{-}07s + 1.703e{-}08}$	$\frac{q(s)}{\delta_e(s)} = \frac{-0.04072s^3 - 0.0007358s^2 - 1.34e{-}07s - 5.038e{-}08}{s^4 + 0.7113s^3 + 0.01514s^2 + 2.923e{-}07s + 8.696e{-}08}$
$\frac{\theta(s)}{\delta_e(s)} = \frac{-2.628e{-}06s^3 - 1.171e{-}06s^2 - 5.422e{-}08s - 2.988e{-}30}{s^4 + 0.4932s^3 + 0.02284s^2 + 1.582e{-}07s + 1.703e{-}08}$	$\frac{\theta(s)}{\delta_e(s)} = \frac{-8.471e{-}06s^3 - 5.403e{-}06s^2 - 1.169e{-}07s - 2.107e{-}30}{s^4 + 0.7113s^3 + 0.01514s^2 + 2.923e{-}07s + 8.696e{-}08}$
$\frac{\beta(s)}{\delta_a(s)} = \frac{-7.564e{-}09s^3 - 7.777e{-}07s^2 - 1.609e{-}06s - 9.44e{-}13}{s^4 + 0.2028s^3 + 2.78e{-}07s^2 - 2.524e{-}08s - 1.516e{-}14}$	$\frac{\beta(s)}{\delta_a(s)} = \frac{-2.836e{-}07s^3 - 1.049e{-}05s^2 - 7.802e{-}06s - 2.585e{-}12}{s^4 + 0.3053s^3 + 4.929e{-}07s^2 + 7.669e{-}09s + 2.272e{-}15}$
$\frac{p(s)}{\delta_a(s)} = \frac{4.088e{-}08s^2 + 8.473e{-}08s + 4.973e{-}14}{s^4 + 0.2028s^3 + 2.78e{-}07s^2 - 2.524e{-}08s - 1.516e{-}14}$	$\frac{p(s)}{\delta_a(s)} = \frac{1.704e{-}07s^2 + 1.278e{-}07s + 4.236e{-}14}{s^4 + 0.3053s^3 + 4.929e{-}07s^2 + 7.669e{-}09s + 2.272e{-}15}$
$\frac{r(s)}{\delta_a(s)} = \frac{8.118e{-}07s^3 + 1.646e{-}07s^2 + 1.016e{-}13s + 7.232e{-}17}{s^4 + 0.2028s^3 + 2.78e{-}07s^2 - 2.524e{-}08s - 1.516e{-}14}$	$\frac{r(s)}{\delta_a(s)} = \frac{2.614e{-}06s^3 + 7.98e{-}07s^2 + 2.953e{-}13s - 6.143e{-}17}{s^4 + 0.3053s^3 + 4.929e{-}07s^2 + 7.669e{-}09s + 2.272e{-}15}$
$\frac{\phi(s)}{\delta_a(s)} = \frac{-4.096e{-}08s^3 - 8.305e{-}09s^2 - 2.312e{-}15s + 4.782e{-}16}{s^4 + 0.2028s^3 + 2.78e{-}07s^2 - 2.524e{-}08s - 1.516e{-}14}$	$\frac{\phi(s)}{\delta_a(s)} = \frac{-1.718e{-}07s^3 - 5.244e{-}08s^2 + 1.095e{-}14s + 1.568e{-}15}{s^4 + 0.3053s^3 + 4.929e{-}07s^2 + 7.669e{-}09s + 2.272e{-}15}$
$\frac{\beta(s)}{\delta_r(s)} = \frac{0.6533s^4 + 7.873e{-}07s^3 - 7.945e{-}06s^2 - 1.642e{-}07s + 3.93e{-}13}{s^4 + 0.2028s^3 + 2.78e{-}07s^2 - 2.524e{-}08s - 1.516e{-}14}$	$\frac{\beta(s)}{\delta_r(s)} = \frac{2.1s^4 + 2.581e{-}06s^3 - 8.301e{-}05s^2 - 1.021e{-}06s + 1.454e{-}12}{s^4 + 0.3053s^3 + 4.929e{-}07s^2 + 7.669e{-}09s + 2.272e{-}15}$
$\frac{p(s)}{\delta_r(s)} = \frac{0.006976s^3 + 4.266e{-}07s^2 + 7.778e{-}09s - 2.105e{-}14}{s^4 + 0.2028s^3 + 2.78e{-}07s^2 - 2.524e{-}08s - 1.516e{-}14}$	$\frac{p(s)}{\delta_r(s)} = \frac{0.0105s^3 + 1.373e{-}06s^2 + 1.698e{-}08s - 2.381e{-}14}{s^4 + 0.3053s^3 + 4.929e{-}07s^2 + 7.669e{-}09s + 2.272e{-}15}$
$\frac{r(s)}{\delta_r(s)} = \frac{1.184e{-}08s^3 + 4.093e{-}09s^2 + 5.087e{-}14s + 1.589e{-}15}{s^4 + 0.2028s^3 + 2.78e{-}07s^2 - 2.524e{-}08s - 1.516e{-}14}$	$\frac{r(s)}{\delta_r(s)} = \frac{3.998e{-}07s^3 + 1.204e{-}07s^2 - 3.345e{-}13s + 3.938e{-}16}{s^4 + 0.3053s^3 + 4.929e{-}07s^2 + 7.669e{-}09s + 2.272e{-}15}$
$\frac{\phi(s)}{\delta_r(s)} = \frac{-4.182e{-}07s^3 - 8.485e{-}08s^2 - 6.629e{-}14s + 1.05e{-}14}{s^4 + 0.2028s^3 + 2.78e{-}07s^2 - 2.524e{-}08s - 1.516e{-}14}$	$\frac{\phi(s)}{\delta_r(s)} = \frac{-1.36e{-}06s^3 - 4.151e{-}07s^2 - 4.802e{-}13s - 1.005e{-}14}{s^4 + 0.3053s^3 + 4.929e{-}07s^2 + 7.669e{-}09s + 2.272e{-}15}$

TABLE 8.3: Transfer functions of Baruna-1 at Take-off and Cruise conditions

The Baruna-1 Longitudinal and Lateral-Directional Modes

The Baruna-1 aircraft is longitudinal and lateral-directional dynamically unstable at take-off condition and longitudinal dynamically unstable but lateral-directional dynamically stable. Since the Baruna-1 aircraft is unstable in certain condition as stated before, the application of the Stability Augmentation System to the state-space matrix is applied.

Using the closed-loop transfer functions, with the airspeed feedback gains $k_u = -0.001$ and aileron sideslip gain $k_{\beta_A} = 0.5$ at take-off condition and airspeed feedback gain $k_u = -0.0016$ at cruise condition, the eigenvalues, damping coefficient, natural frequency and time constant for Baruna-1 at take-off and cruise condition for both longitudinal and lateral-directional are shown below in Table.8.5

In longitudinal modes, the short period is characterized by relatively high damping coefficient ζ_{SP} values as well as high natural frequency $\omega_{n_{SP}}$ values and the phugoid is characterized by low damping coefficient ζ_{PH} as well as low natural frequency ω_{PH}. In lateral-directional modes, the durtch roll is characterized by moderate values of the damping coefficient ζ_{DR} as well as moderate values of the natural frequecy $\omega_{n_{DR}}$. The spiral is a slow first order mode, leading to a very large value of the associated time

Modes	Take-off		Cruise	
	Longitudinal	**Lateral-Directional**	**Longitudinal**	**Lateral-Directional**
Poles	-0.4411985 -0.0520411 -0.0000000613+ 0.0005349i -0.0000000613 - 0.0005349i	-0.2027715 -0.000000566 -0.000000244 + 0.000291i -0.000000244 - 0.000291i	-0.6889 -0.0224 -0.00000041 + 0.000539i -0.00000041 - 0.000539i	-0.30525 -0.0000003 -0.000000618 + 0.000158i -0.000000618 - 0.000158i
Damping	1 (Shord-Period) 0.004557 (Phugoid)	0.00084 (Dutch Roll)	1 (Shord-Period) 0.000763 (Phugoid)	0.003899 (Dutch Roll)
Frequency (rad/s)	0.4412 (Shord-Period) 0.000535 (Phugoid)	0.000291 (Dutch Roll)	0.6889 (Shord-Period) 0.000539 (Phugoid)	0.000158 (Dutch Roll)
Time Constant (s)	-	4.93 (Roll) 1765218.9 (Spiral)	-	3.27 (Roll) 3375447.4 (Spiral)

TABLE 8.5: The eigenvalues, damping, natural frequency, and time constant of Baruna-1 at take-off and cruise.

constant T_S. Lastly, the rolling is a fast first order mode associated with the time constant T_R.

As shown in Table.8.2, the Baruna-1 aircraft for both longitudinal and lateral-directional modes at take-off and cruise conditions become dynamically stable after the application of SAS to the state-space matrix.

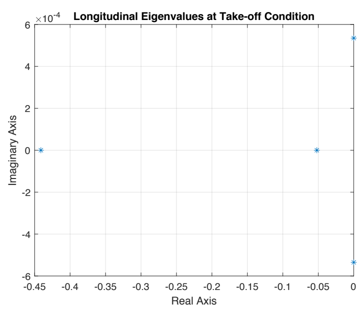

(a) Longitudinal eigenvalues at take-off condition

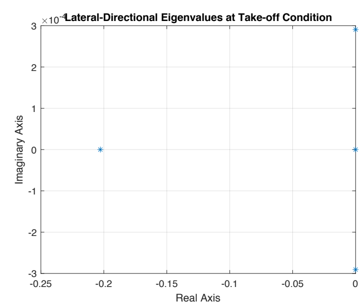

(b) Lateral-directional eigenvalues at take-off condition

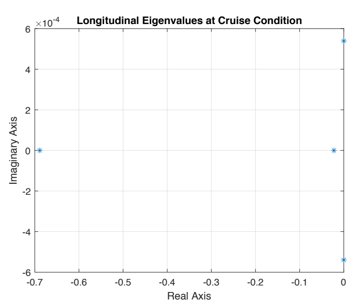

(c) Longitudinal eigenvalues at cruise condition

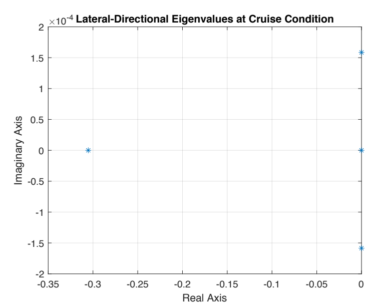

(d) Lateral-directional eigenvalues at cruise condition

FIGURE 8.3: Longitudinal eigenvalues and lateral-directional of both take-off and cruise conditions.

Chapter 9

Aircraft Performance

9.1 Mission Profile

Baruna-1's mission profiles are similar to that of a military bomber aircraft. However, instead of dropping bombs, Baruna-1 will drop fire retardants onto burning areas (see Figure. 9.1 and Figure. 9.2 for Baruna-1's mission profile).

9.1.1 Fire Fighting Mission

As shown in Figure. 9.1, The aircraft will drop three separate batches of fire retardants at an approximate altitude of 100 meters (∼300 feet) above the ground. Each drop phase will last approximately 1 minute, while the loiter phase after the Drop 1 and Drop 2 phases will take around 15 minutes each. Moreover, at both cruising phases, the aircraft will maintain an altitude of 3,500 m (∼11,500 ft) due to the airfoil's critical Mach Number. In the Cruise 2 phase, the aircraft will cruise at its dashing speed of 206 m/s (400 knots). In the Loiter 3 phase, the aircraft will fly at around 3,048 m (∼10,000 ft). Lastly, the aircraft will remain in the Loiter 3 phase for approximately 45 minutes if the aircraft were to make an Instrument approach.

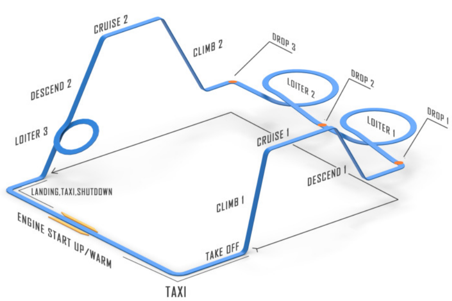

FIGURE 9.1: Baruna-1's fire fighting mission profile.

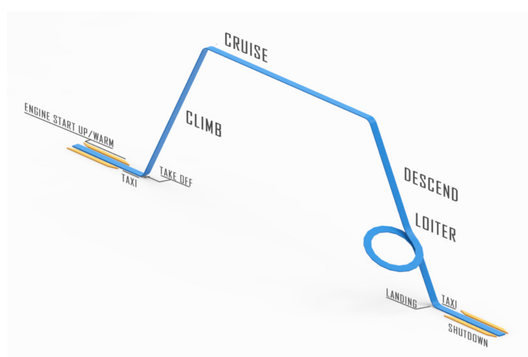

FIGURE 9.2: Baruna-1's ferry mission profile.

9.1.2 Ferry Mission

Baruna-1's ferry mission profile in Figure. 9.2 is similar to that of a typical commercial aircraft mission profile. Like the firefighting mission profile, the aircraft will cruise at 3,500 m (∼11,500 ft) and, at its loiter phase before landing, will last for approximately 45 minutes if it were to make an instrument approach.

9.2 Lift and Drag Polar

Figure. 2.13 in Chapter. **??** shows the lift drag polar diagram. From the figure, three configurations can be found which represents the aircraft with $\Delta f = 0°$ and $\Delta s = 0°$ (clean configuration), $\Delta f = 30°$ and $\Delta s = 0°$ and $\Delta f = 30°$ and $\Delta s = 20°$ each with different k, C_{LD} and C_{D0} values. For the purpose of performance analysis, the following aerodynamic coefficient ratios can be found in Table. 9.1, which were based on the lift drag polar graph. Also, three graphs were produced (see Figure. 9.3 (a) to (c)).

C_L at $\frac{C_L}{C_D}$	$\left(\frac{C_L}{C_D}\right)_{\max}$	C_L at $\frac{C_L^3}{C_D^2}$	$\left(\frac{C_L^3}{C_D^2}\right)_{\max}$	C_L at $\frac{C_L}{C_D^2}$	$\left(\frac{C_L}{C_D^2}\right)_{\max}$
0.703	15.416	1.192	214.533	0.416	435.337
0.806	12.532	1.315	159.787	0.494	246.563
0.970	11.053	1.655	152.902	0.568	162.295

TABLE 9.1: Aerodynamic Coefficient Ratios

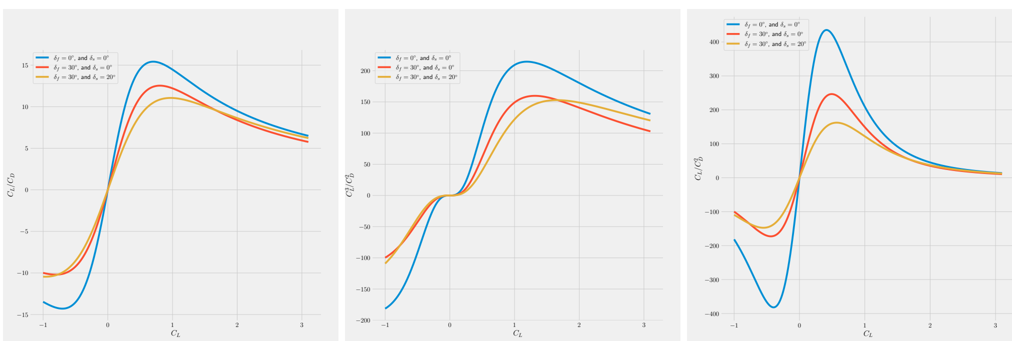

(a) C_L vs $\frac{C_L}{C_D}$ (b) C_L vs $\frac{C_L^3}{C_D^2}$ (c) C_L vs $\frac{C_L}{C_D^2}$

FIGURE 9.3: Aerodynamics coefficient ratios.

The trends shown in the three figures (Figure. 9.3 (a) to (c)) are very similar to one another. It can be seen that the configuration with $\Delta f = 0°$ and $\Delta s = 0°$ have the highest slope among the others followed by the configuration with $\Delta f = 30°$ and $\Delta s = 0°$ and finally, the configuration with $\Delta f = 30°$ and $\Delta s = 20°$. The only difference between the trends is that even though all of Figure. 9.3 trends are similar, Figure. 9.3(b) plateaus at $C_L = 0$ before continuing its uptrend.

9.3 Payload Range

Assuming that Baruna-1 carries maximum fuel and is solely used for cruising, the payload range can be described as shown in Figure. 9.4. The depiction shows the range, in km, that the aircraft can travel under MTOW and EMTOW conditions at an altitude of 3,500 m (blue line). At an MTOW of 150,000 kg, the aircraft can travel as far as ∼9,000 km, while at an EMTOW of ∼105,000 kg, it can travel up to ∼14,000 km.

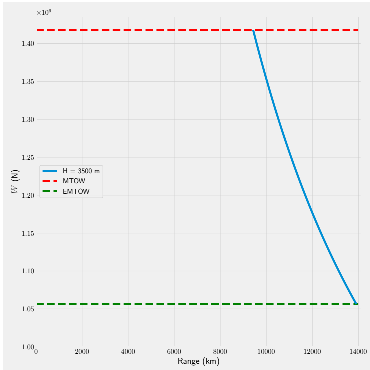

FIGURE 9.4: Baruna-1's Payload Range.

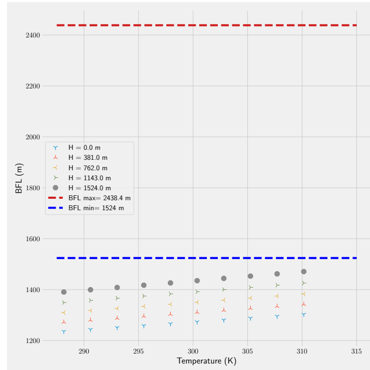

FIGURE 9.5: Balanced field length

9.4 Mission Radius and Ferry Range

Baruna-1's mission radius and ferry range is described in Figure. 9.6 (a) and (b) respectively. Figure. 9.6(a) shows the maximum mission radius of Baruna-1 with different fuel weight fractions $\left(\frac{W_f}{W_{f\max}}\right)$ and retardant weight fractions $\left(\frac{W_r}{W_{r\max}}\right)$. Judging by the figure, Baruna-1 will exceed the RFP's objective radius of around 741 km. Even with the maximum fuel and retardant weight fractions, it still exceeds the objective radius with plenty of space.

In contrast, Figure. 9.6(b) represents the ferry range of Baruna-1 at different fuel weight fractions and without any payload onboard. As shown, even with a 0.5 fuel weight fraction, Baruna-1 can cover a distance of up to around 6,500 km, exceeding the RFP's objective ferry range. With maximum fuel weight fraction, Baruna-1 can cover a maximum distance of approximately 12,500 km.

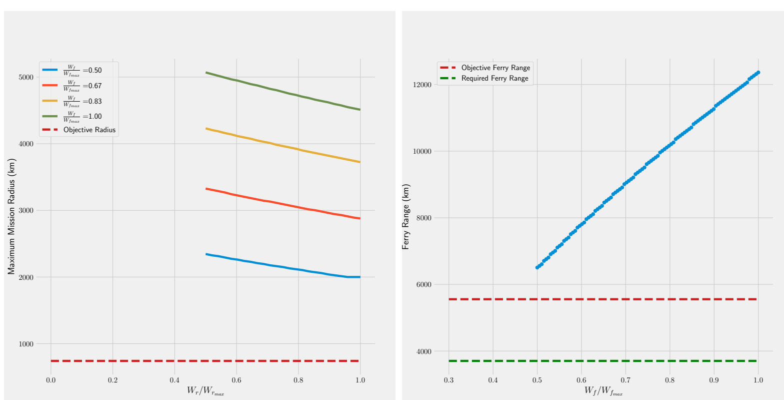

(a) Mission radius (b) Ferry range

FIGURE 9.6: Mission radius and ferry range of Baruna-1.

9.5 Balanced Field Length

Based on the RFP, the required balanced field length is 1,524 m, while the objective, balanced field length is 2,438.4 m. Figure. 9.5 shows these requirements, dashed blue line for the objective balanced field length, and the red dashed line for the required balanced field length. The graph shows the relationship between the balanced field length and the temperature measured in Kelvin. It is seen that there are multiple colored triangle-like plots and a gray-colored dotted plot that represents Baruna-1's balanced field length required on different elevations at various temperatures. It is shown that Baruna-1's balanced field length is far lower than the required balanced field length, which is a remarkable feat to obtain.

9.6 Take-off Distance

The take-off distance for different elevations at various temperatures of Baruna-1 is shown in Figure. 9.7, $C_L = 1.3$ was used for plotting this graph, and as seen also, it has an uptrend as the temperature increases. It is also seen that as the elevation increases, the take-off distance required for Baruna-1 also increases, up to ~1,052 m. The take-off distance already encompasses the ground roll, transition, rotation, and climbing.

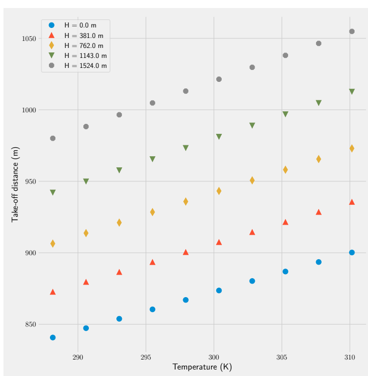

FIGURE 9.7: Take-off distance.

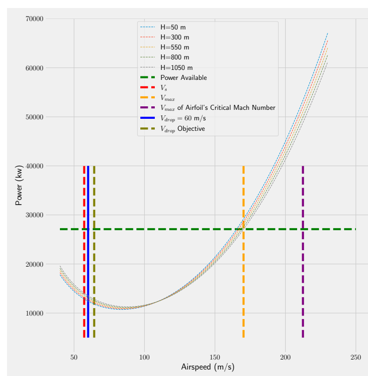

FIGURE 9.8: Baruna-1's drop speed with full flaps extension

9.7 Drop Speed

Baruna-1's drop speed with full flaps extension is depicted in Figure X.11. The horizontal green dashed line in the figure represents the power available of the aircraft set to 85% of installed thrust. The power available is assumed constant throughout varying airspeeds. The drop speed objective written in the RFP requires the aircraft to have a drop speed of 64.3 $\frac{m}{s}$ (125 knots) or below, as represented by the vertical gray dashed line. As described by the blue line, Baruna-1 has a drop speed of approximately 60 $\frac{m}{s}$ (~117 knots), meeting the RFP's drop speed objective.

On the other hand, the parabolic dashed lines represent the power required by the aircraft to maintain a certain airspeed at various elevations. As described in Figure. 9.8, the power required to maintain the drop speed of 60 $\frac{m}{s}$ ($\sim$117 knots) is well below the power available up to an elevation of 1050 m. This means that Baruna-1 will be capable of maintaining its drop speed at 50 - 1050 m of elevation without any issue.

9.8 Dash Speed

The dash speed of Baruna-1 can be represented in Figure. 9.9 (a) through (b) at various altitudes. As seen on each of the figures, they all show a parabolic relationship between the airspeed and the power of Baruna-1. The key takeaway from all three figures is to show that Baruna-1 is able to fly with a dash speed above the objective dash speed established in the RFP.

The maximum velocity of the airfoil's critical Mach Number are 210.09 $\frac{m}{s}$, 208.85 $\frac{m}{s}$, and 206.34 $\frac{m}{s}$ for the altitudes 2,000 m, 2,500 m, and 3,500 m, respectively, which are above the objective dash speed at 205.78 $\frac{m}{s}$. Furthermore, the maximum velocity at these altitudes is $\sim$220 $\frac{m}{s}$ which is also above the objective dash speed.

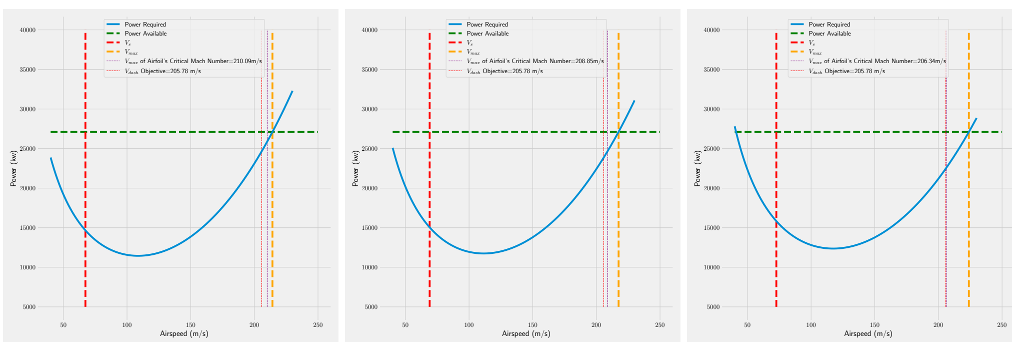

(a) Dash speed at an altitude of 2,000 m (b) Dash speed at an altitude of 2,500 m (c) Dash speed at an altitude of 3,500 m

FIGURE 9.9: Baruna-1's dash speed at different altitudes.

9.9 Gliding Performance

Figure. 9.10 shows a hodograph plot of Baruna-1's gliding performance at various altitudes and weights. The continuous plot lines represent the W-Empty gliding performance of the aircraft at different altitudes. In contrast, the dotted and dashed plot lines depict the EMTOW and MTOW gliding performance, respectively. The highest rate of descent can be found on the MTOW configuration at an altitude of 3,500 m, while the lowest rate of descent can be found on the W-Empty configuration at an altitude of 1,000 m.

9.10 Turning Performance

The turning radius and turning rate for Baruna-1 can be seen in Figure. 9.12 (a) and (b) as well as Figure. 9.13 (a) and (b). Figure. 9.12 (a) and (b) show the MTOW coordinated turning radius for various bank angles at an altitude of 50 m and 3,000 m, respectively. Those figures show the exact same trend where a 10° bank angle has the largest turning radius at low speeds and a 60° bank angle has the smallest turning radius at high speeds. The steepest slope can also be found when the airplane is banking at a 10°

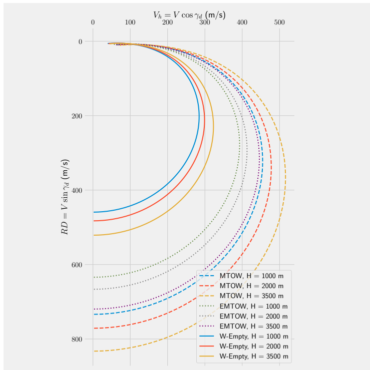

FIGURE 9.10: Gliding performance

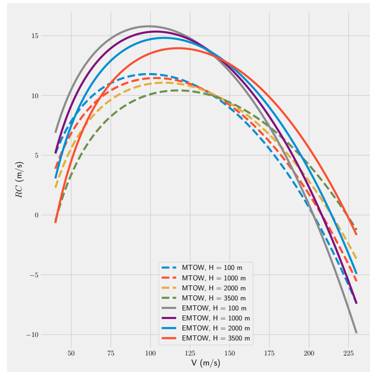

FIGURE 9.11: Climbing performance

angle and has a maximum turning radius of ∼5.3 km at a 50 m altitude and ∼7 km at a 3,000 m altitude, while the "flattest" slope is found when the airplane is banking at a 60° angle and has a minimum turning radius of ∼0.4 km at 50 m and ∼0.8 km at 3,000 m.

Furthermore, Figure. 9.13 (a) and (b) show the time taken to perform a coordinated 180° turn at MTOW for various bank angles at an altitude of 50 m and 3,000 m, respectively. Again, the trends for both graphs are similar to one another. Turning with a 30° bank angle still gives the steepest slope, while turning with a 60° bank angle gives the "flattest" slope. Turning with a 30° bank angle also gives the longest turning rate with a maximum time of ∼2.8 minutes, while the shortest turning rate happens when turning at a 60° bank angle with a minimum time of ∼0.2 minutes at an altitude of 50 m. At an altitude of 3000 m, the maximum time taken to turn is ∼3.5 minutes and the minimum time taken to turn is ∼0.4 minutes.

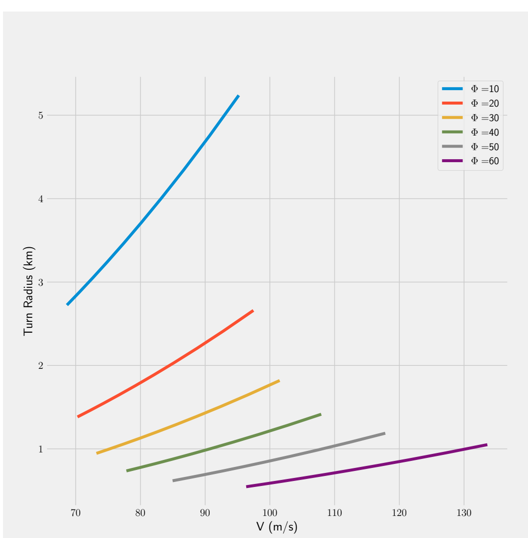

(a) Turning radius at an altitude of 50 m

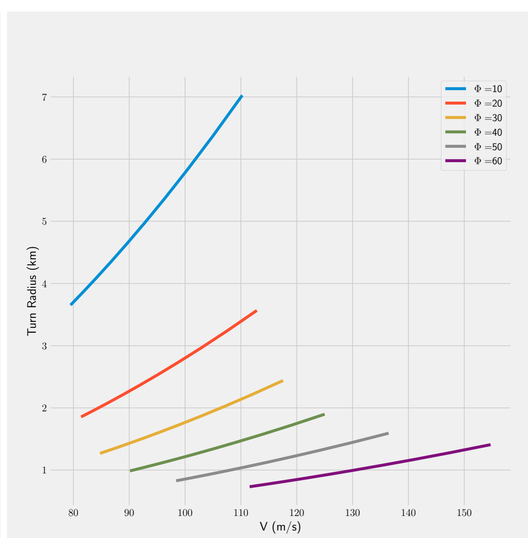

(b) Turning radius at an altitude of 3000 m

FIGURE 9.12: Turning radius at different altitudes with various bank angles

9.11 Climbing Performance

The rate of climb of Baruna-1 at various altitudes and weights can be found in Figure. 9.11, The continuous plot lines represent the EMTOW performance, while the dashed ones represent the MTOW performance. A parabolic relationship can be observed for every weight at different altitudes from the figure. It can also be seen that the highest rate of climb belongs to the EMTOW condition at an altitude of 100 m (∼328 ft) with a value of ∼16 $\frac{m}{s}$ (∼3,150 $\frac{ft}{min}$) at a velocity of ∼90 $\frac{m}{s}$ (175 knots). Moreover, the highest rate of climb for the MTOW condition is also at an altitude of 100 m with a value of ∼13 $\frac{m}{s}$ (∼2,559 $\frac{ft}{min}$) at a velocity of ∼90 $\frac{m}{s}$ (∼175 knots) as well.

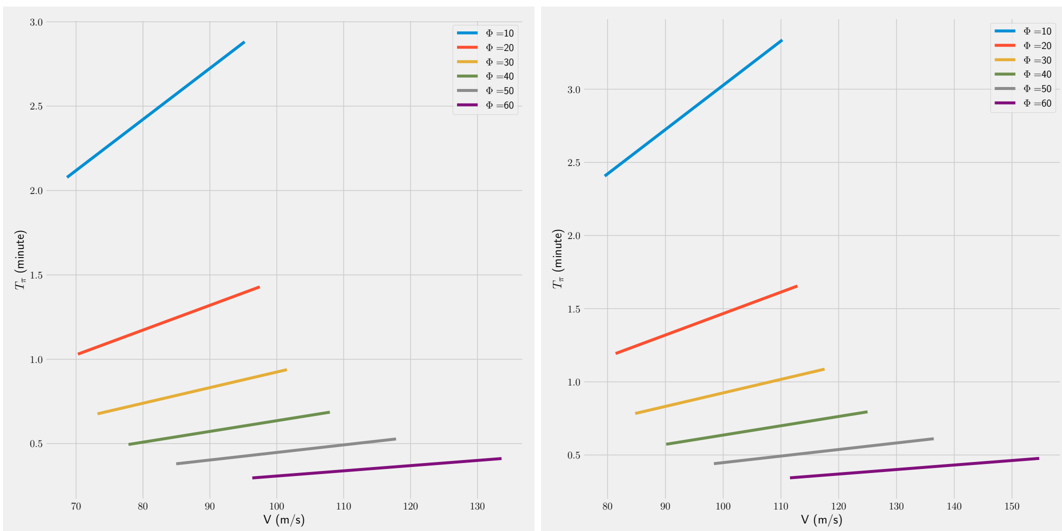

(a) Turning rate at an altitude of 50 m

(b) Turning rate at an altitude of 3000 m

FIGURE 9.13: Turning rates at different altitudes with various bank angles

Chapter 10

Cost Analysis

The production and the O&M (operations and maintenance) costs were estimated using the Eastlake Model [117] and the methods given in [118], respectively.

The Eastlake Model is another modification of the RAND DAPCA IV [119], similar to the cost estimation methods used in [120] and [118]. However, it considers a discount factor for buying off-the-shelf components in bulk and further includes a manufacturer's liability insurance to the minimum selling price.

Worker wages were mainly obtained from [117] and [121]. Additionally, all the costs given in this section have been adjusted for 2030 Dollars by predicting CPI factors (Consumer Price Index [121]) relative to the year 2030 through data extrapolation starting from the year 2012.

10.1 Production Cost

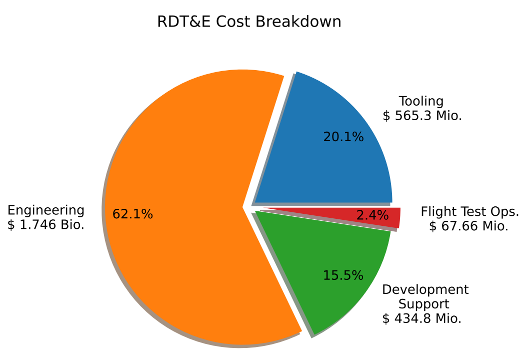

(a) RDT&E cost.

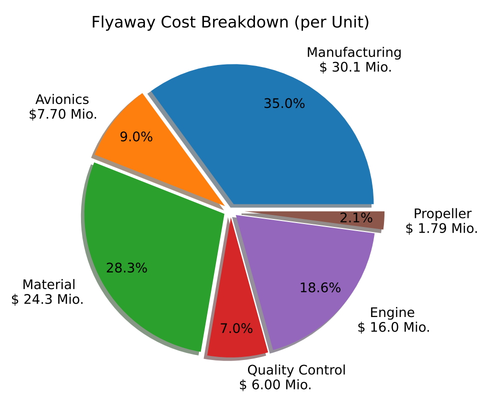

(b) Flyaway cost.

FIGURE 10.1: Production cost breakdown.

The production cost consists of the RDT&E (research, development, test, and evaluation) and the flyaway cost. Figure 10.1(a) shows the individual contributors to the RDT&E cost, which adds to 2,813,601,763.98 USD. The RDT&E cost is a fixed cost that will be amortized over a total of 105 aircraft; equaling to expected 7 aircraft production per year over a 15-year production span.

The flyaway cost breakdown is illustrated in 10.1 totaling 85,904,723.30 USD per unit. Adding the

Source	Value/unit
RDT&E Cost	$ 26,796,207.28
Flyaway Cost	$ 85,904,723.30
Man. Liability Insurance	$ 27,387,236.70
Min. Selling Price	$ 140,088,167.27
Price after Markup	**$ 162,000,000.00**
Break-Even Units	**37**

TABLE 10.1: Purchase price summary.

manufacturer's liability insurance and a 15% profit margin, the purchase price of 162 Mio. USD is obtained as summarized in Table. 10.1. The program is projected to break even after 37 units are sold.

10.2 Operating Cost

The summary of the O&M cost to operate the aircraft is given in Table 10.2. The maintenance material cost has been assumed to be equal to the cost of the maintenance labor as given in [118] due to the overall similarities between Baruna-1 to a military aircraft; e.g. operated by the government, unscheduled and strategically planned missions, and bombs and retardant analogy.

Source	*Source*	% of O&M
Maintenance Labor	$ 3,280,320.00	23.66%
Maintenance Material	$ 3,280,320.00	23.66%
Fuel	$ 6,623,057.19	47.76%
Crews	$ 267,306.18	1.93%
Insurance	$ 416,010.41	3.00%
Total Yearly O&M Cost	**$ 13,867,013.78**	
Hourly O&M Cost	**$ 11,555.84**	

TABLE 10.2: O&M cost estimation.

Source	Value
Fixed Ground Support (1st Scenario)	$ 6,575.47
Fixed Ground Support (2nd Scenario)	$ 8,298.98
Mobile Ground Support	$ 43,552.00
Crews (annually)	$ 95,760.00

TABLE 10.3: Ground fire fighting support system cost.

Finally, the cost summary for the ground fire fighting support previously explained in Section 7.2, are presented in Table 10.3. Aside from crew wages, the fixed and mobile ground supports are non-recurring and their total cost will vary between different aerodromes or stations. The storage, retardant, and landing fees are omitted from the O&M cost as these expenses are usually managed by the government.

Chapter 11

Compliance to the RFP

Table 11.1, shows the compliance of Baruna-1 is fully complied with the RFP.

Requirements	**Baruna-1's Compliance to the RFP**
Retardant Capacity	
[R] 15,200 L	✓
Multi Drop	
[R] Minimum 7,600 kg per drop	✓
Retardant Reload Speed	
[R] 32 kg/s	✓
Drop Speed	
[O] <= 232 kts	✓
Drop Altitude	
[R] <= 92 m AGL	✓
Design Radius with Full Payload	
[O] 740 km	✓
Design Ferry Range (No Payload)	
[O] 5,556 km	✓
Dash Speed (After Payload Drop)	
[O] 741 km/h	✓
Field Requirements (@ 5,000 ft (1,524 m) MSL at 1.67°C)	
[O] 1524 m	✓
Certifications	
[R] Capable VFR & IFR flight w/ autopilot	✓
[R] Capable flight in known icing conditions	✓
[R] Meets applicable certification rules in FAA 14 CFR Part 25	✓
[O] Provides systems & avionics architecture that will enable autonomous operations	✓

TABLE 11.1: Baruna-1 compliance to the AIAA's RFP.

Bibliography

[1] A Malcolm Gill, Scott L Stephens, and Geoffrey J Cary. "The Worldwide "Wildfire" Problem". In: *Ecological applications* 23.2 (2013), pp. 438–454.

[2] *Global Trends in Wildfire and Its Impacts*. Oct. 2020.

[3] Niels Andela et al. "A Human-Driven Decline in Global Burned Area". In: *Science (New York, N.Y.)* 356.6345 (2017), pp. 1356–1362.

[4] Joshua Lizundia-Loiola et al. "A Spatio-Temporal Active-Fire Clustering Approach for Global Burned Area Mapping at 250 m from MODIS Data". In: *Remote Sensing of Environment* 236 (2020), p. 111493.

[5] *Multi-Decade Global Fire Dataset Set to Support Trend Analysis*.

[6] *Six Trends to Know about Fire Season in the Western U.S.* Dec. 2018.

[7] Olga Pechony and Drew T Shindell. "Driving Forces of Global Wildfires over the Past Millennium and the Forthcoming Century". In: *Proceedings of the National Academy of Sciences* 107.45 (2010), pp. 19167–19170.

[8] David M Romps et al. "Projected Increase in Lightning Strikes in the United States Due to Global Warming". In: *Science (New York, N.Y.)* 346.6211 (2014), pp. 851–854.

[9] Steven W Running. "Is Global Warming Causing More, Larger Wildfires?" In: *Science (New York, N.Y.)* (2006).

[10] Matthew W Jones et al. "Climate Change Increases Risk of Wildfires". In: *ScienceBrief Review* 116 (2020), p. 117.

[11] Sarah Elise Finlay et al. "Health Impacts of Wildfires". In: *PLoS currents* 4 (2012).

[12] Daniel A Jaffe and Nicole L Wigder. "Ozone Production from Wildfires: A Critical Review". In: *Atmospheric Environment* 51 (2012), pp. 1–10.

[13] Leandro Silveira et al. "Impact of Wildfires on the Megafauna of Emas National Park, Central Brazil". In: *Oryx : the journal of the Fauna Preservation Society* 33.2 (1999), pp. 108–114.

[14] Travis B Paveglio et al. "Understanding Social Impact from Wildfires: Advancing Means for Assessment". In: *International Journal of Wildland Fire* 24.2 (2015), pp. 212–224.

[15] Jon J Driessen. *Crew Cohesion, Wildland Fire Transition, and Fatalities*. US Department of Agriculture, Forest Service, Technology & Development Program, 2002.

[16] National Wildfire Coordinating Group. *Wildland Fire Incident Management Field Guide*. National Wildfire Coordinating Group, 2014.

[17] MP Plucinski et al. "The effect of aerial suppression on the containment time of Australian wildfires estimated by fire management personnel". In: *International Journal of Wildland Fire* 21.3 (2011), pp. 219–229.

[18] Ahmed Hassanein et al. "An Autonomous Firefighting Robot". In: *2015 International Conference on Advanced Robotics (ICAR)*. IEEE. 2015, pp. 530–535.

[19] Gregory J McCarthy. *Effectiveness of Aircraft Operations by the Department of Natural Resources and Environment and The Country Fire Authority 1997-98*. Department of Sustainability and Environment, 2003.

[20] U.S. Department of Agriculture. *Aerial Firefighting Use and Effectiveness (AFUE) Report*.

[21] Cees Bil. "C-17 Conversion System for Fire Fighting Operations". In: *53rd AIAA Aerospace Sciences Meeting*. 2015, p. 1904.

[22] Matthew P Thompson et al. "Airtankers and Wildfire Management in the US Forest Service: Examining Data Availability and Exploring Usage and Cost Trends". In: *International Journal of Wildland Fire* 22.2 (2012), pp. 223–233.

[23] Crystal S Stonesifer et al. "Characterizing Large Airtanker Use in United States Fire Management". In: *In: Keane, Robert e.; Jolly, Matt; Parsons, Russell; Riley, Karin. Proceedings of the Large Wildland Fires Conference; May 19-23, 2014; Missoula, MT. Proc. RMRS-P-73. Fort Collins, CO: US Department of Agriculture, Forest Service, Rocky Mountain Research Station. p. 314-316.* Vol. 73. 2015, pp. 314–316.

[24] Tom Appleton. "Supreme Scooper". In: *The Forestry Chronicle* 74.4 (1998), pp. 511–513.

[25] Peter Kal'avskỳ et al. "The Efficiency of Aerial Firefighting in Varying Flying Conditions". In: *2019 International Conference on Military Technologies (ICMT)*. IEEE. 2019, pp. 1–5.

[26] AIAA Aircraft Design Competition Technical Committee. *Request for Proposal: Responsive Aerial Fire Fighting Aircraft*. 2021.

[27] Daniel P. Raymer. *Aircraft Design: A Conceptual Approach*. AIAA Education Series. Reston, VA: American Institute of Aeronautics and Astronautics, Inc, 2018. ISBN: 978-1-62410-490-9.

[28] Mohammad H. Sadraey. *Aircraft Design: A Systems Engineering Approach*. Aerospace Series. Chichester, West Sussex: Wiley, 2013. ISBN: 978-1-119-95340-1.

[29] G. J. J Ruijgrok. *Elements of Airplane Performance*. 2009. ISBN: 978-90-6562-232-7 978-90-6562-203-7 978-90-6562-204-4.

[30] Jan Roskam. *Airplane Design*. Lawrence, Kan: DARcorporation, 2002. ISBN: 978-1-884885-24-2.

[31] Robert J McGhee, William D Beasley, and Dan M Somers. *Low-speed aerodynamic characteristics of a 13-percent-thick airfoil section designed for general aviation applications*. Tech. rep. 1975.

[32] Snorri Gudmundsson. *General aviation aircraft design: Applied Methods and Procedures*. Butterworth-Heinemann, 2013.

[33] Zdeněk Pátek and Marian Zabloudil. “Pressure Distribution Development on an Airfoil with a Fowler Flap”. In: *RRDPAE Proceedings* 2008 ().

[34] Lee Smith. *Deep Stall Aerodynamics*. Jan. 2010.

[35] *14 CFR Part 25 – Airworthiness Standards: Transport Category Airplanes*. https://www.ecfr.gov/current/title-14/chapter-I/subchapter-C/part-25?toc=1.

[36] *Aerospace Aluminum Distributor Supplier*. https://www.aerospacemetals.com/aluminum-distributor.html.

[37] Ikuhiro INAGAKI et al. “Application and Features of Titanium for the Aerospace Industry”. In: NPPON STEEL & SUMITOMO METAL TECHNICAL REPORT.No.106 (July 2014).

[38] *The Materials Used in the Design of Aircraft Wings*. https://www.azom.com/article.aspx?ArticleID=12117. 2015-06-09T05:50:00.0000000-04:00.

[39] *FAR § 25.337*.

[40] *FAR § 25.335*.

[41] *EASA.E.033 - Europrop International GmbH TP400-D6 Engine*. https://www.easa.europa.eu/document-library/type-certificates/engine-cs-e/easae033-europrop-international-gmbh-tp400-d6-engine. Mar. 2022.

[42] *Military Turboshaft/Turboprop Specifications*. https://www.jet-engine.net/miltsspec.htm. Apr. 2022.

[43] Ulyanovsk Higher Aviation School of Civil Aviation. *Domestic Aerospace Engineering (in Russian)*. http://www.uvauga-dvig.narod.ru/nk-12mp_12mk.pdf.

[44] Tom Fey. *Curtiss Turboelectric Propeller*. https://www.enginehistory.org/Propellers/Curtiss/Turboelectric/Turboelectric.shtm Aug. 2019.

[45] *Ivchenko Progress D-27 Propfan Aero Engine*. https://ivchenko-progress.com/wp-content/uploads/pdf/d27.pdf. May 2015.

[46] *TP400-D6 - MTU Aero Engines*. https://www.mtu.de/engines/military-aircraft-engines/transport-aircraft/tp400-d6/. Mar. 2022.

[47] Rolls Royce PLC. *TP400-D6*. https://www.rolls-royce.com/products-and-services/defence/aerospace/transport-tanker-patrol-and-tactical/tp400-d6.aspx#/.

[48] Safran Aircraft Engine, Adrien Daste, and Benoit Vallet. *TP400 - A New-Generation Turboprop Engine*. https://www.safran-group.com/products-services/tp400-new-generation-turboprop-engine. Apr. 2022.

[49] *TP400-D6 Turboprop Engine - Europrop International*. https://www.europrop-int.com/the-tp400-d6/.

[50] Dieter Scholz et al. *FUEL CONSUMPTION DUE TO SHAFT POWER OFF-TAKES FROM THE ENGINE*. 2013.

[51] *EASA.P.012 - Ratier-Figeac FH385-FH386 Series Propellers*. https://www.easa.europa.eu/document-library/type-certificates/propeller-cs-p/easap012-ratier-figeac-fh385-fh386-series. Apr. 2022.

[52] Norman S. Currey. *Aircraft Landing Gear Design: Principles and Practices*. AIAA, 1988. ISBN: 978-1-60086-018-8.

[53] *DR20523T / Tyre Specification / Dunlop Aircraft Tyres - Manufacturer and Retreader of Aircraft Tires*. https://www.dunlopaircrafttyres.co.uk/tyres/detail/dr20523t.

[54] *14 CFR Part 25 Subpart F – Equipment*. https://www.ecfr.gov/current/title-14/chapter-I/subchapter-C/part-25/subpart-F.

[55] *Fly-by-Wire Flight Control Systems and Computers*. https://www.thalesgroup.com/en/markets/aerospace/flight-deck-avionics-equipment-functions/fly-wire-flight-control-systems-and.

[56] *Air Data Systems*. https://www.collinsaerospace.com/what-we-do/Commercial-Aviation/Flight-Deck/Surveillance/Air-Data-Systems.

[57] Rockwell Collins. *SmartProbe® Air Data Systems Advanced, Integrated Solutions for Modern Aircraft*. 2017.

[58] Southeast Aerospace. *Collins Aerospace AHC-3000*. https://www.seaerospace.com/sales/product/Collins%20Aerospace/AHC-3000.

[59] *APS-85 Autopilot System*. https://www.collinsaerospace.com/what-we-do/Military-And-Defense/Avionics/Autopilot/Aps-85-Autopilot-System.

[60] I. Moir, A. G. Seabridge, and Malcolm Jukes. *Civil Avionic Systems*. 2nd edition. Chichester, West Sussex: Wiley, 2013. ISBN: 978-1-118-53672-8 978-1-118-53673-5 978-1-118-53674-2.

[61] Ian Moir, Allan Seabridge, and ProQuest (Firm). *Aircraft Systems: Mechanical, Electrical and Avionics Subsystems Integration.* Chichester, West Sussex, England; Hoboken, NJ: Wiley, 2011. ISBN: 978-0-470-77094-8.

[62] Honeywell. *Air Data Inertial Reference System (ADIRS)*. 2007.

[63] *Air Data Inertial Reference System (ADIRS)*. https://aerospace.honeywell.com/us/en/learn/products/sensors/air-data-inertial-reference-system.

[64] *FMC 4000 Flight Mission Computer*. https://www.collinsaerospace.com/what-we-do/Military-And-Defense/Avionics/Computing-And-Networks/Mission-Computers/Fmc-4000-Flight-Mission-Computer.

[65] Rockwell Collins. *FMC-4500 Flight Mission Computer Family > Data Sheet*. 2018.

[66] *CDU-7000 Control Display Units*. https://www.collinsaerospace.com/what-we-do/Military-And-Defense/Displays-And-Controls/Airborne/Control-Display-Units/Cdu-7000-Control-Display-Units.

[67] Rockwell Collins. *CDU-7000*. 2008.

[68] *GPS-4000S Global Positioning System Sensor*. https://www.collinsaerospace.com/what-we-do/Commercial-Aviation/Flight-Deck/Navigation-And-Guidance/Gps-Devices/Gps-4000S-Global-Positioning-System-Sensor.

[69] Rockwell Collins. *Rockwell Collins GPS-4000S*. 2007.

[70] *TTR-2100 Airborne Collision Avoidance System Traffic Computer*. https://www.collinsaerospace.com/what-we-do/Business-Aviation/Flight-Deck/Additional-Flight-Deck/Traffic-Awareness/Ttr-2100-Airborne-Collision-Avoidance-System-Traffic-Computer.

[71] Rockwell Collins. *TTR-2100/TTR-4100 AIRBORNE COLLISION AVOIDANCE SYSTEM/TRAFFIC COMPUTER*. 2019.

[72] Southeast Aerospace. *Honeywell MK VIII*. https://www.seaerospace.com/sales/product/Honeywell/MK%20VIII.

[73] *Mark VIII EGPWS*. https://aerospace.honeywell.com/us/en/learn/products/terrain-and-traffic-awareness/mark-viii-egpws.

[74] *ALT-1000/4000 Radio Altimeter*. https://www.collinsaerospace.com/what-we-do/Business-Aviation/Flight-Deck/Additional-Flight-Deck/Datalink-Communications-And-Navigation/Navigation/Alt10004000radioaltimeter.

[75] Southeast Aerospace. *Collins Aerospace ALT-4000*. https://www.seaerospace.com/sales/product/Collins%20Aerospace/ALT-4000.

[76] *FA5000 Series — Cockpit Voice & Flight Data Recorders*. https://www.l3harris.com/all-capabilities/fa5000-series-cockpit-voice-flight-data-recorders.

[77] *ELT 5000 Distress Tracking (DT) For GADSS Compliance*. https://www.acrartex.com/products/elt-5000-distress-tracking-dt-for-gadss-compliance/.

[78] *NAV-4000/4500/VIR-4000/ADF-4000 Navigation Receivers*. https://www.collinsaerospace.com/what-we-do/Business-Aviation/Flight-Deck/Additional-Flight-Deck/Datalink-Communications-And-Navigation/Navigation/Nav4

[79] Southeast Aerospace. *Collins Aerospace NAV-4000*. https://www.seaerospace.com/sales/product/Collins%20Aerospace/NAV-4000.

[80] *DME 4000 Distance Measuring Equipment*. https://www.collinsaerospace.com/what-we-do/Business-Aviation/Flight-Deck/Additional-Flight-Deck/Datalink-Communications-And-Navigation/Navigation/Dme-4000-Distance-Measuring-Equipment.

[81] Southeast Aerospace. *Collins Aerospace DME-4000*. https://www.seaerospace.com/sales/product/Collins%20Aerospace/DM 4000.

[82] Honeywell. *CMU MARK II+ DATA COMMUNICATIONS*. 2022.

[83] *Mark II+ Communications Management Unit*. https://aerospace.honeywell.com/us/en/learn/products/navigation-and-radios/mark-ii-communications-management-unit.

[84] *VHF-4000 VHF Communication Transceiver*. https://www.collinsaerospace.com/what-we-do/Business-Aviation/Flight-Deck/Additional-Flight-Deck/Datalink-Communications-And-Navigation/Datalink-And-Communications/Vhf-4000-Vhf-Communication-Transceiver.

[85] Southeast Aerospace. *Collins Aerospace VHF-4000*. https://www.seaerospace.com/sales/product/Collins%20Aerospace/VHF 4000.

[86] *Primus HF-1050*. https://aerospace.honeywell.com/us/en/learn/products/navigation-and-radios/primus-hf-1050.

[87] Honeywell. *Honeywell Primus HF 1050 HF Radio System*.

[88] Rockwell Collins. *IRT NX SATCOM SYSTEM FOR IRIDIUM®*. 2021.

[89] *IRT-NX SATCOM System for Iridium®*. https://www.collinsaerospace.com/what-we-do/Commercial-Aviation/Flight-Deck/Communications/Satcom/IRT-4XX0-next-generation-Iridium-SATCOM-system.

[90] *TPR-901 — Collins*. https://www.collinsaerospace.com/what-we-do/Commercial-Aviation/Flight-Deck/Surveillance/Transponders/TPR-901.

[91] Rockwell Collins. *TPR-901-003/021 Transponders: Meeting Worldwide ADS-B Mandates*. 2009.

[92] *Head Up Display (HUD)*. https://www.collinsaerospace.com/what-we-do/Commercial-Aviation/Flight-Deck/Head-Up-Display.

[93] *Helmet-Mounted Display for Aircraft: Transport, Helicopter & Fighter*. https://www.thalesgroup.com/en/markets/aerospace/f deck-avionics-equipment-functions/helmet-mounted-display-aircraft.

[94] *TopOwl, Helmet-mounted Sight & Display for Helicopters*. https://www.thalesgroup.com/en/markets/aerospace/flight-deck-avionics-equipment-functions/helmet-mounted-display/TopOwl.

[95] Avionics Sales Corporation. *822-1084-051/822-1753-351 - AFD 3010/3010E FLIGHT DISPLAY*.

[96] Southeast Aerospace. *Collins Aerospace AFD-3010E*. https://www.seaerospace.com/sales/product/Collins%20Aerospace/AF 3010E.

[97] *GH-3900 Electronic Standby Instrument System (ESIS)*. https://www.l3harris.com/all-capabilities/gh-3900-electronic-standby-instrument-system-esis.

[98] L3Harris. *GH-3900 ESIS ELECTRONIC STANDBY INSTRUMENT SYSTEM*. 2021.

[99] *USFS Additional Telemetry Unit ATIS*. https://www.latitudetech.com/solutions/additional-telemetry-unit/.

[100] Rockwell Collins. *Ice Detectors 0871ND Series*. 2015.

[101] *Ice Detection Systems*. https://www.collinsaerospace.com/what-we-do/Helicopters/Commercial-Helicopters/Ice-Detection-Systems.

[102] Ian Moir and Allan Seabridge. *Aircraft Systems*. Third Edition. John Wiley & Sons Ltd, The Atrium, Southern Gate, Chichester, West Sussex PO19 8SQ, England: John Wiley & Sons, Ltd, 2008. ISBN: 978-0-470-05996-8.

[103] Trotter Control. *FRDS GENIII*. https://www.frdsgeniii.com/home. Apr. 2022.

[104] ASME. *BPVC Section XII-Rules for Construction and Continued Service of Transport Tanks*. ASME, 2021. ISBN: 978-0-7918-7430-1.

[105] *Aircraft Bleed Air Systems*. https://skybrary.aero/articles/aircraft-bleed-air-systems. May 2021.

[106] *Bolt Assembled Fiberglass Plastic Water Reservoir Tank 40000 Liters - Buy Water Tank 40000 Liters,Plastic Water Reservoir Tank,Fiberglass Water Reservoir 40000 Liters Product on Alibaba.Com*. https://www.alibaba.com/product-detail/Bolt-Assembled-Fiberglass-Plastic-Water-Reservoir_1600246545265.html?spm=a2

[107] *5” Inch Fire Hose Double Jacket — FireHoseSupply.Com*. https://www.firehosesupply.com/products/6-inch-double-jacket-fire-hose.

[108] *Stainless Steel Centrifugal Pump Manufacturer Ss304 316l Alkali Pump Oem Odm - Buy Stainless Steel Centrifugal Pump,Alkali Pump,Centrifugal Pump Product on Alibaba.Com*. https://www.alibaba.com/product-detail/Centrifugal-Pump-Ss304-Centrifugal-Pump-Stainless_1600448753278.html?spm=a2700.galleryofferlist.normal_offer.

[109] forestry-suppliers.com. *Fomtec Enviro Class A Foam*. http://www.forestry-suppliers.com/product_pages/products.php?mi=39

[110] *High Technology Vacuum Pump Blower Ring Blower Side Channel Blower - Buy High Pressure Side Channel Blower/Dust Absorption Ring Blower /Pneumatic Waste Conveying Air Blower/Aluminium Alloy Ring Blower,High Quality Big Electric Sewage Treatment Air Blowers/Cleaning Air Blower/Food Drying Side Channel Blower/Side Channel Blower,Single Phase Air Blower/ Three Phase Blower/ Biogas Conveying Atex Explosion C Cost Litter Vibration Air Blower Product on Alibaba.Com*. https://www.alibaba.com/product-detail/Vacuum-Pump-High-Technology-Vacuum-Pump_1600208402297.html?spm=a2700

[111] *6" Flexible Pipe Coupling,Universal Joint Coupling For Di,Ci,Pe,Pvc Pipe - Buy Pipe Coupling,Universal Joint Coupling,Universal Coupling Product on Alibaba.Com*. https://www.alibaba.com/product-detail/Coupling-Universal-Coupling-6-Flexible-Pipe_1600200745416.html?spm=a2700.7724857.normal_offer.d_title.612b27

[112] *Tri Axles 42000 50000 Liters Diesel Oil Water Fuel Tanker Truck Trailer For Sale - Buy 50000 Liters Fuel Tank Trailer,42000l Fuel Tank Trailer,Fuel Tanker Truck Trailer Product on Alibaba.Com*. https://www.alibaba.com/product-detail/Tri-Axles-42000-50000-Liters-Diesel_60819237741.html?spm=a2700.galleryofferli

[113] Daniel Raymer. *Aircraft design: a conceptual approach*. American Institute of Aeronautics and Astronautics, Inc., 2012.

[114] Mohammad H. Sadraey. *Aircraft design: a systems engineering approach*. J. Wiley, 2013.

[115] Marcello R. Napolitano. *Aircraft dynamics: from modeling to simulation*. J. Wiley, 2012.

[116] Egbert Torenbeek. *Synthesis of subsonic airplane design: an introduction to the preliminary design of subsonic general aviation and transport aircraft, with emphasis on layout, aerodynamic design, propulsion and performance*. Springer Science & Business Media, 2013.

[117] S. Gudmundsson. *General Aviation Aircraft Design: Applied Methods and Procedures*. Elsevier Science, 2021. ISBN: 978-0-12-822647-6. URL: https://books.google.co.id/books?id=VXcrEAAAQBAJ.

[118] D.P. Raymer. *Aircraft Design: A Conceptual Approach*. AIAA education series. American Institute of Aeronautics and Astronautics, Incorporated, 2018. ISBN: 978-1-62410-490-9. URL: https://books.google.co.id/books?id=3G1uuwEACAAJ.

[119] H. E. Boren. *DAPCA: A Computer Program for Determining Aircraft Development and Production Costs*. Santa Monica, CA: RAND Corporation, 1967.

[120] L.M. Nicolai and G. Carichner. *Fundamentals of Aircraft and Airship Design*. AIAA education series v. 1. American Institute of Aeronautics and Astronautics, 2010. ISBN: 978-1-60086-751-4. URL: https://books.google.co.id/books?id=qA0oAQAAMAAJ.

[121] *U.S. Bureau of Labor Statistics, https://www.bls.gov/*. en. URL: https://www.bls.gov/ (visited on 05/11/2022).